공학박사학위논문

Superfilling of Through-Silicon-Vias by Cu Electrodeposition with Iodide-based Levelers and Improvement of Filling Efficiency by Adding Thiourea

요오드화물 기반의 평탄제를 포함하는 구리 전해 도금 공정을 통한

실리콘 관통 비아의 초등각 전착과

싸이오요소 첨가를 통한 채움 효율 개선

2017년 2월

서울대학교 대학원

화학생물공학부

김 회 철

Abstract

The scaling of Cu interconnection for the fabrication of densified chips is reaching physical and technological limitation. Intensive researches have been focused on the 3D packaging by using through-silicon-vias (TSVs) to solve the scaling limitation. In the present work, iodide-based levelers were introduced to fill the TSVs without voids, and filling mechanism of TSV and methods to improve the filling efficiency are introduced.

Based on the previously reported molecular structures of levelers, a new leveler containing cationic quaternary ammonium and anionic iodide ion was suggested. The suggested leveler exhibited convection-dependent adsorption characteristic, that is, strong inhibition under forced convection. Electrochemical analyses demonstrated that the leveler enhanced the adsorption strength of suppressor while Cu deposition was promoted by the displacement of accelerator in the stagnant condition. TSV-scaled trenches were filled by adding the accelerator, suppressor, and leveler. Based on the electrochemical analysis and filling results, the filling mechanism was examined: strong inhibition by suppressor and leveler on the top of the trenches, while accumulation of SPS on the bottom that developed the growing surface.

Step current was applied to reduce the filling time in the three-additive system. Step current is composed of (1) low current for the bottom-up growth, and (2) consecutively applied high current for the decrease in the filling time. The growing surface is developed by the accumulation of accelerator during the first step current. Negligible Cu deposition occurred on the side walls near the top where the surface coverage of suppressor and leveler was high enough under the strong convection. Cu was selectively deposited only on the growing surface and the bottom-up growth continued. The filling time was reduced by about 47% with step current deposition compared to that of galvanostatic filling.

To improve the filling performance by modifying the molecular structures of levelers, various kinds of organic levelers were tested. However, the levelers did not affect Cu electrodeposition although the molecular structures were modified by changing the methyl to allyl, hydroxyl to ester group, or elongating the carbon chain. It is obvious that quaternary ammonium ion or iodide ion determines the behavior of the levelers since all the levelers contain it in common. The characteristic as the leveler was more clearly observed in the order of leveler containing Cl^- < Br^- < I^- when levelers containing various halide ions were electrochemically analyzed.

Electrochemical analysis was conducted with the addition of NaI to investigate the

effect of iodide ion in detail. I^- ionized from NaI exhibited the similar electrochemical behavior, of convection-dependent adsorption and synergetic inhibition with suppressor, to the organic levelers. Moreover, cyclic voltammetry demonstrated that I^- retarded the displacement adsorption of SPS. The addition of NaI, instead of organic levelers, also enabled the void-free filling of trenches. Void-free filling was achieved with the addition of KI and NH_4I, as well, through the I^- ionized from the inorganic compounds, which supported that I^- functioned as the leveler.

TSV was filled without voids at an applied current density of 1 mA/cm^2, in the three-additive system containing I^-. However, filling failed at higher current density of 2 mA/cm^2. Thiourea was added to the three-additive composition in order to improve the filling performance at 2 mA/cm^2. Low concentrations of TU increased the adsorption strength of suppressor, while the suppressing layer was disrupted when high concentrations of TU were added. Void-free filling of TSV was enabled at 2 mA/cm^2 by adding low concentrations of TU which enhanced suppressing power and retarded the displacement adsorption of accelerator on the TSV side walls. High concentrations of TU, of course, deteriorated the filling performance by detaching suppressor on the side walls. The filling time was reduced in half by optimizing the 4-additive composition.

Keywords: through-silicon-via (TSV), Cu, leveler, iodide, electrodeposition, galvanostatic deposition, step current, superfilling

Student number: 2011-21032

Content

List of Tables

List of Figures

CHAPTER I

Introduction

1.1. Recent trend for Cu interconnection

The fabrication technique of Cu interconnect, pioneered by IBM in 1997, has been used in the semiconductor integrated circuits (ICs).[1] Compared to the chips made with Al wire which was the standard technology before the Cu interconnect, microprocessors composed of Cu wires show faster operating speed based on lower resistivity of bulk Cu (1.67 μΩ·cm) than bulk Al (2.66 μΩ·cm). The high resistance of Cu interconnects to electromigration increases the reliability of ICs, which accelerates the replacement of Al by Cu, as well.[2-5] The Cu interconnect is formed by Damascene process as shown in Fig. 1.1. The Damascene process includes patterning of silicon oxide, deposition of barrier and Cu seed layer, Cu electrodeposition to fill the pattern, and finally planarization of the over-deposited Cu. With the scaling technology, signal transmission rate can be improved by increasing the number of metal levels. Cu-based ultra-large-scale integration is achieved by repeating the Damascene process. Intel recently introduced 13-layer interconnection as shown in Fig. 1.2.[6]

The dimensions of Cu wires and devices keep on decreasing in order to make densified chips of fast operation speed and less active power. The roadmap for the size of memory and logic devices is shown in Table 1.1.[7] The device technology will continue to drive extreme scaling to improve the chip performance.[8-12] However, the scaling approaches technological limitation: difficulties in patterning by lithography, insufficient margin for the deposition of barrier and seed layer, and troubles in metallization. International Technology Roadmap for Semiconductors reported that it would become impossible to reduce the dimensions of device features by 2020-2025.[7] Nowadays, the effort to improve the device performance has been focused on the 3D integration in order to solve the scaling problem.

Table 1.1. Roadmap for the Size of DRAM, Flash Memory, and Logic Device (Ref. 7)

	Year of production	2015	2017	2019	2021	2024	2027
DRAM	**Half Pitch (nm)**	24	20	17	14	11	8.4
	Cell Size (μm^2)	0.00346	0.00240	0.00116	0.00078	0.0048	0.00028
NAND Flash	**Half Pitch (nm)**	15	14	12	12	12	12
Logic Device	**Node Range (nm)**	16/14	11/10	8/7	6/5	4/3	3/2.5

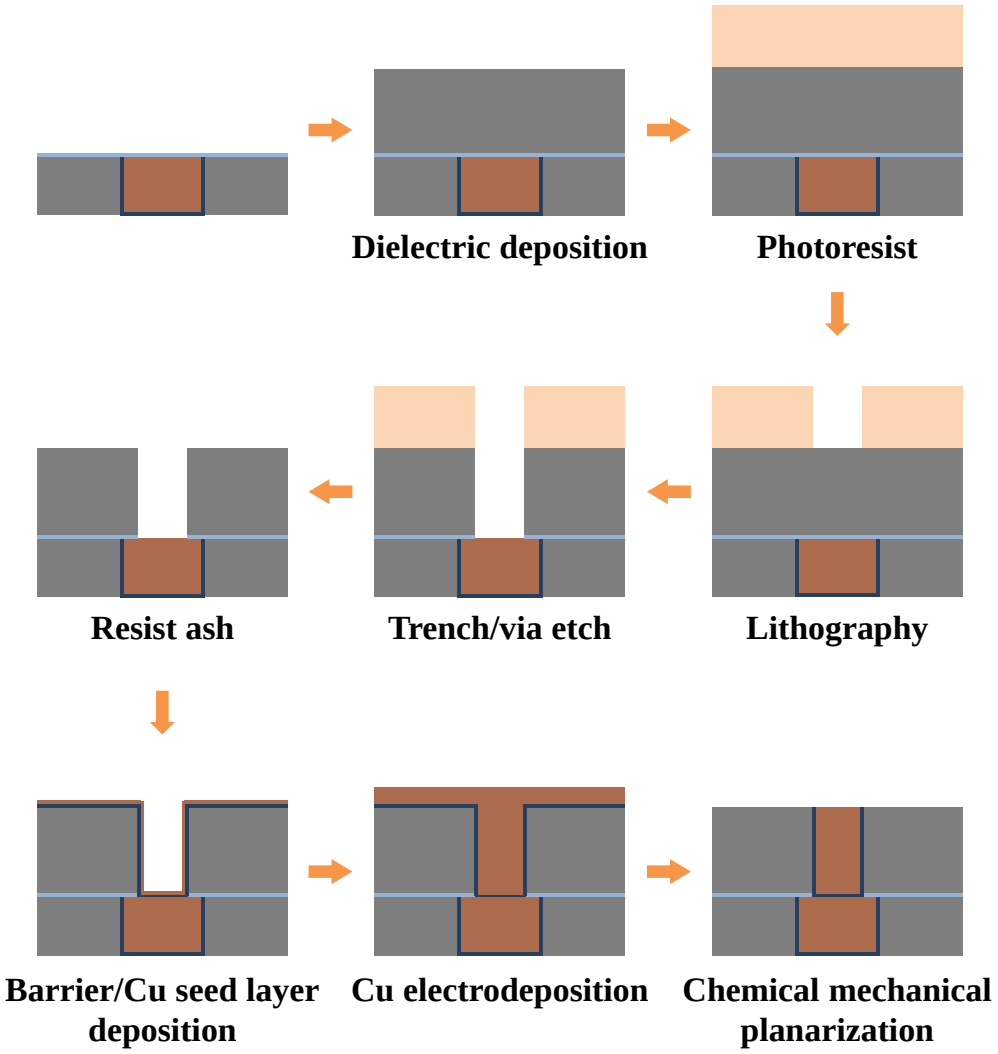

Fig. 1.1. Schematic diagram of single damascene process.

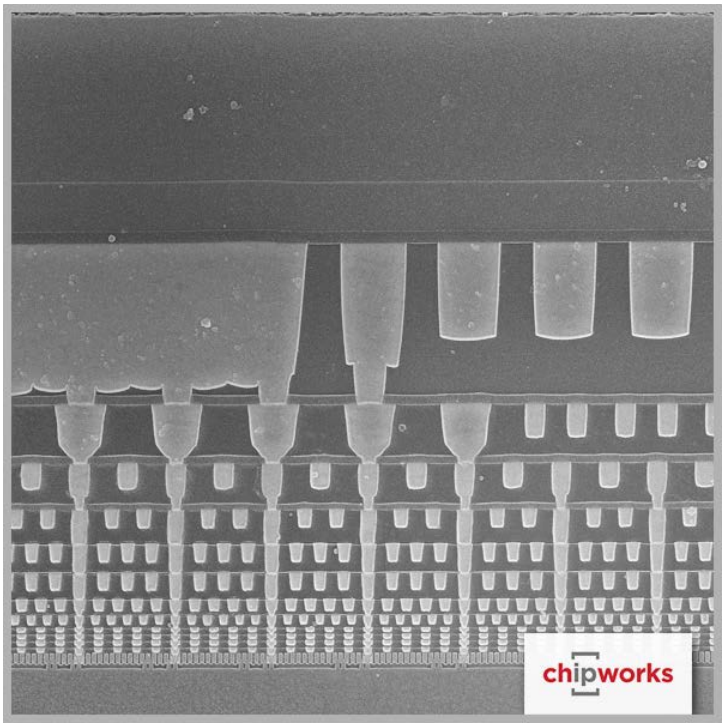

Fig. 1.2. Cross-section image of 13-layer metal lines in Intel’s CPU (Ref. 6).

1.2. Through-silicon-via (TSV) process and Cu electrodeposition

The technology for building three-dimensionally stacked devices promises to improve the device performance.[12-14] The market share of 3D integrated devices is expected to continuously increase. As shown in Fig. 1.3, global equipment and material market for wafer-level-packaging are predicted to gradually expand more than 2,000 million dollars within the next 3 years.[15] Intensive studies have been investigated to enable the wafer-level-packaging as shown in Fig. 1.4. Wire bond packaging is conventionally used to make interconnections between chips by the gold or copper wires. However, wire bonding requires extra space for the wires that make the connection outside the chips.[16] TSV, which is an about 50-μm depth via formed through the Si wafer, vertically interconnects the upper and lower chips. TSV allows densified packaging since no excessive space is required in contrast to the wire bonding. The vertical connection by TSV minimizes the distance for signal propagation, thereby increasing the operation speed. The packaged device by TSV technology is predicted to have reduced size more than 35%, 40% lower power consumption, reduction in the fabrication cost by 45%, and 8 times higher bandwidth.[7]

State-of-the-art TSV process includes Cu electrodeposition for the via filling similarly

to the Damascene process. As shown in Fig. 1.5, via, of a few μm in diameter and a few tens of μm in depth, is formed through the lithography and deep reactive-ion etching process. Diffusion barrier layer and metal seed layer are consecutively deposited on the TSV surface in order to prevent the deposited Cu from being diffused to the Si wafer and to supply electrons for the next-step metallization, respectively. Physical vapor deposition (PVD) has been conventionally used to deposit the barrier and seed layers. Recently, formation of the layers by using electroless deposition is highlighted since the electroless deposition exhibits an excellent step coverage.[17-21] Diffusion layer of Co alloy formed by electroless deposition efficiently blocked the diffusion of Cu at 400°C of annealing temperature.[22] Furthermore, the properties of the barrier layer can be controlled based on the composition of electrolyte in electroless deposition.[23-24] High-step coverage of Cu seed layer was deposited on non-vosch TSV with the Cu electroless deposition.[25] After the formation of seed layer, the TSV wafer is immersed in electrolytes followed by Cu electrodeposition performed by applying current or potential. The TSV is filled by Cu during the metallization step. The over-deposited Cu is removed by chemical mechanical planarization (CMP). Finally, the bottom of the Si substrate is polished by wafer thinning process to expose the conductive metal lines that interconnect chips.

As aforementioned, Cu electrodeposition is a process to reduce Cu ions in the electrolyte on the conductive substrate by externally applying electrons. TSV substrate with the Cu seed layer is used as a working electrode in the electrodeposition process. After dipping both the working electrode and metal or insoluble electrode used as a counter electrode, Cu deposition occurs on the working electrode by applying current or potential as shown in Fig. 1.6. Two charge transfer steps in Cu electrodeposition have been identified.[26-27]

$$Cu^{2+} + e^{-} \rightarrow Cu^{+} \quad (1.1)$$

$$Cu^{+} + e^{-} \rightarrow Cu \quad (1.2)$$

The first reaction determines the deposition rate of Cu as the rate-determining step, with three order of magnitude slower speed than that of the second reaction.[28] Cu dissolution or oxidation reaction is simultaneously observed at the anode during the Cu electrodeposition. The electrolyte is commonly composed of Cu compound for providing Cu ion, supporting electrolyte that reduces the solution resistance, and chloride ion. $CuSO_4$ and H_2SO_4 are representatively used as the Cu compound and the supporting electrolyte, respectively. Methanesulfonic acid, which has higher solubility

of Cu compound than that of H_2SO_4, is applied to TSV filling as one of the substitutive supporting electrolytes.[29]

Three deposition modes are observed during the TSV filling by Cu electrodeposition as shown in Fig. 1.7. Electric field converges on the top surface of the TSV during the Cu electrodeposition in the absence of any additives or at high applied current densities.[30] Cu ion is preferentially consumed for the deposition near the top surface, not reaching the bottom of the TSV. Pinch-off effect, or subconformal deposition therefore occurs, forming voids inside the TSV. Conformal deposition with a seam is obtained when the deposition rates on the top, side walls, and bottom are the same. The size of voids and seams expands during the repetitive operation of semiconductor devices or by the stress release after the annealing.[31-32] Void-free filling is definitely required since small size of the voids can deteriorate the device reliability. Cu deposited selectively on the bottom of the TSV induces bottom-up growth without any defects. The superconformal deposition or so-called superfilling enables the fabrication of highly reliable stacked chips.

Organic additives used in Cu electrodeposition allows superfilling by affecting the local deposition rate.[33-37] The additives are classified into two primary types on the basis of the effect on deposition rate: accelerator and suppressor which promotes and

inhibits Cu deposition rate, respectively. A part of the suppressors that functionally level the macroscale rough surface are referred to as leveler, which will be discussed in detail in Chapter 1.4. The representative accelerators and suppressors used in Cu electrodeposition are listed in Table 1.2. The organic additives, 3-mercapto-1-propanesulfonic acid sodium salt (MPSA), bis(3-sulfopropyl) disulfide disodium salt (SPS), and 3-*N*,*N*-dimethylaminodithiocarbamoy-1-propanesulfonic acid (DPS), accelerates Cu deposition rate.[38-40] Disulfide bond (-S-S-) and mercapto groups (-SH) contained in the accelerators contribute to the acceleration by the following interconversion reaction.[41-42]

$$4Cu^{+} + 2SPS \leftrightarrow 4Cu^{2+} + 4(thiolate)^{-} \leftrightarrow 2Cu^{2+} + 2Cu^{+}\text{-thiolate}^{-} + SPS \quad (1.3)$$

Cu^{+} is generated during the electrodeposition through the Eq. 1.1 or by comproportionation reaction. The generated Cu^{+} reduces SPS to $thiolate^{-}$ which is followed by the reformation of disulfide bond (SPS) accompanying the reduction of Cu^{2+} to Cu^{+}-$thiolate^{-}$. It is known that the Cu-thiolate is rapidly reduced during the electrodeposition. SPS promotes Cu deposition by the consecutive reaction including the interconversion between SPS and MPS^{-}.

Polyethylene glycol (PEG), polypropylene glycol (PPG), and their block copolymer (PEG/PPG) are used as the suppressor with the aid of Cl^-. Cl^- is adsorbed on the Cu surface in an instant after dipping the Cu electrode to the electrolyte. The Cu electrode is covered by the polymeric suppressor which develops the complex with the rapidly adsorbed Cl^-, especially as in the form of PEG-Cu^+-Cl.[43-45] The adsorbed suppressor physically inhibits the approach of Cu^{2+} to the Cu surface, thereby reducing the charge transfer rate of Cu deposition.

The interaction between the accelerator and the suppressor has been investigated in detail to explain the superfilling mechanism in Damascene process.[46-49] The rapidly formed blocking layer by the suppressor is displaced by the accelerator during the Cu electrodeposition.[50] The internal area decreases as Cu is deposited inside the submicrometer trenches. It accompanies the accumulation of the accelerator at the feature bottom, which promotes the local deposition rate on the concave portion. Bump formation above the trench supports the theory of catalyst accumulation by the area reduction. The change in the local coverage is denoted in the following equation,[49]

$$\frac{d\theta_{SPS}}{dt} = k_{ads}(1-\theta_{SPS})C_{SPS} - k_{inc}\theta^q + \upsilon\kappa\theta_{SPS} \quad (1.4)$$

In Eq. 1.4, θ_{SPS} is the surface coverage of adsorbed SPS, k_{ads} is the rate constant for SPS adsorption, C_{SPS} is the bulk concentration of SPS, k_{inc} is the rate constant for SPS incorporation, υ is the deposition rate of Cu in the surface normal direction, and κ is curvature of the surface. The first term in the right-hand side of the equation is related to the adsorption kinetics of SPS. $k_{inc}\theta^q$ is the term considering the consumption rate of SPS by incorporation. The last term, product of curvature, deposition rate, and surface coverage of SPS, indicates the accumulation of SPS by the area reduction during the filling. For the curvature enhanced accelerator coverage (CEAC) model, the last term should dominate the filling system.[49] The competitive adsorption between the accelerator and the suppressor can be applied to explain the filling mechanism of TSV, as discussed later.

Table 1.2. Representative Accelerators and Suppressor in Cu Electrodeposition

Accelerator	**3-Mercapto-1-propanesulfonic acid sodium salt (MPSA)**	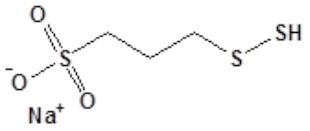
	Bis(3-sulfopropyl) disulfide disodium salt (SPS)	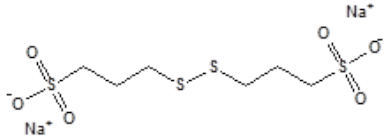
	3-*N*,*N*-Dimethylaminodithiocarbamoy-1-propanesulfonic acid (DPS)	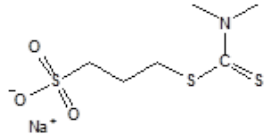
Suppressor	**Polyethylene glycol (PEG)**	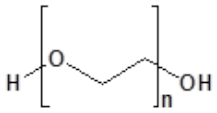
	Polypropylene glycol (PPG)	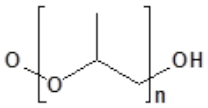
	PEG/PPG block copolymer	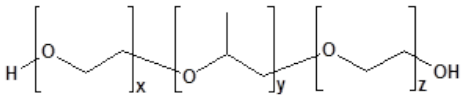
	Polyethyleneimine	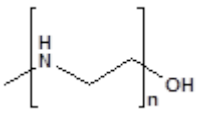
	Tetronic 701	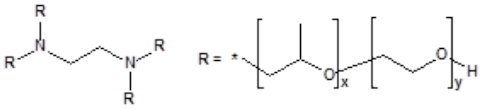

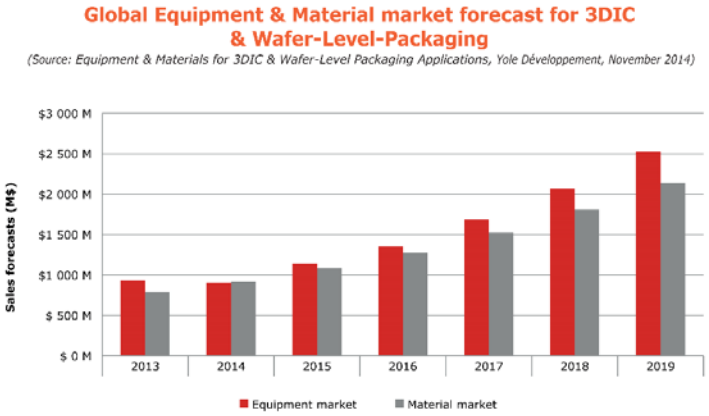

Fig. 1.3. Global equipment and material market forecast for wafer-level-packaging (Ref. 15).

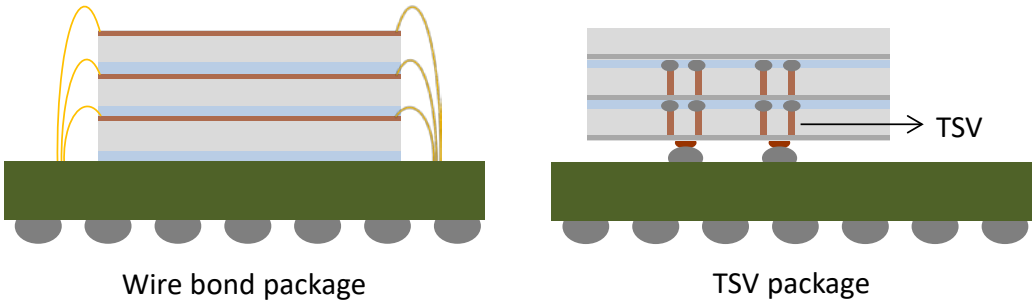

Fig. 1.4. Schematic diagram of packaging technology using wire bonding or TSV.

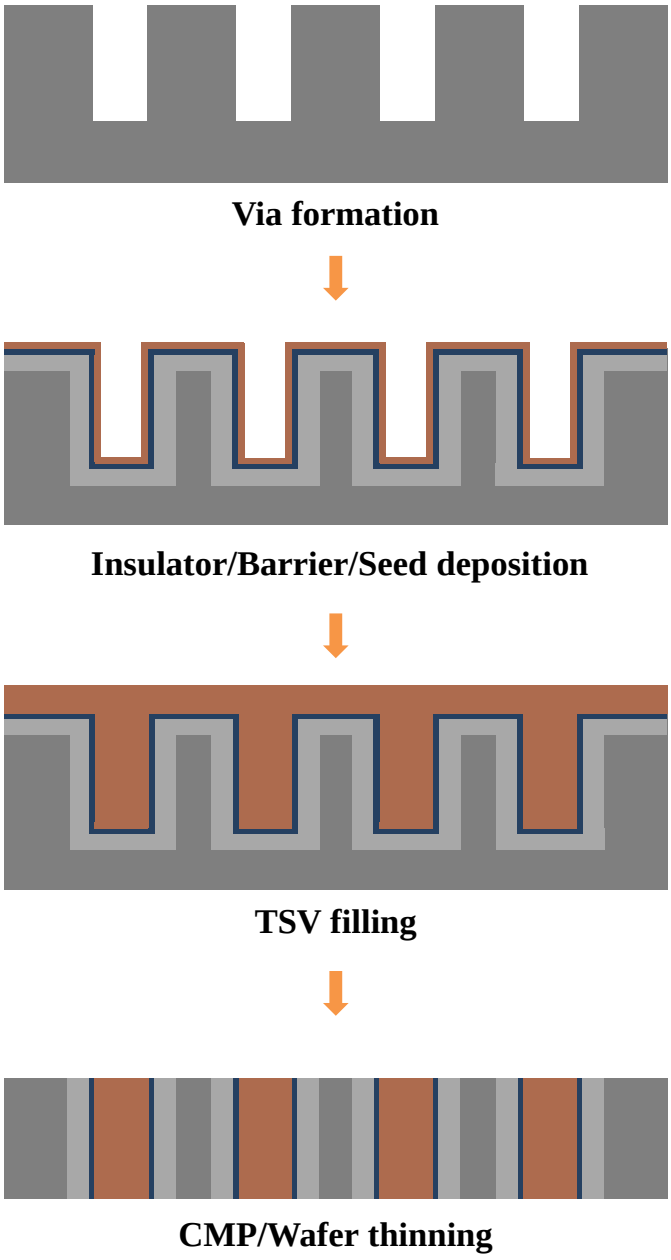

Fig. 1.5. Fabrication process flow for TSV.

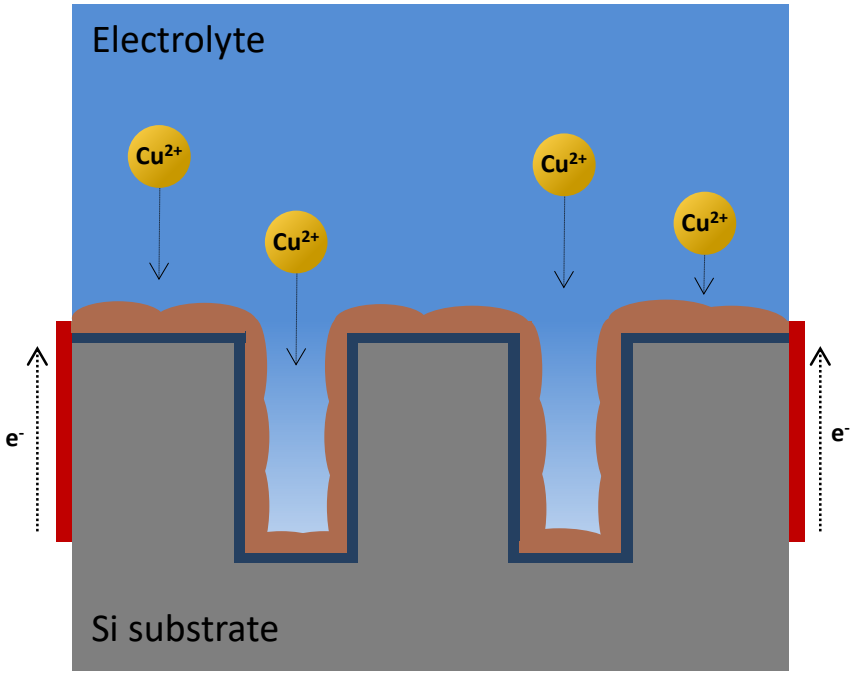

Fig. 1.6. Schematic diagram of Cu electrodeposition in TSV filling.

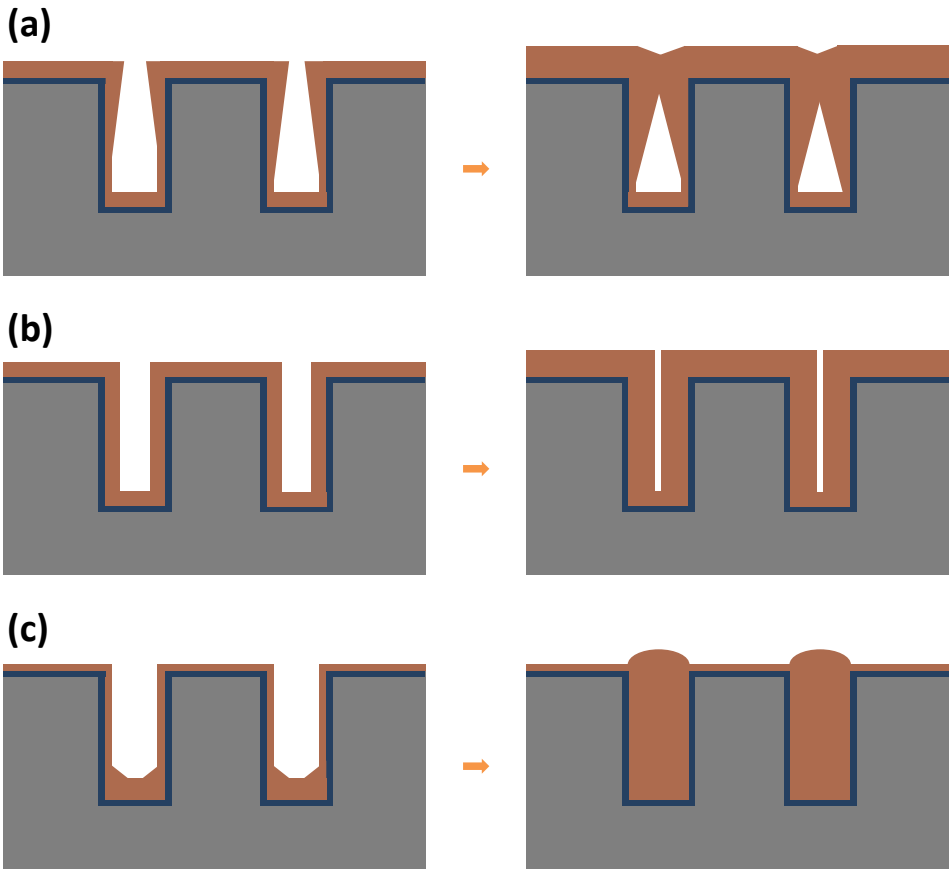

Fig. 1.7. Three types of deposition profile observed during the TSV filling.

(a) Subconformal, (b) conformal, (c) superconformal deposition.

1.3. Superfilling of TSV by Cu electrodeposition

Intensive researches have been focused on examining the filling mechanism of TSV. It was reported that adsorption characteristic of additives that depended on the convection strength enabled the void-free filling. TSV filling is commonly conducted under the convective condition to sufficiently supply Cu^{2+} and additives inside the TSV. The forced convection is developed only near the top surface of the TSV due to the high-aspect-ratio structure. The effect of forced convection gradually decreases along the TSV depth. It was reported that the convection could be neglected within the depth of 60% from the bottom, when convection was applied by rotating the TSV wafer of 20 μm diameter and 120 μm depth under 1,000 rpm.[51] It is reasonable to consider that the gradual change in convection strength along the depth can affect the adsorption behavior of the additives. The adsorption strength of an additive, sulfonated diallyl dimethyl ammonium chloride copolymer (SDDACC), is proportional to the convection power.[52-54] SDDACC strongly inhibits Cu deposition near the top of the TSV, while weakly inhibits near the bottom, as the effect of convection decreases on the TSV bottom. In addition, concentration gradient of the additive is developed during the electrodeposition since the flux of the additive is slower than its consumption or

incorporation rate. The locally different surface coverage of SDDACC results in the deposition of Cu from the bottom and side walls, zipping up the TSV with V-shaped profiles as shown in Fig. 1.8.[54] The V-shaped cross section was also observed with the addition of Janos Green B (JGB) which shows convection-dependent adsorption characteristic.[55-56]

Recently, extreme bottom-up filling of TSV by adding a single additive, suppressor, was reported.[57] Cu^{2+} is coordinated by 6 water molecules in the aqueous solution, forming an octahedral hydration structure. In the presence of sulfate, the sulfate anion and water molecule stabilize the free Cu^{2+} in the state of $Cu^{2+}SO_4^{2-}(H_2O)_5$.[58] The anion and water molecule is released during the reduction of aquo Cu^{2+} complex to Cu metal.[57]

$$Cu^{2+}(H_2O)_x(SO_4^{2-})_y + e^- \rightarrow Cu^{+}(H_2O)_z(SO_4^{2-})_n + (x-z)H_2O + (y-n)SO_4^{2-} \quad (1.5)$$

$$Cu^{+}(H_2O)_z(SO_4^{2-})_n + e^- \rightarrow Cu + zH_2O + nSO_4^{2-} \quad (1.6)$$

The released water remains very near the electrode surface, perturbing the adsorption of polymeric suppressor that contains hydrophobic parts. Based on the theory, TSV filling was achieved with the single addition of Tetronic 701 (average molecular weight:

3,400). With the addition of Tetronic 701, Cu electrodeposition on the top surface is significantly inhibited by the adsorbed suppressor. However, Cu^{2+} reaches the bottom of the TSV faster than the suppressor since the molecular weight of Tetronic 701 is 20-time higher than that of aquo Cu^{2+} complex. The water of solvation released during Cu deposition causes the Cu surface to become hydrophilic and prevents the formation of a blocking suppressor layer.[59-61] The positive feedback enables the bottom-up growth with a flat growing surface as shown in Fig. 1.9.[57, 59-61] The bistable adsorption of suppressor is further applicable to the TSV filling of Zn, Sn, and Au.[62-64]

Bottom-up filling was also achieved by artificially developing a SPS-rich bottom condition. In order to reinforce the adsorption of SPS on the bottom, Ta layer of thickness thinner than 5 nm was deposited by PVD only on the TSV surface.[65-66] Cu deposition was extremely suppressed on the Ta surface, while SPS was accumulated on the bottom. The locally increased deposition rate on the bottom allowed bottom-up filling in the Ta-capped TSV process. Furthermore, investigation using a reverse current was introduced to selectively deactivate the accelerator on the top surface.[67-69] The SPS adsorbed on the top surface was desorbed by applying reverse current, in company with the dissolution of CuCl which vigorously occurred under the strong convection. By optimizing the condition, SPS adsorbed on the bottom remained during

the reverse-current step since dissolution of CuCl was severely suppressed in the nearly stagnant condition of the bottom. Bottom-up filling was achieved by developing the SPS-rich bottom.

Either method of Ta-capped TSV or selective accelerator deactivation by reverse-pulse contributes to the formation of accelerator-rich bottom. However, both methods require additional process steps delaying the total fabrication rate of TSV-based chips. TSV filling performance can be improved, without any additional processes, just by optimizing the additive chemistry. Additive chemistry which controls the local deposition rate gives rise to bottom-up filling. Thus, studies on the effect of the additives should be preceded before conducting the TSV filling.

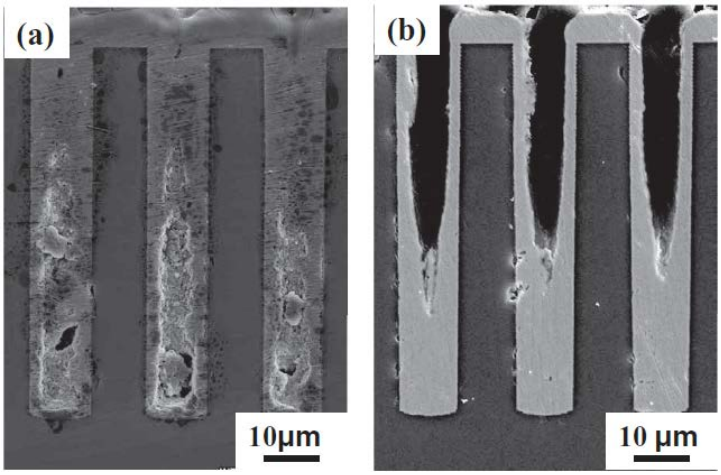

Fig. 1.8. Cross-section images of TSV after the Cu electrodeposition by adding (a) 0 ppm and (b) 1.5 ppm of SDDACC (Ref. 54).

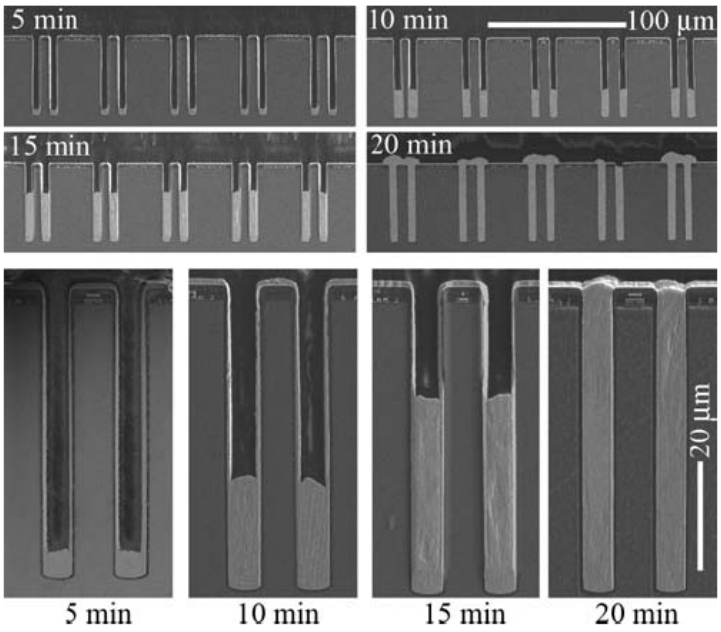

Fig. 1.9. Cross-section images of TSV after the Cu electrodeposition by adding 10 μM of Tetronic 701 (Ref. 57).

1.4. Effect of the leveler on the TSV filling

The additives listed in Table 1.2 controls the local deposition rate of Cu, thereby enabling the bottom-up filling of sub-100 nm trenches as described by CEAC model. However, the suppressor alone may not sufficiently inhibit Cu deposition on the top surface of the TSV, which has hundredfold larger dimensions in the diameter (a few micrometer), until the end of the TSV filling. As shown in Fig. 1.10, Cu is deposited on the top surface and on the corner of the TSV entrance with the addition of suppressor and accelerator. The pinch-off is commonly observed in TSV filling with the two additives. An additional additive chemistry is required to improve the inhibition on the top.

The leveler shows high adsorption density on the protrusion and low on the recess. Thus, the leveler produces thicker metal deposits in microrecesses and thinner deposits in microprotrusions, resulting in a levelled surface.[70] The leveler can be efficiently used in metallization of TSV, since the protruding features whose dimension is a few ~ a few tens of μm (that is, order of the diffusion layer thickness) are selectively inhibited by the leveler.

The selective adsorption of leveler is explained by two primary mechanisms: diffusion-controlled mechanisms and non-diffusional mechanisms.[71] In the diffusion-controlled mechanisms, the adsorption of the leveler is determined by mass transfer rate. More levelers diffuse to the elevations rather than the recesses because the distance from boundary layer to the elevations is shorter. The selectively high adsorption density of levelers on the protrusion enables the levelled surface during the metal electrodeposition.[70,72-73] The diffusion-controlled mechanism also explains the adsorption density of the leveler determined by a forced convection. The convection reduces the thickness of boundary layer, thereby increasing the adsorption density of the leveler.[74] As discussed in Chapter 1.3, the effect of convection gradually decreases from top to bottom of the TSV, which implies that the surface coverage of leveler also decreases along the TSV depth. The selectively high adsorption density of the leveler due to the fast mass transfer on the top enables the bottom-up filling of TSV.

In some cases, the effect of leveler is not explained simply by the diffusion-controlled mechanisms. Research has proposed non-diffusional mechanism in order to complement the adsorption of leveler,[71] which is described by (i) electrosorption showing 'current density sensitive' characteristic,[75] (ii) mechanisms with complex formation,[76] (iii) ion-pairing mechanisms,[77] and (iv) chemical filming,[78] etc. In aspect

of TSV filling, the non-diffusional mechanism of (i) electrosorption gives a useful description in explaining the filling mechanism. In the ‘current density sensitive’ mechanism, the local current density (or local overpotential) determines the adsorption of the leveler. In the metal electrodeposition, the current density at the protrusion locally increases due to the relatively thinner boundary layer.[73] Furthermore, it was reported that electric field was concentrated at the via opening, especially at the opening-edge.[30,79] According to the ‘current density sensitive’ mechanism, the leveler can be preferentially adsorbed on the protrusion where the local current density is high, which induces metal deposition selectively on the recessed sites. It explains the removal of overhang in TSV filling with the addition of leveler. Therefore, it is very important to develop levelers of new molecular structures in order to improve the filling performance.

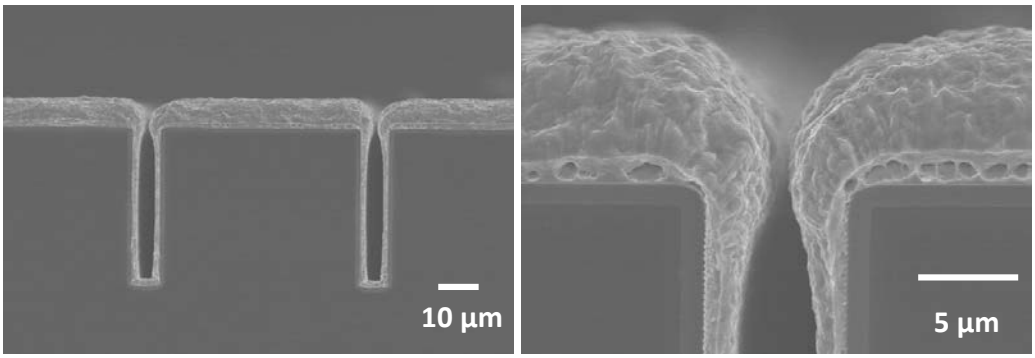

Fig. 1.10. Cross-section images of Cu-filled trenches with the addition of accelerator (SPS) and suppressor (PEG/PPG) without any leveler. Overhang was observed at the trench opening.

1.5. Purpose of this study

It is obvious that bottom-up filling is achieved with the strong suppression on the top accompanying the weak suppression or dominant acceleration on the bottom, as shown in Fig. 1.11. Various kinds of levelers reported previously are listed in Fig. 1.12.[54,80-83] The reported levelers commonly contain nitrogen atoms in the form of tertiary amines or quaternary ammonium salts. In this study, new kinds of levelers are synthesized and introduced based on the molecular structures of levelers reported previously. By adding the levelers, TSV is galvanostatically filled in the three-additive system composed of accelerator, suppressor, and leveler. After that, the filling performance is improved by modifying the deposition mode or additive chemistry.

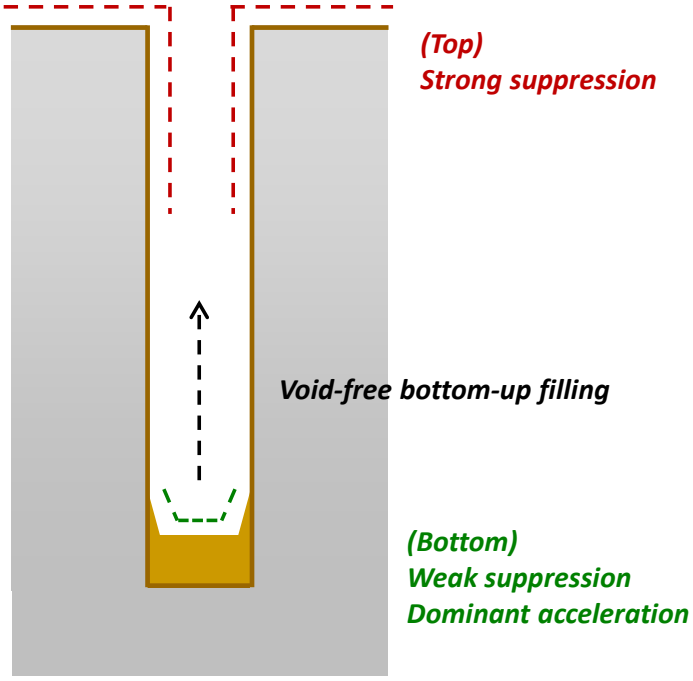

Fig. 1.11. Schematic diagram of the model for void-free and bottom-up filling.

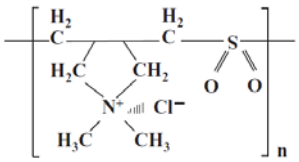

SDDACC (Ref. 54)

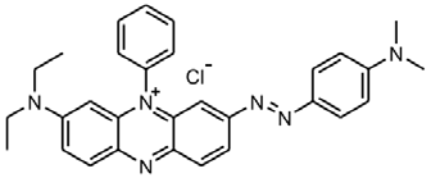

Janus Green B (Ref. 80)

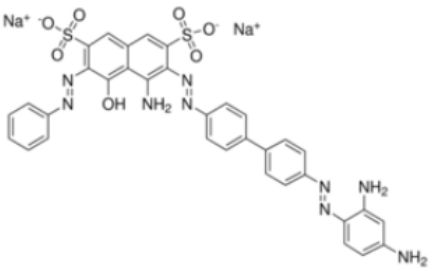

Diazine Black (Ref. 80)

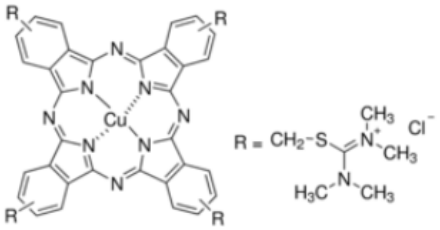

Alcian Blue (Ref. 81)

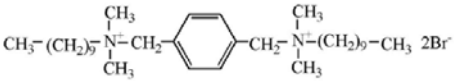

Bis-*N*,*N*,*N*-decyldimethyl-p-xylylenediammonium dibromide (Ref. 82)

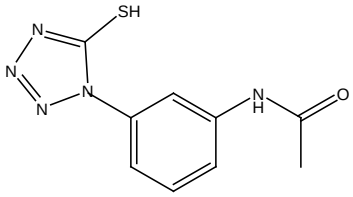

1-(3-Acetamide)phenyl -5-mercaptotetrazole (Ref. 83)

Fig. 1.12. Molecular structures of the levelers reported in papers.

CHAPTER II

Experimental

2.1. Experimental in the three-additive composition

2.1.1. Basic experimental conditions: electrolyte, additives and electrode system

A standard electrolyte composed of 1.0 M CuO_4, 0.5 M H_2SO_4, and 1.4 mM HCl was used for the Cu electrodeposition. 10 μM of SPS and 50 μM of PEG/PPG (average molecular weight: 1,100) were used as the accelerator and suppressor, respectively. Four kinds of organic additives were synthesized by professor Y. G. Kim's group to be used as the leveler (Table 2.1): (1) α,ω-bis(*N*,*N*,*N*-trimethylammoniomethyl)triethylene glycol diiodide, (2) α,ω-bis(*N*,*N*,*N*-allyldimethylammoniomethyl)triethylene glycol diiodide, (3) 1,5-bis(2-*N*,*N*,*N*-trimethylammonioethyl)glutarate diiodide, (4) 1,10-bis(3-(*N*,*N*,*N*-trimethylammonio)-2-propanol-oxy)decane diiodide. The four additives was noted as Lev(1), Lev(2), Lev(3), and Lev(4), respectively, for a simple notation. All the four additives contain two quaternary ammonium salts and two iodide ions in

common. Lev(1) has ether and hydroxyl functional groups with a symmetrical structure. Lev(2) contains allyl groups at both ends of the molecule rather than the methyl groups although the molecular structure of Lev(2) is quite similar to that of Lev(1). Lev(3) has two ester groups without any hydroxyl groups. The length of carbon chain increases in Lev(4) containing decane.

Levelers having various halide ions were additionally synthesized to compare the effect of halide ions. The molecular structures of the levelers synthesized by changing the iodide ion in Lev(2) to chloride or bromide ion are described in Table 2.2. The levelers of different halide ions are noted as Lev(2)-X (X = Cl, Br, and I). Finally, NaI was used instead of the synthesized levelers in order to distinctively examine the effect of iodide ion on the Cu electrodeposition.

Cu electrodeposition was conducted in the three-additive composition by adding 50 μM of the synthesized levelers (Lev(1) ~ Lev(4) and Lev(2)-X) with SPS and PEG/PPG. NaI was added with the concentration of 100 μM for the TSV-scaled trench filling. The temperature of the electrolyte was maintained at 25°C by using a thermostat.

All the experiments were performed with a three-electrode system. The schematic diagram of electrode setting is displayed in Fig. 2.1. Cu-surface electrodes, electronic

grade Cu rod, and Ag/AgCl (KCl saturated) were used as the working, counter, and reference electrode, respectively. Detailed specification of the working electrodes will be discussed in the associated Chapter later. The three electrodes were immersed into the electrolyte followed by applying current or potential to progress Cu electrodeposition. The electrodeposition was conducted using a PAR 273A potentiostat (EG&G Princeton Applied Research Corporation).

2.1.2. Electrochemical analysis

The electrochemical behavior of the additives was investigated by linear sweep voltammetry (LSV) and cyclic voltammetry (CV) by using Cu rotating disk electrode (RDE) with an area of 0.196 cm^2. The surface of the Cu RDE was polished by 2000-grit sand papers to expose a fresh Cu surface before every electrochemical analysis. LSV was performed in the potential range from 150 mV ~ -350 mV with a scan rate of 10 mV/s. The sweeping range in conducting CV was reduced as 150 mV ~ -150 mV or ~ -200 mV (10 mV/s) to observe the adsorption characteristics of the additives more clearly in the charge-transfer-controlled region. RDE was rotated with a speed of 0 and 900 rpm to replicate the convective conditions of TSV bottom and top, respectively.

2.1.3. TSV-scaled trench filling

A patterned wafer containing two sizes of trenches with similar dimensions to TSV was used as the working electrode; widths of 7 and 9 μm and a depth of 40 μm. The trenches were lined with Cu seed layer (PVD, 1.2 μm at the top, 270 nm at the bottom)/Ta (PVD, 25 nm)/TaN (PVD, 50 nm)/SiO_2. Wafers fragmented by 1.5 X 1.5 cm^2 were immersed in ethanol for 30 s to improve the surface wettability. The wetted wafers were loaded in a Teflon holder with an exposed area of 1 cm^2, and Cu electrodeposition was conducted in the electrolyte. Current was applied galvanostatically or in the form of step for the filling. Galvanostatic filling was performed by applying a constant current density of 15 mA/cm^2 for 600 s. Step current was applied with the first step current of 15 mA/cm^2 and the second step of 30 mA/cm^2, 50 mA/cm^2, and 70 mA/cm^2. The total deposition charge was maintained as 9,000 mC. The filling was performed at 900 rpm to efficiently supply the electrolyte and additives inside the trenches. The cross-sections of the trenches were observed by field emission scanning electron microscopy (FESEM, S-4800, Hitachi).

2.1.4. Cu film deposition

Cu film was deposited by adding SPS, PEG/PPG, and one of the levelers listed in Table 2.1, to compare the effect of the levelers on Cu electrodeposition. A blanket wafer composed of Cu seed layer (50 nm, PVD)/Ta (35 nm, PVD)/SiO_2 was used as the working electrode. Before the electrodeposition, the native oxide of the blanket wafer was removed by immersing it in an aqueous solution of 0.03 M citric acid and 0.034 M potassium hydroxide for 2 min. The oxide-etched coupon wafer was dipped into the electrolyte containing 10 μM SPS, 10 μM PEG/PPG, and 10 μM levelers. Note that the concentrations of suppressor and leveler were diluted to one-fifth for replicating the surface concentration of each additive at the bottom of trenches.[78] A constant current density of 15 mA/cm^2 was applied with a deposition charge of 2000 mC/cm^2.

After the film deposition, X-ray diffractometer (XRD, D8 Advance, Bruker) having Cu Kα 1 (0.154 nm) was used to study the crystallographic orientations. The radiation had a penetration depth of about 2.8 μm to 5.4 μm at two-theta of 30˚ to 60˚, respectively, considering depth for 63% of the diffracted beam. All the XRD measurements were performed with theta-two theta scans with the incident angle equal

to the reflection angle. The scan rate was 3°/min for the two-theta range of 30° - 60°. Sheet resistance and film thickness were measured by a 4-point probe (CMT-SR1000N, Chang Min Tech Co.) and by FESEM, respectively, to calculate resistivity.

Table 2.1. Molecular Structures of the Synthesized Iodide-based Levelers

Synthesized Levelers	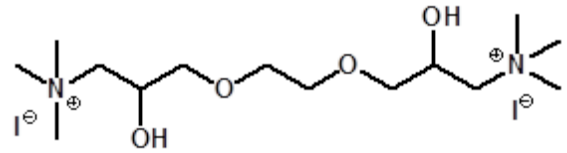 α,ω-bis(*N*,*N*,*N*-trimethylammoniomethyl)triethylene glycol diiodide **Lev(1)**
	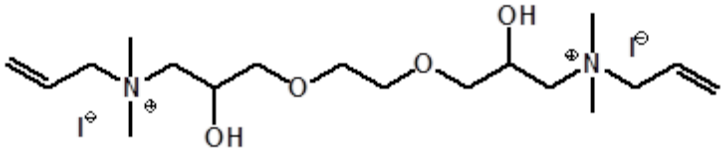 α,ω-bis(*N*,*N*,*N*-allyldimethylammoniomethyl)triethylene glycol diiodide **Lev(2)**
	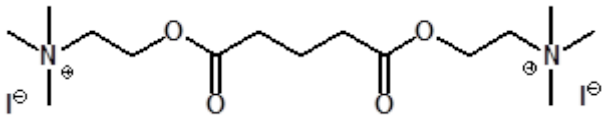 1,5-bis(2-*N*,*N*,*N*-trimethylammonioethyl)glutarate diiodide **Lev(3)**
	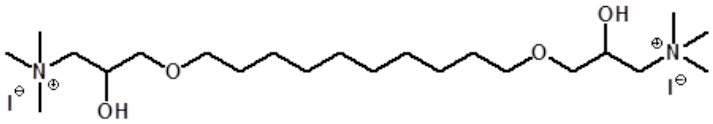 1,10-bis(3-(*N*,*N*,*N*-trimethylammonio)-2-propanol-oxy)decane diiodide **Lev(4)**

Table 2.2. Molecular Structures of Lev(2)-X (X = Cl, Br, I)

Synthesized Levelers	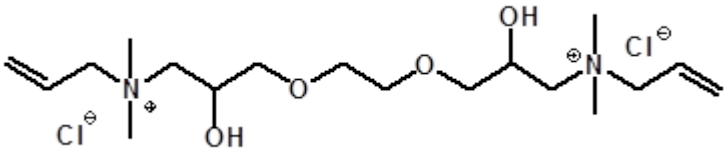 α,ω-bis(*N*,*N*,*N*-allyldimethylammoniomethyl)triethylene glycol dichloride **Lev(2)-Cl**
	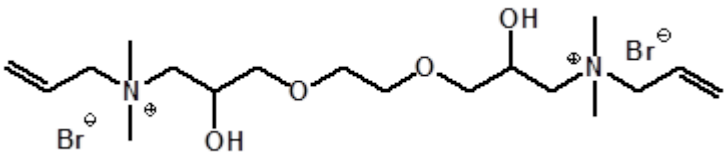 α,ω-bis(*N*,*N*,*N*-allyldimethylammoniomethyl)triethylene glycol dibromide **Lev(2)-Br**
	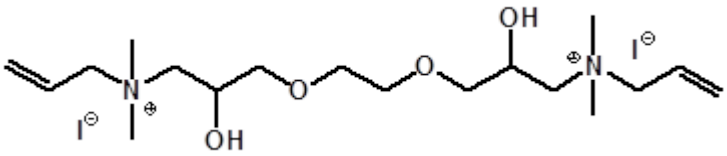 α,ω-bis(*N*,*N*,*N*-allyldimethylammoniomethyl)triethylene glycol diiodide **Lev(2)-I**

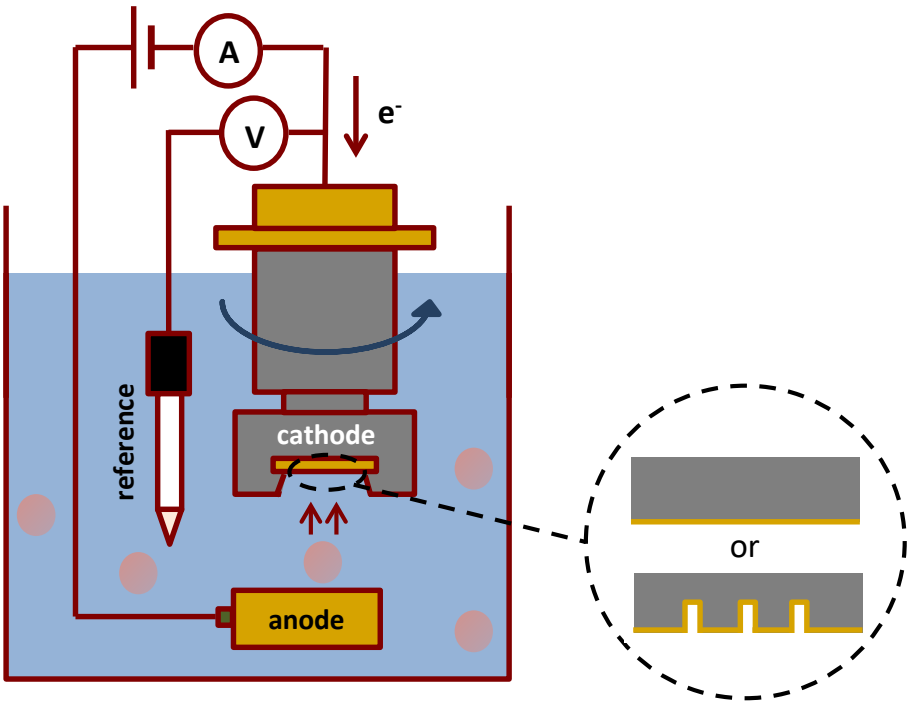

Fig. 2.1. Schematic diagram of the three-electrode system for the Cu electrodeposition.

2.2. Experimental in the four-additive composition

2.2.1. Electrochemical analysis

The four-additive composition includes 10 μM SPS, 50 μM PEG/PPG, 400 μM NaI, and 10 ~ 100 μM TU. To examine the electrochemical interaction of TU with other additives, LSV and CV were performed in the same voltammetric condition as described in Chapter 2.1.2. Chronoamperometry was conducted to additionally investigate the effect of additives by applying -200 mV (vs. Ag/AgCl) for 50 s. -200 mV corresponding to the averagely measured potential during the TSV filling was used.

2.2.2. TSV filling

Columnar TSV of 5 μm in diameter and 60 μm in depth was used as the working electrode in the four-additive system. The TSV was lined with Cu seed layer (PVD, 600 nm)/Ta (PVD, 300 nm)/SiN (250 nm). All the experimental conditions are the same as Chapter 2.1.3, except the applied current density. Current density of 1 mA/cm^2 or 2 mA/cm^2 was applied for 2200 s or 1100 s, respectively, by the potentiostat. The

cross-sections of the Cu-filled TSV was observed by optical microscopy, after molding the specimen in an acrylic resin and mechanically polishing the molded sample.

CHAPTER III

Results and Discussion

3.1. TSV filling in the three-additive composition

3.1.1. Filling mechanism in the three-additive composition

One of the organic levelers, noted as Lev(1) in Table 2.1, was used to identify the possibility of the leveler for the void-free TSV filling. Based on the molecular structures of levelers reported previously, Lev(1) containing two quaternary ammonium cations with iodide anions was synthesized. The single effect of SPS, PEG/PPG, or Lev(1) was electrochemically investigated as shown in Fig. 3.1. LSV was performed under 0 and 900 rpm to replicate the local convective condition on trench top and bottom, respectively. Similar voltammograms were obtained irrespective of the rotating speed when 10 μM of SPS was added until -50 mV (vs. Ag/AgCl). As the effect of mass transfer becomes dominant within the potential range more negative than -50 mV, the current density under 900 rpm is measured higher than that of 0 rpm. The efficiently supplied Cu^{2+} to the electrode surface under 900 rpm contributes to the

higher current in the mass-transfer controlled region. However, the current discrepancy was not observed with the addition of 50 μM PEG/PPG. Very similar current densities were measured between 0 rpm and 900 rpm within the given sweeping range of 150 mV ~ -350 mV. Since PEG/PPG severely suppresses the Cu deposition, the deposition rate is governed by charge-transfer rate even up to -350 mV. In the case of Lev(1), it inhibits Cu deposition up to -100 mV under 900 rpm, while the inhibition power dramatically decreases in the stagnant condition of 0 rpm.

The adsorption characteristic of Lev(1) that depends on the convective force is explained by diffusion layer thickness according to the rotation speed. The Nernst diffusion layer is described as below in the RDE system,[84]

$$\delta_O = 1.61 D_O^{1/3} \omega^{-1/2} \nu^{1/6} \tag{3.1}$$

wehre δ_O is the diffusion layer thickness (μm), D_O is the diffusion coefficient of the reactant (cm^2/s), ω is the angular velocity of RDE (rad/s), and ν is the kinematic viscosity of the solution (cm^2/s). The diffusion coefficient of Cu^{2+} is calculated by using the Levich equation (3.2) that is derived by assuming the steady-state,[84]

$$i_{l,c} = 0.62nFAD_O^{2/3}\omega^{1/2}\nu^{1/6}C_O^* \quad (3.2)$$

where $i_{l,c}$ is the limiting current (A), n is the number of electrons involved in the reduction reaction, F is the Faraday constant (C/mol), A is the area of the RDE (cm^2), and C_O^* is the bulk concentration of the reactant (mol/cm^3). The limiting current was experimentally measured from linear sweep voltammogram at certain rotating speeds in order to calculate the diffusion coefficient of Cu^{2+}. In this system, the diffusion coefficient of Cu^{2+} was calculated as 7.54 (±0.16)×10^{-6} cm^2/s when using the kinematic viscosity of the water as the solvent (0.01 cm^2/s).

The diffusion layer thickness at 0 rpm can be calculated by assuming the pseudo-steady-state. It was calculated as 155.1 (±1.1) μm from the Eq. 3.2 by using the experimentally measured limiting current at 0 rpm. In the presence of convection, diffusion layer thickness was calculated as 15.10 (±0.11) μm at 900 rpm from the Eq. 3.1. More than 10 times shorter diffusion length under the convection corresponds with the faster mass-transport rate of the species in the electrolyte. The time required for the Lev(1) to reach the electrode surface through the diffusion layer is calculated as 60.2 (±1.1) s and 0.570 (±0.011) s at 0 rpm and 900 rpm, respectively, by using $\delta = \sqrt{Dt}$ (conventionally reported diffusion coefficient for the leveler, 4×10^{-6} cm^2/s, was used.[46]).

The Lev(1) is rapidly transferred to the electrode surface through the short diffusion layer under 900 rpm, thereby showing the strong inhibition based on the high surface coverage. The convection-dependent adsorption characteristic of Lev(1) indicates that it can help the selective inhibition on the top of TSV where forced convection exists.

Prior to the TSV-scaled trench filling, the interaction of the additives was electrochemically investigated as shown in Fig. 3.2. The sole addition of SPS did not show a clear acceleration. The current density with the addition of SPS-Lev(1) followed that with the single addition of Lev(1), which implied that SPS did not make interactive relation with Lev(1). SPS added with PEG/PPG exhibited an acceleration by displacing the pre-adsorbed blocking suppressor layer (Fig. 3.2c and d).[85-86] In the combination of PEG/PPG and Lev(1), Cu electrodeposition was effectively suppressed by the co-adsorption of the two additives. The inhibition power was enhanced compared to that with the sole addition of PEG/PPG or Lev(1), under both 0 rpm and 900 rpm. The co-adsorption of the suppressor and leveler may accompany the molecular interaction, causing the synergistically enhanced inhibition. In the combination of SPS-PEG/PPG-Lev(1), the addition of SPS obviously promoted Cu deposition compared to that of PEG/PPG-Lev(1) under 0 rpm. However, the effect of SPS disappeared in the three-additive system under 900 rpm, since strongly adsorbed

PEG/PPG-Lev(1) hindered the displacement adsorption of SPS.

To sum up the results of electrochemical analyses, the synergetic interaction of PEG/PPG-Lev(1) efficiently inhibits Cu deposition under 900 rpm, that is, on the top surface of TSV. The inhibition layer is not disrupted by the addition of SPS with the forced convection, which indicates that Cu deposition on the top surface will be sufficiently blocked. Simultaneously, SPS accelerates Cu deposition rate on the bottom of stagnant condition by naturally displacing the adsorbed PEG/PPG. It is reasonable to consider that Cu deposition selectively progresses on the bottom during the filling in the presence of the organic Lev(1) with SPS and PEG/PPG.

LSV was performed by varying the concentrations of Lev(1) from 10 μM to 50 μM in the three-additive composition. As shown in Fig. 3.3, the inhibition is slightly improved under 0 rpm as the concentration of Lev(1) increases. The effect of Lev(1) is found to be saturated, under 900 rpm, just with the concentration of 10 μM. TSV-scaled trench filling was conducted by applying 15 mA/cm^2 under 900 rpm, as shown in Fig. 3.4. Filling failed with the addition of 10 μM or 25 μM Lev(1) and voids formed near the bottom; while the increased concentration of 50 μM Lev(1) enabled void-free filling. Insufficient inhibition with the low concentrations of Lev(1) does not block the metal deposition on the side walls adjacent to the bottom. The Cu grown

from the side walls impedes the diffusion of Cu^{2+} to the bottom surface and hinders the bottom-up growth. The composition of the three-additive system for the void-free filling was selected as 10 μM SPS, 50 μM PEG/PPG, and 50 μM Lev(1).

The filling profile by applying 15 mA/cm^2 based on the filling time is shown in Fig. 3.5. Fig. 3.5a shows that Cu deposition is promoted at the bottom corner in the early stage of filling. The black arrows indicate the accelerated Cu deposition on the concave structure. The surface coverage of SPS increases by the accumulation, similar to the description of CEAC model, promoting Cu reduction at the bottom corner.[49] Furthermore, the low surface coverage of PEG/PPG and Lev(1) at the bottom by the slow diffusion rate and negligible convection, respectively, contributes to the adsorption of SPS at the bottom. Consequently the growing surface is established at the bottom of trenches through the accumulation of SPS. On the contrary, the top surface and more than half of the trench side walls from the top clearly remains as the seed layer without any Cu deposition. PEG/PPG and Lev(1) shows the synergetic inhibition near the top surface where the forced convection is applied. The growing surface formed at the bottom and the strong inhibition at the top enables the bottom-up filling without voids.

The potential-time curve measured during the filling gives more information on

understanding the filling process. As shown in Fig. 3.6. The potential curve is divided into four remarkable regions: (i) abrupt increase in the overpotential (negative shift of the potential) up to 13 s, (ii) slight depolarization (positive shift, 13 ~ 50 s), (iii) gradual polarization (50 ~ 200 s), and (iv) stabilized potential (after 200 s). (i) PEG/PPG and Lev(1) are promptly adsorbed on the top and side walls of the trenches at the initial stage, polarizing the electrode. (ii) SPS that begins to be activated at the bottom promotes Cu deposition, as shown in Fig. 3.5a. Slight depolarization occurs through the accumulation of SPS. (iii) As the growing surface proceeds from the bottom to the top, the effect of PEG/PPG and Lev(1) increases under the forced convection near the top. It again depolarizes the electrode in this region. (iv) The surface coverage of the additives is stabilized as the high adsorption density of SPS on the growing surface and of PEG/PPG and Lev(1) on the top and side walls. The bottom-up growth continues in the region (iv) until the end of the filling.

Filling with two combinations of the additives was performed to support the investigation on the role of each additive. The cross-section images and potential-time curves are presented in Fig. 3.7 (SPS-PEG/PPG), Fig. 3.8 (SPS-Lev(1)), and Fig. 3.9 (PEG/PPG-Lev(1)).The effect of the additives can be examined from the filling results, although filling fails in the two-additive systems

In the case of filling with SPS and PEG/PPG shown in Fig. 3.7, sharp polarization until 20 s followed by depolarization was observed. PEG/PPG rapidly forms the suppressing layer with Cl^- and polarizes the electrode surface in the early stage of the deposition. After that, SPS gradually displaces the pre-adsorbed PEG/PPG during the electrodeposition. The electrode is depolarized as the surface coverage of SPS increases. The promoted deposition at the bottom corner supports the accumulation of SPS. However, filling fails since the addition of PEG/PPG without Lev(1) does not form a strong inhibiting layer, which allows Cu deposition on the top and the side walls.

The potential profile measured with the addition of SPS and Lev(1) is exhibited in Fig. 3.8. The electrode is only depolarized unlikely to the result of SPS-PEG/PPG. As can be expected from the potential profile, no evidence for the accelerated Cu deposition at the bottom corner is observed in the cross-section images. It is concluded that no competitive adsorption occurs between Lev(1) and SPS. Cu is deposited on the side walls due to the weak inhibition of Lev(1) alone, causing the pinch-off.

The results of PEG/PPG-Lev(1) are presented in Fig. 3.9, showing entirely different filling results. The potential is negatively shifted to -275 mV (vs. Ag/AgCl) within 30 s, followed by showing nearly constant potential. The addition of PEG/PPG-Lev(1) induces the extreme polarization compared to the other two-additive systems, based on

the synergetic effect of suppressor and leveler. PEG/PPG and Lev(1) block Cu deposition inside the trenches except a very small amount of deposition at the bottom. However, bumpy Cu deposit is observed on partial top surface, although the other parts remain as free surface. Cu is deposited only the surface where the inhibition power of PEG/PPG-Lev(1) is relatively weak, while negligible deposition occurs on the other surface. The deposition nonuniformity makes the tens-of-micrometer bumpy nodulation on the top surface. Based on the results, SPS seems to enhance the uniformity of the filling by developing the growing interface through its accumulation.

In summary, a new molecular structure of leveler, containing two quaternary ammonium ions with iodide ions, was introduced in Chapter 3.1.1. The Lev(1) showed convection-dependent adsorption characteristic, meaning that the Lev(1) could selectively adsorb on the top surface of the TSV. As described in the schematic diagram of filling mechanism of Fig. 3.10, the synthesized Lev(1) synergistically inhibited Cu deposition near the top surface with PEG/PPG. The effect of PEG/PPG and Lev(1) gradually decreases from the top to the bottom: (1) slow diffusion rate of PEG/PPG due to the low diffusion coefficient, and (2) deactivation of Lev(1) in the stagnant condition of the bottom. A growing surface was developed at the bottom through the accumulation of SPS, which enabled the bottom-up filling without voids.

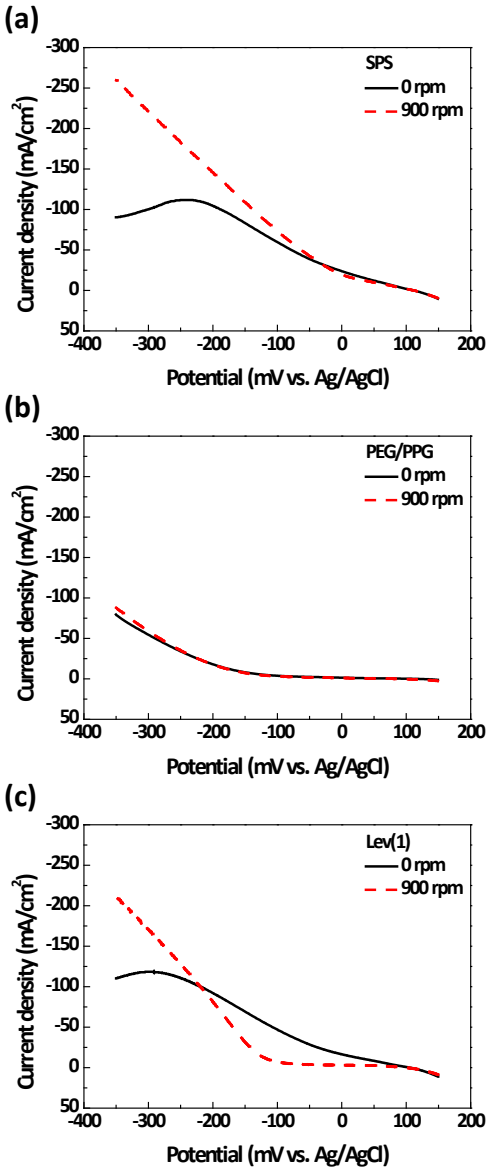

Fig. 3.1. Voltammograms obtained with the single addition of (a) 10 μM SPS, (b) 50 μM PEG/PPG, and (c) 50 μM Lev(1) under 0 and 900 rpm.

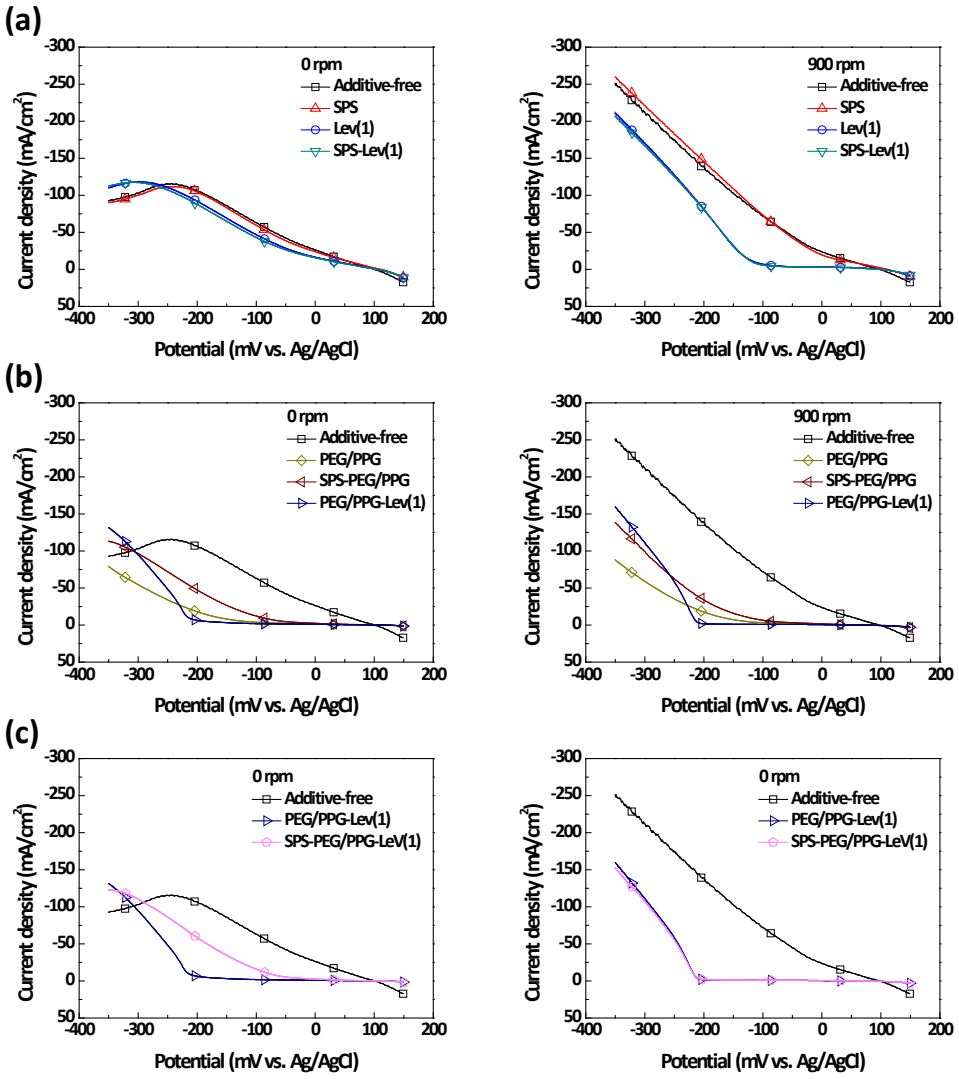

Fig. 3.2. Voltammograms obtained by combining (a) SPS-Lev(1), (b) SPS-PEG/PPG and PEG/PPG-Lev(1) to observe the displacement reaction and synergistic inhibition, respectively, and (c) SPS-PEG/PPG-Lev(1). The concentrations of SPS, PEG/PPG, and Lev(1) were 10 μM, 50 μM, and 50 μM, respectively. The left and right figures were obtained under 0 and 900 rpm of the rotating speed.

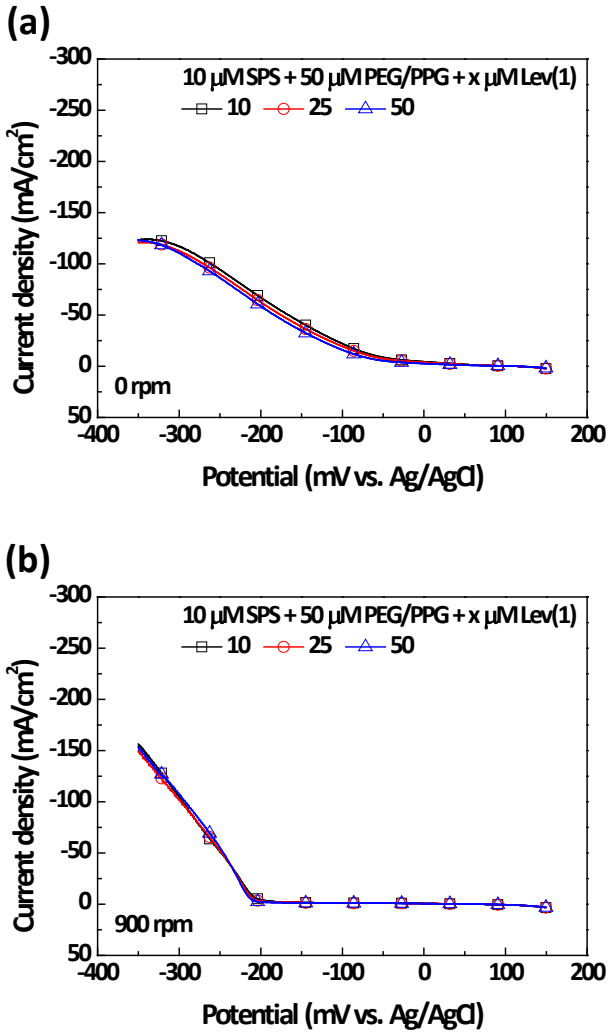

Fig. 3.3. Voltammograms obtained by adding 10 μM SPS, 50 μM PEG/PPG, and 10 to 50 μM Lev(1) under (a) 0 rpm and (b) 900 rpm.

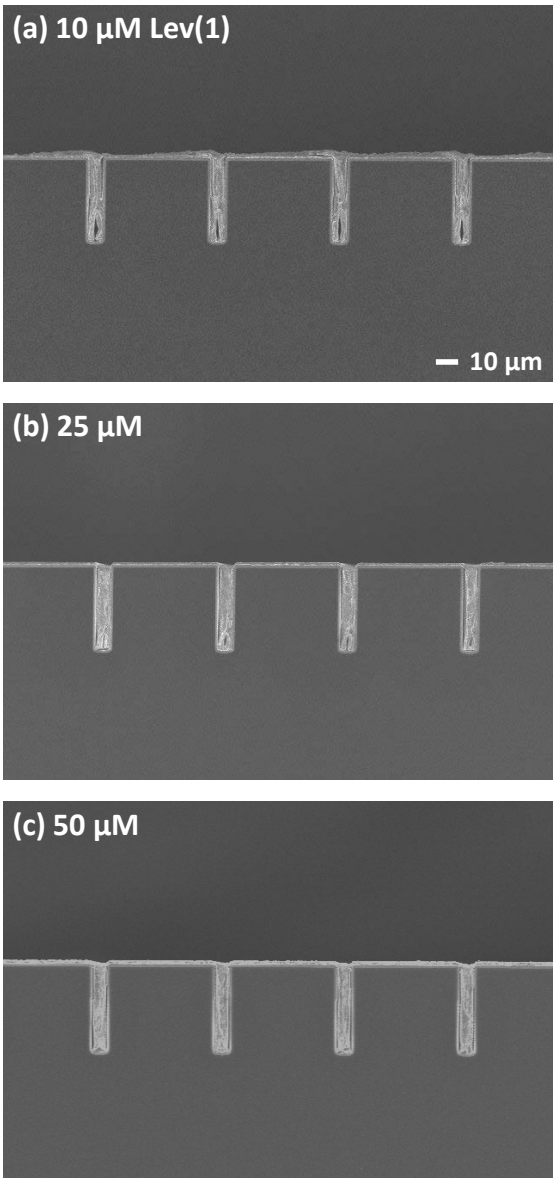

Fig. 3.4. Cross-section images of Cu-filled trenches by adding (a) 10 μM, (b) 25 μM, and (c) 50 μM of Lev(1) with 10 μM SPS and 50 μM PEG/PPG. A constant current density of 15 mA/cm^2 was applied for 600 s under 900 rpm of the rotating speed.

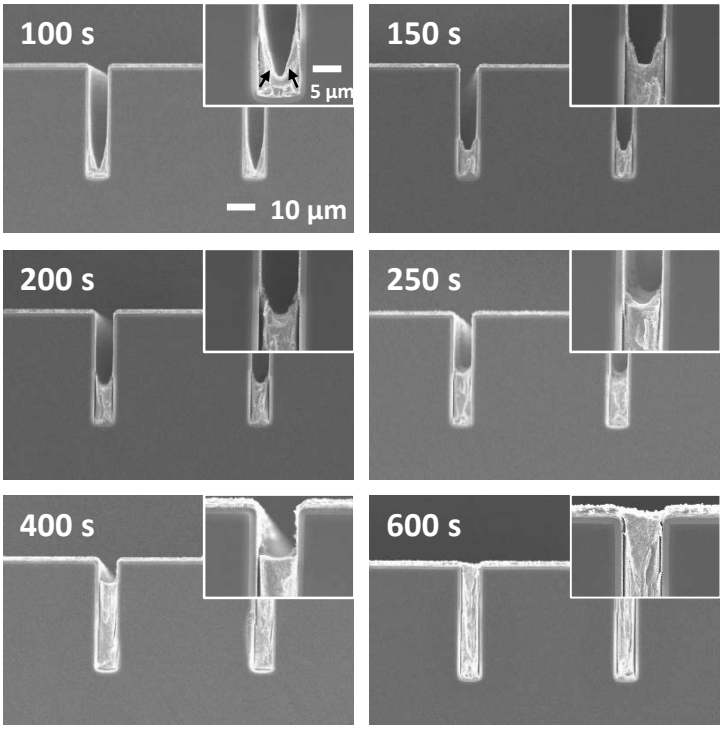

Fig. 3.5. Cross-section images of filling profiles. The trenches were filled with the addition of 10 μM SPS, 50 μM PEG/PPG, and 50 μM Lev(1) at the applied current density of 15 mA/cm^2.

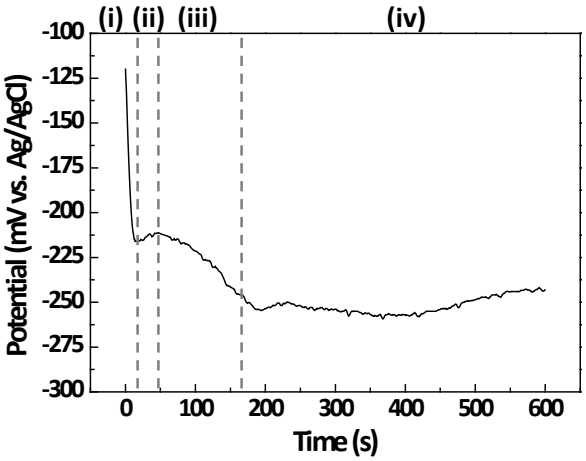

Fig. 3.6. Potential profile measured during the trench filling with the addition of 10 μM SPS, 50 μM PEG/PPG, and 50 μM Lev(1) at the current density of 15 mA/cm^2 applied for 600 s.

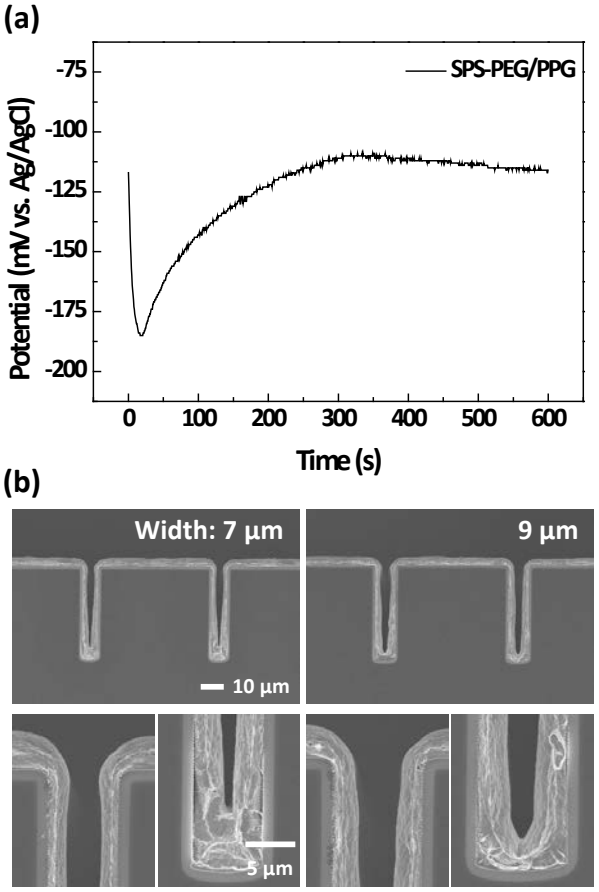

Fig. 3.7. (a) Potential profile and (b) cross-section images of trenches electrodeposited with the addition of 10 µM SPS and 50 µM PEG/PPG at the current density of 15 mA/cm^2 applied for 600 s.

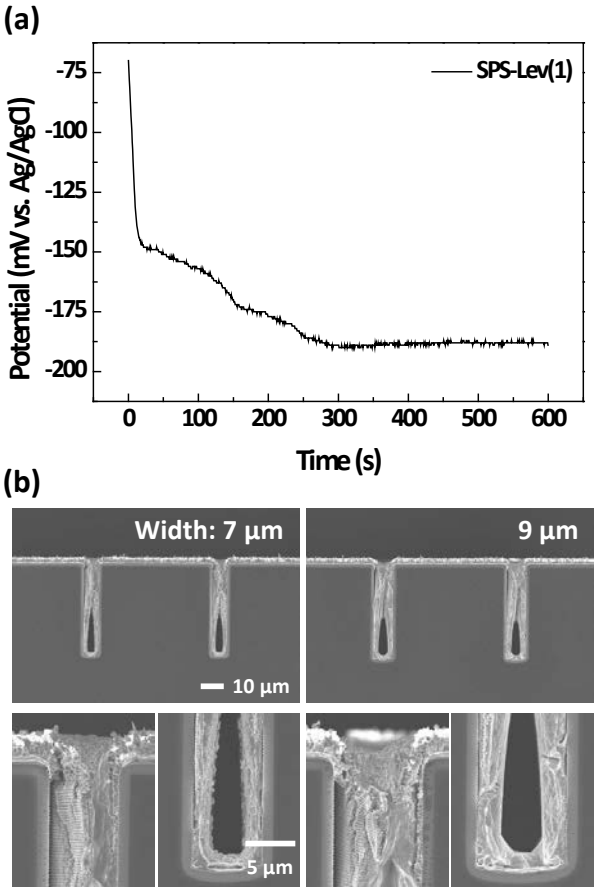

Fig. 3.8. (a) Potential profile and (b) cross-section images of trenches electrodeposited with the addition of 10 μM SPS and 50 μM Lev(1) at the current density of 15 mA/cm^2 applied for 600 s.

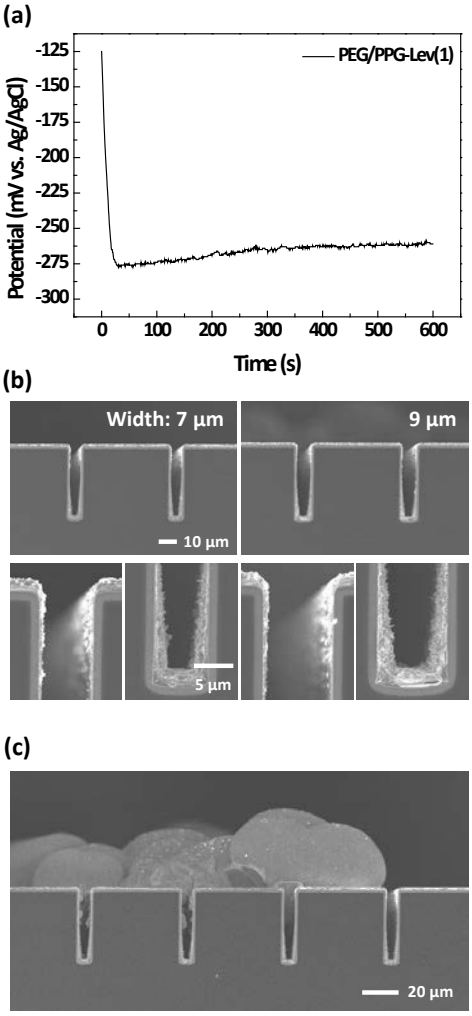

Fig. 3.9. (a) Potential profile and (b) cross-section images of trenches electrodeposited with the addition of 50 µM PEG/PPG and 50 µM Lev(1) at the current density of 15 mA/cm^2 applied for 600 s. (c) A low magnified image of the cross-section that shows the non-uniform deposition of Cu on the top surface.

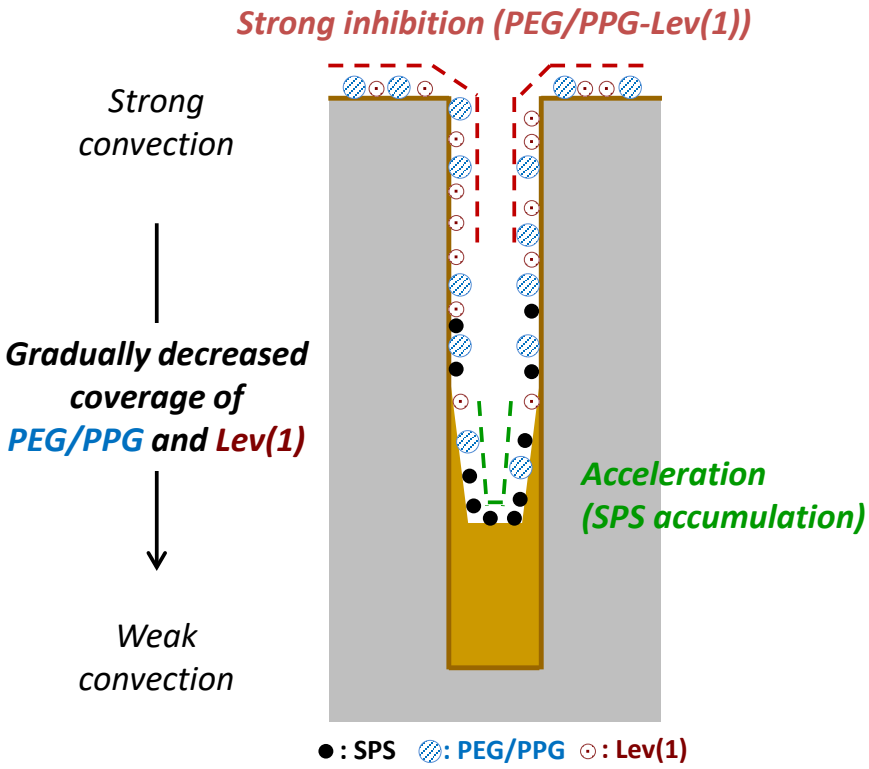

Fig. 3.10. Schematic diagrams of the filling mechanism in the three-additive composition containing SPS, PEG/PPG, and Lev(1).

3.1.2. Filling by applying step current

The effect of the synthesized Lev(1) and its applicability on the TSV filling has been studied in the previous Chapter. Along with the researches on developing new organic additives, intensive efforts are focused on reducing the filling time, as well, since TSV has micrometer dimensions demanding a long filling time. It was concluded that strong inhibition layer was formed near the top surface while the accumulation of accelerator occurred at the bottom. Based on the suggested filling mechanism, it is expected that the inhibition layer near the top surface is well-maintained even at high applied current densities, since the suppressor and the leveler are strongly bonded to the top surface under the forced convection. The filling performance can be improved by applying the step current comprising a first step (low current) to establish a growing surface and a second step (high current) to reduce the filling time. A filling method using step current deposition is introduced in this Chapter.

The intensity of the applied current generally determines the filling performance; when inappropriately high current is applied, either disruption of the adsorbed inhibitors because of the high overpotential or Cu reduction under the mass-transfer-limited condition may induce void formation.[87] The filling performance based on the

applied current intensity was investigated as shown in Fig. 3.11, with the addition of 10 μM SPS, 50 μM PEG/PPG, and 50 μM Lev(1). Void-free filling was achieved at an applied current density of ≤ 15 mA/cm^2. The applied current density of 17.5 mA/cm^2 resulted in void formation near the bottom. Since the high applied current promoted Cu reduction by detaching the inhibitors, the deposition rate of Cu on the side wall increased with higher current. The Cu growth from the side walls of the trenches combined at the middle of the trench before the completion of the bottom-up growth, forming voids near the bottom at 17.5 mA/cm^2. Therefore, the applied current density of 15 mA/cm^2, inducing void-free deposition near the bottom, was selected as the first step current.

The filling profile measured by applying 15 mA/cm^2 based on the segmented filling time is shown in Fig. 3.12 (cross-section images identical to Fig. 3.5). Successful gap-filling was achieved based on the strong suppression of Cu deposition on the top because of synergistic inhibition with the suppressor and leveler, and selective deposition of Cu at the bottom owing to the accumulation of SPS. More than half of the trench side wall clearly remained as the initial seed layer without Cu deposition, for up to 250 s. Cu was deposited on the side wall from the bottom to the point indicated by a white arrow, marked as “A”. The height of region “A”, ~18.5 μm, did not increase

from 50 to 150 s as shown in Fig. 3.12b, but began to increase when the growing surface was fully developed after 200 s. In general, the coverage of the inhibitors, composed of a suppressor and leveler, gradually decreased from the top to the bottom. The applied current selectively detached the inhibitors adsorbed onto the region “A” where the surface coverage of inhibitors was low, which initiated Cu deposition only on the region “A” of 18.5 μm height. The inhibitors strongly adsorbed onto the other areas except region “A” maintained its coverage, resisting the deposition of Cu. In addition, the accumulation of SPS at the bottom-corner accelerated the deposition of Cu, developing a concave growing surface. As shown in Fig. 3.12a, the growing surface had a sharply concave structure at 100 s of filling time. The bottom-up filling was progressed inside the concave structure to establish a growing front with higher curvature until 200 s of the filling time. After that, the height of region “A” increased as the bottom-up growth continued.

To reduce the filling time, bottom-up filling was achieved by applying 15 mA/cm^2 for 250 s at first, followed by applying higher current as shown in Fig. 3.13. Almost half of the trench was filled during the application of the first step, i.e., 15 mA/cm^2 for 250 s (Fig. 3.12a). Void-free filling continued with subsequently applied higher current of 30, 50, or 70 mA/cm^2, and the filling time was measured as 425, 355, and 325 s,

respectively. When 70 mA/cm^2 was applied, nodulation occurred on the surface of the trenches because of the extremely high current density.[88] When 50 mA/cm^2 was applied as the second step current, the filling time (355 s) was reduced by ~40% compared to constant current deposition at 15 mA/cm^2 (Fig. 3.11c, 600 s). With step current, the trenches were filled from the bottom to the midway point by applying 15 mA/cm^2 for 250 s. The inhibitors, which fully blocked the other half of the trenches, suppressed Cu deposition near the top even at a high current density of 50 mA/cm^2. However, with direct current deposition, the applied current density of just 17.5 mA/cm^2 induced void formation by detaching the low coverage of inhibitors near the bottom. Filling with step current allowed void-free filling with less filling time by applying extremely high current in the second step.

The application time for the first step current was modulated to further reduce the filling time. As shown in Fig. 3.14, the first step current density of 15 mA/cm^2 was applied for 100, 150, and 200 s, followed by 50 mA/cm^2 applied as the second step. Trenches filled by applying 15 mA/cm^2 for 100 s in the first step (Fig. 3.14a) contained voids near the bottom, whereas voids were formed at the middle of the trenches with 15 mA/cm^2 applied for 150 s as the first step (Fig. 3.14b). Only the condition of 15 mA/cm^2 (200 s) → 50 mA/cm^2 (120 s) resulted in void-free filling with a total filling

time of 320 s. With filling time of 100 s, as shown in Fig. 3.12a, the growing interface did not develop sufficiently from the bottom, and the height was measured as 2.7 μm from the bottom to the lowest part of the growing surface. The high current density used in the second step (50 mA/cm^2) promoted Cu deposition on the side wall of the concave growing surface. The deposited Cu on the side wall blocked the deep concave structure, hindering the bottom-up growth, and finally voids were formed. During the second step, Cu deposition under the mass transfer limited condition also contributed to the defect formation. When 15 mA/cm^2 was applied for 150 s, the position of the deposited height prior to the second step (Fig. 3.12a) was measured as 12.7 μm from the bottom, similar to the void position formed after applying the second step current (Fig. 3.14b). In contrast, the bottom-up filling progressed sufficiently when the first step current density of 15 mA/cm^2 was applied for 200 s, and void-free filling continued in the second step at 50 mA/cm^2. The short duration of the first step reduced the total filling time. However, since the complete formation of growing surface in the first step was required for the void-free filling, an optimized condition of the first step was required. By modulating the step condition, filling time was further decreased by 35 s as compared to Fig. 3.13b.

Fig. 3.15 shows the filling profile based on the deposition time of the second step

after applying 15 mA/cm^2 for 200 s as the first step. The application of the second step current for 30 s created a leveled Cu surface (Fig. 3.15b) from the concave surface developed during the first step (Fig. 3.15a). The leveled surface then continuously propagated toward the trench opening without forming voids. When 50 mA/cm^2 was applied, the potential was measured as -440 mV (vs. Ag/AgCl, not shown here), which might be sufficiently negative to disrupt the inhibiting layers. However, the inhibiting layer formed on the top and the side wall near the top was not disrupted by the high current, but rather, suppressed Cu deposition almost perfectly. It was speculated that the current for Cu reduction was concentrated only on the growing interface, where the inhibitor coverage was low without severely detaching the inhibitors adsorbed onto the top and side walls.

In summary, the step current comprising of a first step of 15 mA/cm^2 to develop void-free growth followed by a second higher step current was applied to reduce the filling time. By modulating the deposition condition, filling time decreased by ~47% with the application of 15 mA/cm^2 (200 s) → 50 mA/cm^2 (120 s) compared to the galvanostatic filling time of 600 s. In conclusion, a first step lasting of 200 s was required to sufficiently establish the growing surface, enabling the void-free filling of trenches during the second step.

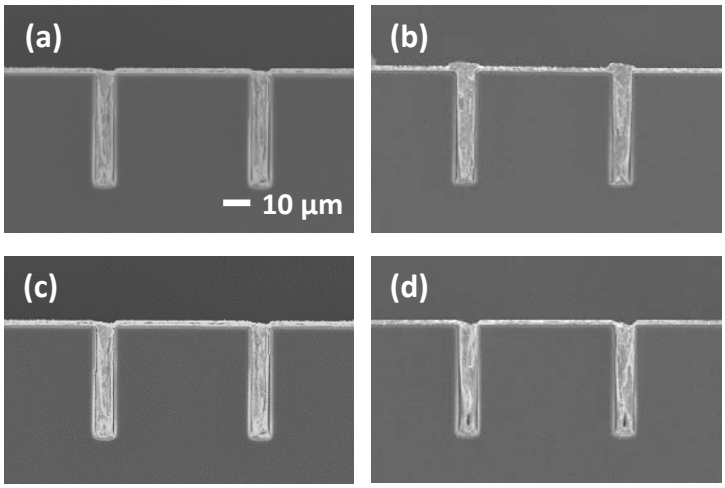

Fig. 3.11. Cross-section images of trenches galvanostatically filled by applying (a) 10 mA/cm^2 for 900 s, (b) 12.5 mA/cm^2 for 720 s, (c) 15 mA/cm^2 for 600 s, and (d) 17.5 mA/cm^2 for 514 s, under 900 rpm of the rotating speed. The filling was performed in the electrolyte containing 10 μM SPS, 50 μM PEG/PPG, and 50 μM Lev(1).

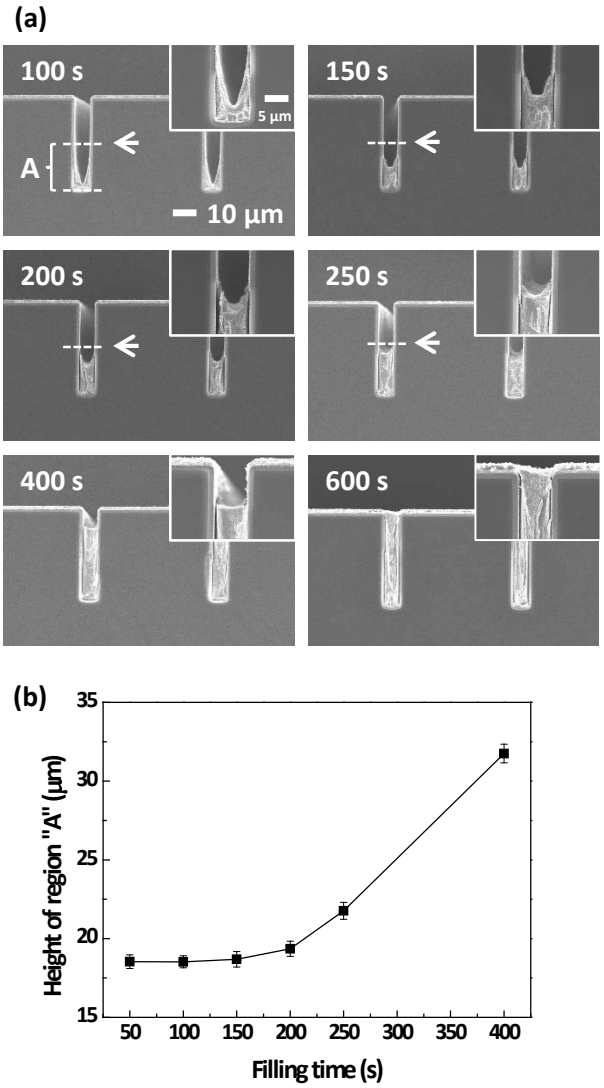

Fig. 3.12. (a) Cross-section images of filling profiles and (b) the highest position of deposited Cu on the side wall (marked as “A” and white arrows in Fig. 3.12a) according to the filling time. A constant current density of 15 mA/cm^2 was applied for 600 s under 900 rpm of the rotating speed with the addition of 10 μM SPS, 50 μM PEG/PPG, and 50 μM Lev(1).

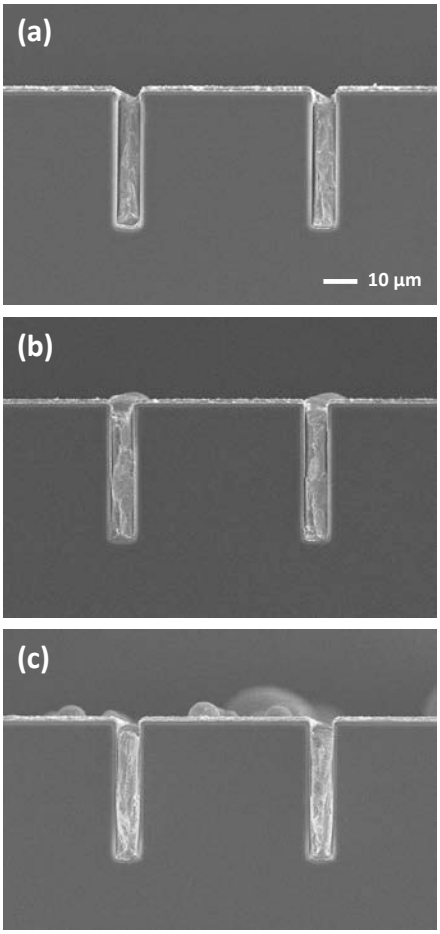

Fig. 3.13. Cross-section images of trenches filled by applying step current. 15 mA/cm^2 was applied in the first step for 250 s, and then (a) 30 mA/cm^2 for 175 s, (b) 50 mA/cm^2 for 105 s, and (c)70 mA/cm^2 for 75 s was applied in the second step. The total filling time of each figure is 425 s, 355 s, and 325 s, respectively. The filling was performed in the electrolyte containing 10 μM SPS, 50 μM PEG/PPG, and 50 μM Lev(1).

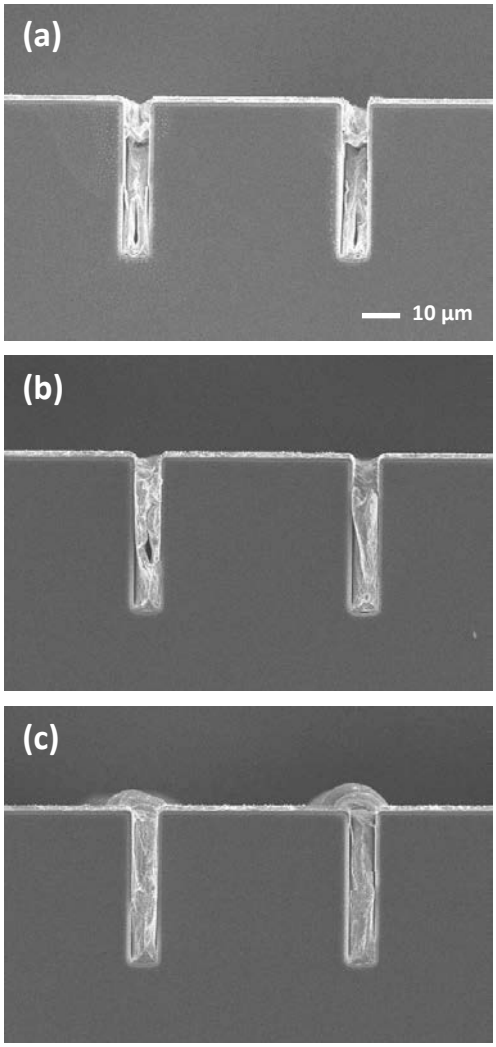

Fig. 3.14. Cross-section images of trenches filled by applying step current of (a) 15 mA/cm^2 (100 s) → 50 mA/cm^2 (150 s), (b) 15 mA/cm^2 (150 s) → 50 mA/cm^2 (135 s), and (c) 15 mA/cm^2 (200 s) → 50 mA/cm^2 (120 s). The total filling time of each figure is 250 s, 285 s, and 320 s, respectively. The filling was performed in the electrolyte containing 10 μM SPS, 50 μM PEG/PPG, and 50 μM Lev(1).

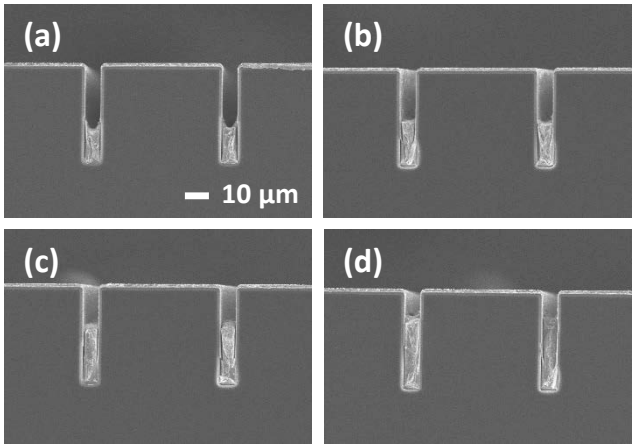

Fig. 3.15. Cross-section images of filling profiles by applying 15 mA/cm^2 for 200 s in the first step, followed by applying the second step current of 50 mA/cm^2 for (a) 0 s, (b) 30 s, (c) 60 s, and (d) 90 s. The filling was performed in the electrolyte containing 10 μM SPS, 50 μM PEG/PPG, and 50 μM Lev(1).

3.1.3. Effect of various levelers

Along with the change in deposition mode as discussed in Chapter 3.1.2, modification of the additive structure also affects the filling results. Various kinds of iodide-based levelers listed in Table 2.1 are suggested and tested to compare the effect of molecular structures on the Cu electrodeposition. The four levelers commonly contain two quaternary ammonium ions with iodide ions. The molecular structure is modified by changing the functional groups from hydroxyl to ester group, from methyl to allyl group, or by elongating the chain length, as described in the Experimental Chapter. Trench filling was performed in the three-additive composition containing 10 μM of SPS, 50 μM of PEG/PPG, and 50 μM of a leveler among Lev(1), Lev(2), Lev(3), and Lev(4). The cross-section images in Fig. 3.16 show the void-free filling results irrespective of the leveler.

LSV or Cu film deposition was performed in the three-additive composition to more clearly distinguish the effect of each leveler as shown in Fig. 3.17. Unfortunately, quite similar voltammograms were obtained in the given kinds of the levelers. The levelers had convection-dependent characteristic in common, with the similar synergetic inhibition when combined with PEG/PPG. It is reasonable to consider that all the four

levelers allow void-free filling based on the same mechanism discussed in Chapter 3.1.1.

Cu film was deposited in the three-additive system under 0 rpm, with diluted concentrations of PEG/PPG and the levelers in order to replicate the deposition condition at the bottom of the TSV.[89] As shown in Fig. 3.18, the addition of SPS, PEG/PPG and one of the levelers enabled the deposition of a flat Cu film compared to that of additive-free. However, dramatic change in the surface morphology was not observed. The properties of the deposited Cu films were analyzed by XRD and 4-point probe. The adsorbed additives retard the surface diffusion of Cu adatoms, thereby suppressing the growth of (111) orientation as shown in Fig. 3.19.[90] The increase in the resistivity is also attributed to the adsorbed additives which block the growth of (111) grains, thereby increasing the grain boundary scattering of electrons.[91-93] Note that the levelers exhibit a very minor effect on Cu (111) intensity or resistivity, below 7% or 5% deviation, respectively (Fig. 3.19). It is hard to conclude that the functional groups of the levelers determine the properties of Cu films.

All the levelers contain two quaternary ammonium cations and two anionc iodide ions in common. It indicates that the cationic or anionic part dominantly determines the characteristic of the levelers in the given suggested structures, rather than the different

molecular structures does. As noted by K. Kondo et al.,[94] the influence of halogen ions on Cu bottom-up filling is important, however, few studies have dealt with the effects of Br^- or I^- on Cu electrodeposition and gap-filling. Therefore, levelers containing various halide ions were synthesized by changing the iodide ion in Lev(2) to chloride or bromide ion, as listed in Table 2.2. The levelers containing various halide ions are now noted as Lev(2)-X (X=Cl, Br, I)

LSVs conducted with the single addition of Lev(2)-X are depicted in Fig. 3.20, demonstrating that the levelers induced convection-dependent suppression with a magnitude in the order of Lev(2)-Cl < Lev(2)-Br < Lev(2)-I. This suggested that the halide ions adsorbed onto the Cu surface with the leveler, affecting the electrochemical behavior.

The voltammograms with the levelers in the presence of PEG/PPG and SPS are depicted in Fig. 3.21. Convection-dependent characteristics are observed regardless of counter anions. However, the suppression increases in the order of Lev(2)-Cl < Lev(2)-Br < Lev(2)-I. The suppression power is saturated under 300 rpm, showing similar voltammograms to that under 900 rpm. It signifies that the levelers can effectively suppress electrodeposition at the side wall near the opening of the trenches where weak fluidic motion is predicted. In Lev(2)-Br and Lev(2)-I, considerable suppression and

convection dependent adsorption are clearly confirmed in Figs. 3.21b and 3.21c. The reduction current before the breakdown of the suppressing layer is remarkably decreased as compared to the case of Lev(2)-Cl. These results suggest that Br^- and I^- interacted with the suppressor, the organic part of the leveler, or both, finally establishing a compact and strong suppressing layer on the Cu surface.

CV was conducted to clarify the displacement of the pre-adsorbed suppressing layer by SPS. Cyclic voltammograms according to the levelers and the rotating speed are shown in Fig. 3.22. It was obvious that the addition of the levelers with the different counter anions changed the hysteric behavior. The area of hysteresis could be used to compare the degree of accelerator adsorption. The normalized values of the hysteresis areas to the area obtained without levelers, were 0.77, 0.85, and 0.18 under 0 rpm, and 0.66, 0.42, and 0.13 under 900 rpm for Lev(2)-Cl, Lev(2)-Br, and Lev(2)-I, respectively. Comparing the results without levelers and with Lev(2)-Cl, it was found that the organic part of the leveler reduced the adsorption of SPS. Previously, it was reported that polyethylene imine (PEI) reduced the displacement between the suppressing layer and the accelerator, and this was due to the ion pairing between PEI and SPS on the electrode surface.[95] The molecular backbone of the levelers might reduce the effect of SPS in a similar manner as PEI. Br^- and I^- effectively retarded the

displacement of the pre-adsorbed suppressing layer by SPS. It was previously noted that PEG-Cu^{+}-Br was much stronger than PEG-Cu^{+}-Cl.[96] Br^{-} and I^{-} seemed to form robust suppressing layers with PEG/PPG, interrupting the SPS adsorption. I^{-} even assisted in the rapid recovery of the suppressing layer during the backward scan. The displacement of SPS initially took place (-250 mV ~ -160 mV for 0 rpm, -250 mV ~ -200 mV for 900 rpm, in backward scan) followed by the readsorption of the suppressing layer. In summary, the counter ions and levelers hindered the adsorption of SPS, and the overall tendency was Lev(2)-Cl < Lev(2)-Br < Lev(2)-I.

The combination of PEG/PPG, SPS, and the levelers was applied to the filling of TSV-scaled trenches. The filling profiles are presented in Figs. 3.23. The combination of PEG/PPG and SPS without a leveler resulted in almost subconformal deposition of Cu. Note that Cu deposition was also concentrated at the bottom corner of the trenches as discussed in Fig. 3.7. With Lev(2)-Cl, conformal profiles with slightly reduced Cu deposition at the outside of the trenches compared to that of additive-free were observed. The overhang of Cu at the top corners of the trenches was diminished with Lev(2)-Cl compared to the results without the leveler.

The gap-filling profiles obtained with Lev(2)-Br are shown in Fig. 3.23c. The thickness of Cu outside the trenches was obviously decreased, and a V-shaped

deposition profile was observed. This was due to the strong suppression at the top surface and enhanced convection dependent behavior of the leveler with Br^-, which was consistent with the electrochemical results observed in Fig. 3.21b. Fig. 3.23d shows the gap-filling profiles obtained with the addition of Lev(2)-I. Successful bottom-up filling was confirmed in 9 μm-width trenches. Cu deposition was perfectly inhibited at the top surface of the features, resulted from the strong suppression under 900 rpm and effective retardation of the SPS adsorption observed in the voltammograms. The additional effects of I^-, that is, the increase in the suppression at the top surface and the reduction of SPS adsorption, definitely improved the bottom-up filling.

In summary, four kinds of levelers that commonly contained two quaternary ammonium cations and two iodide ion were tested. The results of filling, electrochemical analysis, and film properties were not dominantly affected by the levelers in spite of the change in the molecular structures. To examine the effect of halide ion, Lev(2) with different counter anions, Cl^-, Br^-, and I^-, were synthesized. The convection-dependent adsorption of Lev(2) and the effects of counter anions were investigated by electrochemical analyses. It was concluded that the characteristic of convection-dependent adsorption increased in the order of Lev(2)-I > Lev(2)-Br >

Lev(2)-Cl. The addition of Lev(2)-I only enabled bottom-up filling by blocking Cu deposition outside the TSV-scaled trenches, which supported the dominant role of I^- as the leveler. The detailed effect of iodide ion on Cu electrodeposition will be discussed in the next Chapter.

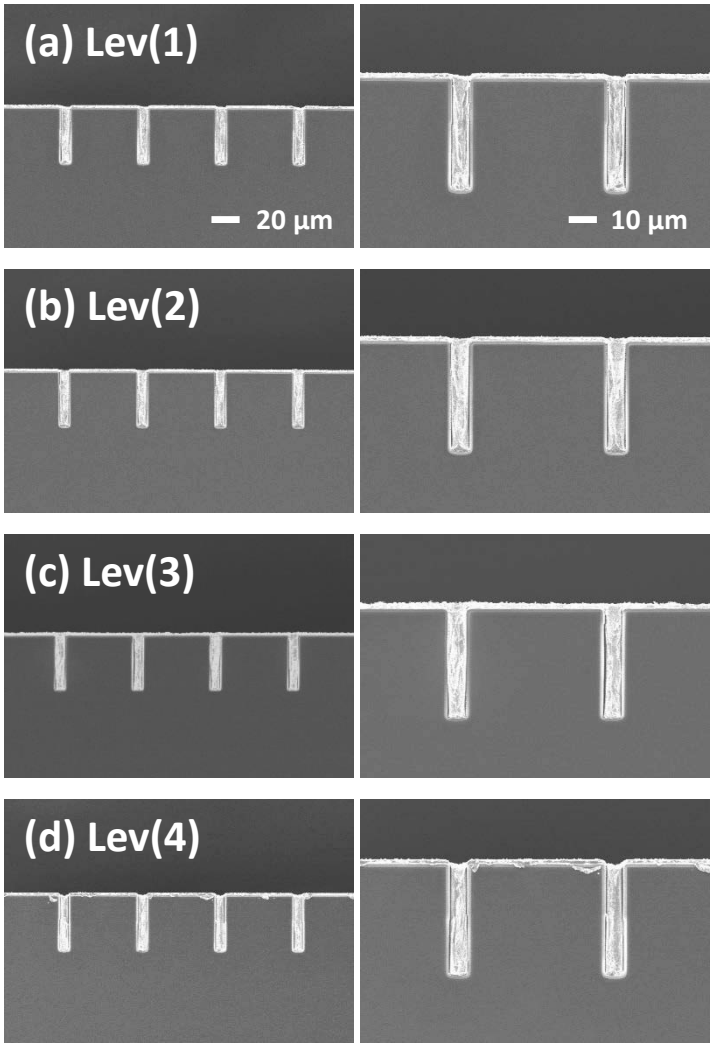

Fig. 3.16. Cross-section images of trenches filled with the addition of 10 μM SPS, 50 μM PEG/PPG, and 50 μM (a) Lev(1), (b) Lev(2), (c) Lev(3), and (d) Lev(4), at the current density of 15 mA/cm^2 applied for 600 s, at the rotating speed of 900 rpm.

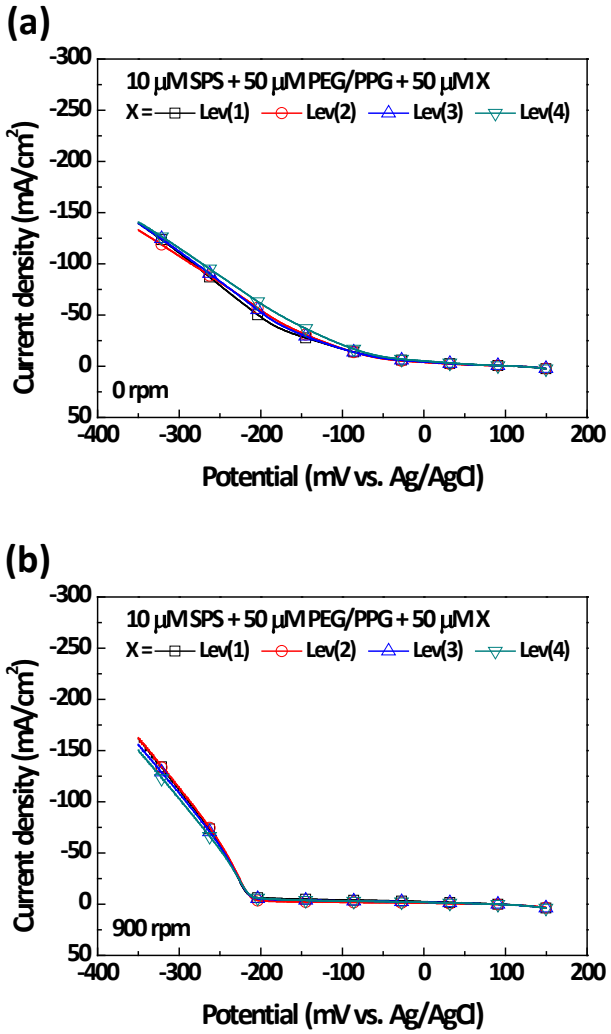

Fig. 3.17. Voltammograms obtained with the addition of 10 μM SPS, 50 μM PEG/PPG, and 50 μM Lev(1), Lev(2), Lev(3), or Lev(4). The potential was swept with a scan rate of 10 mV/s at the electrode rotating speed of (a) 0 rpm and (b) 900 rpm.

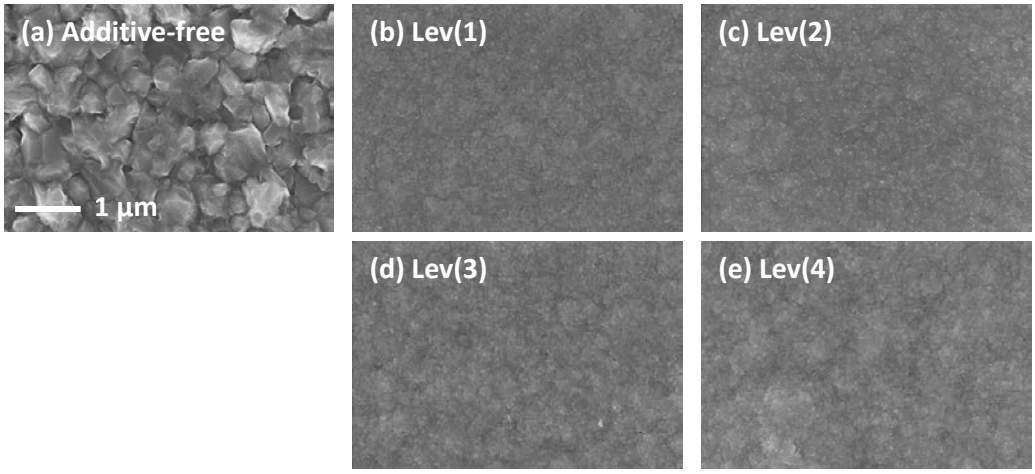

Fig. 3.18. (a) The surface morphology of deposited Cu on the blanket wafer without any additives. 10 μM of (b) Lev(1), (c) Lev(2), (d) Lev(3), and (e) Lev(4) was added with 10 μM of SPS and 10 μM of PEG/PPG. Cu film was deposited by applying 15 mA/cm^2 in convection-free condition.

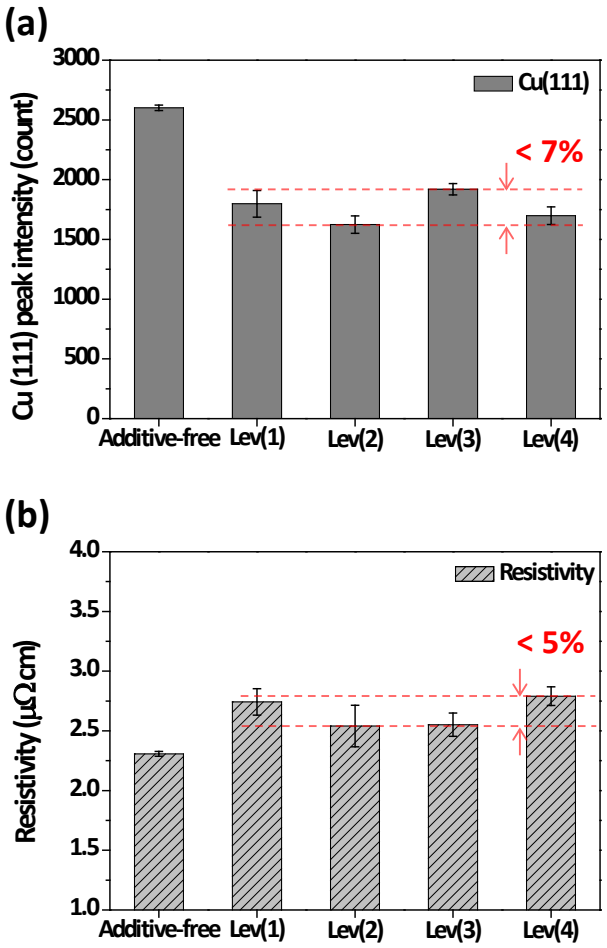

Fig. 3.19. (a) Cu (111) intensity measured and (b) resistivity of Cu films deposited in additive-free electrolyte or with the addition of 10 μM of SPS, 10 μM of PEG/PPG, and 10 μM of Lev(1) ~ Lev(4). Cu film was deposited by applying 15 mA/cm^2 in convection-free condition.

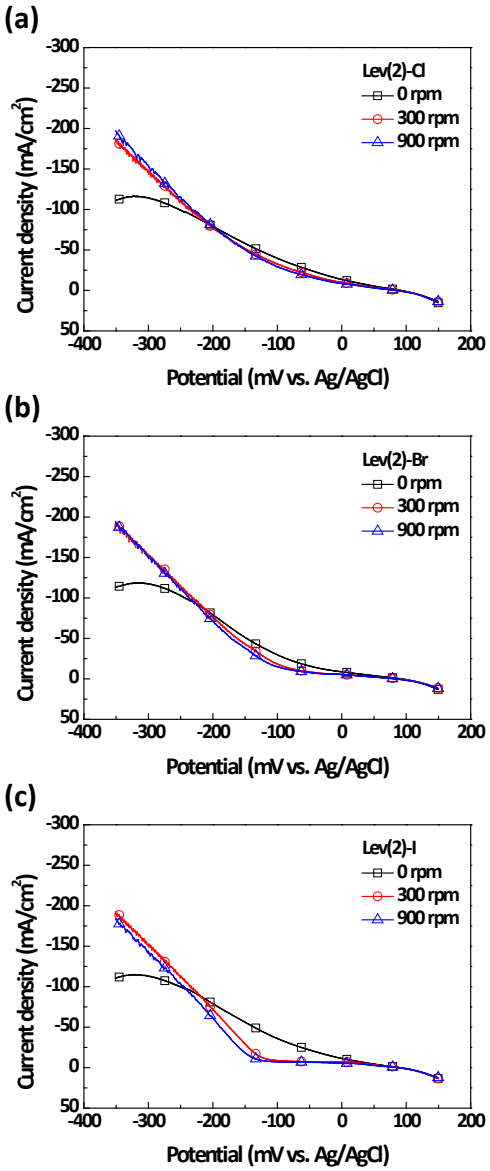

Fig. 3.20. Voltammograms obtained with the addition of 50 μM (a) Lev(2)-Cl, (b) Lev(2)-Br, and (c) Lev(2)-I. The potential was swept with a scan rate of 10 mV/s at the electrode rotating speed of 0, 300, and 900 rpm.

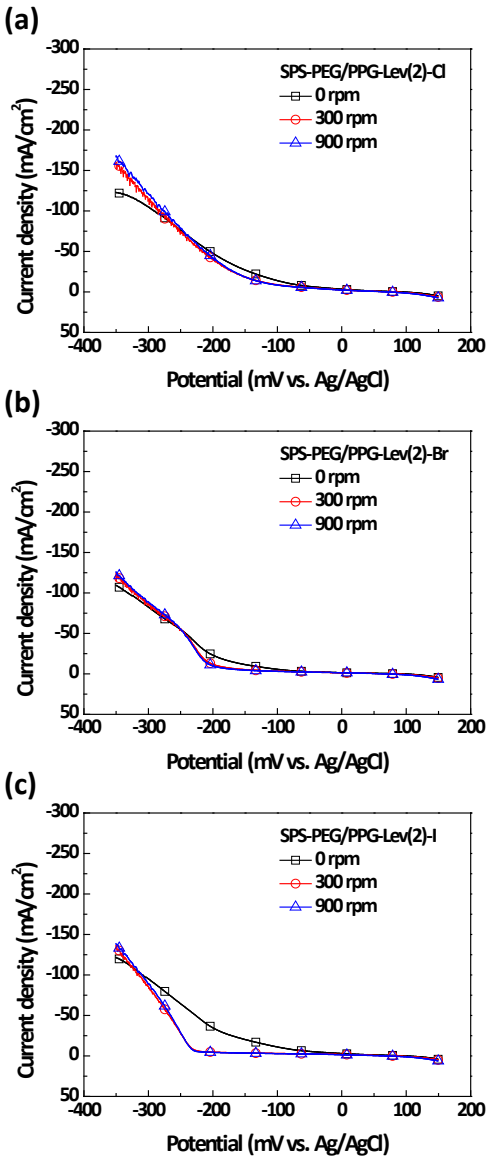

Fig. 3.21. Voltammograms obtained with the addition of 10 μM SPS, 50 μM PEG/PPG, and 50 μM (a) Lev(2)-Cl, (b) Lev(2)-Br, and (c) Lev(2)-I. The potential was swept with a scan rate of 10 mV/s at the electrode rotating speed of 0, 300, and 900 rpm.

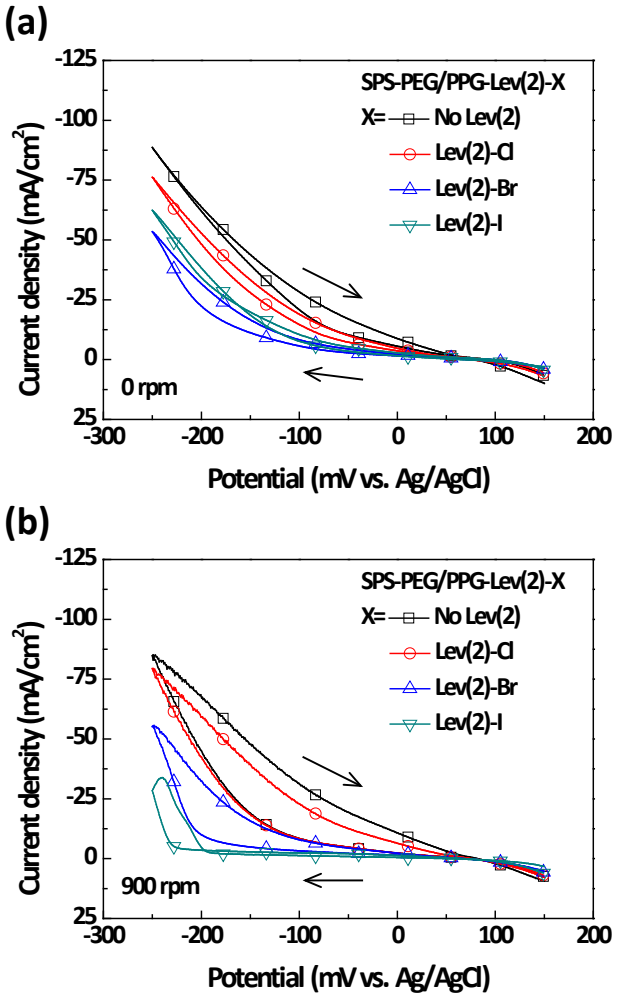

Fig. 3.22. Cyclic voltammograms obtained with the addition of 10 μM SPS, 50 μM PEG/PPG, and 50 μM Lev(2)-Cl, Lev(2)-Br, or Lev(2)-I. The potential was swept with a scan rate of 10 mV/s at the electrode rotating speed of (a) 0 and (b) 900 rpm.

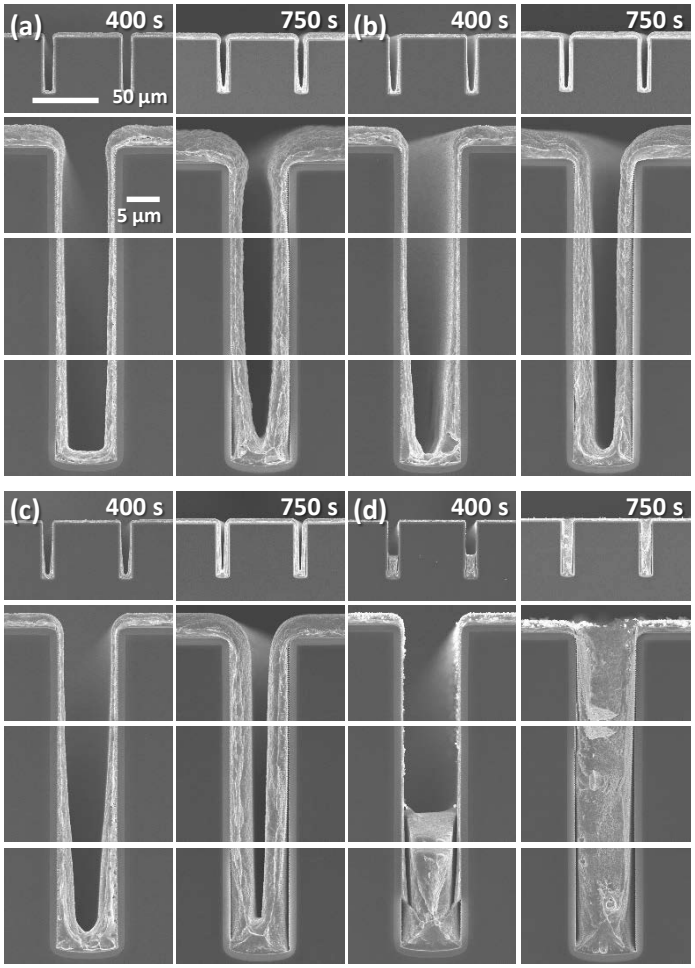

Fig. 3.23. Cross-section images of trenches filled (a) without any additives, or with the addition of 10 μM SPS, 50 μM PEG/PPG, and 50 μM (b) Lev(2)-Cl, (c) Lev(2)-Br, and (d) Lev(2)-I, at the current density of 15 mA/cm^2 under 900 rpm of the rotating speed.

3.1.4. Inorganic iodide-based leveler

It was revealed that the iodide ion in the synthesized leveler more dominantly determined the characteristic as the leveler than the organic part did. The study on the effect of iodide ion on the Cu electrodeposition is required. Unlikely to the role of Cl^- in Cu electrodeposition, the characteristics of I^- adsorption and its influences on Cu electrodeposition were not clearly investigated. Previously, the characteristics of the interaction between Cu and the halogen ions of Cl^- and I^- were reported.[97] The Cu-Cl species could easily move on the surface through Cl^- showing the ionic behavior when interacted with Cu.[97] In contrast, I^- gave its charge to Cu as in a covalent bond.[97] Therefore, the strength of the interaction was relatively strong compared to Cl^-, and Cu-I species were immobilized on the surface. Based on these characteristics, Cl^- acted as the corrosion promoter while I^- significantly reduced Cu corrosion.[97] Similar to the results of corrosion, it is possible that I^- suppresses the surface reaction of Cu reduction.

In this study, NaI was used as the source of I^-. LSV was performed by varying the concentration of I^- from 0 to 200 μM to investigate the effects of I^- on Cu electrodeposition. Fig. 3.24 depicts the voltammograms obtained at 0 and 900 rpm of Cu RDE rotating speed. The adsorption characteristic of I^- depended on the convection

strength similarly to that observed in the synthesized levelers discussed in Chapter 3.1. I^- showed negligible effect on Cu electrodeposition under 0 rpm in the given concentration range. However, Cu deposition was inhibited up to about -50 mV by adding I^- under 900 rpm. The change in I^- adsorption according to the rotating speed, i.e. mass transport of I^-, was clearly confirmed in Fig. 3.24c. The enhancement of I^- effect at 900 rpm originated from the increased mass transport of I^- leading to higher concentrations of I^- on the Cu surface.

Many studies have explained the interactions between polymeric suppressors and Cl^-: Cl^- provides the adsorption site for polyether suppressors.[98,99] However, few literatures dealt with the role of I^- with polymeric suppressor. LSVs were performed with various combinations of Cl^-, I^-, and PEG/PPG to clarify the interaction between I^- and PEG/PPG. Voltammograms obtained under 0 and 900 rpm are shown in Fig. 3.25. The suppression power increased in the order of Additive-free < PEG/PPG < PEG/PPG-I^- < PEG/PPG-Cl^- < PEG/PPG-Cl^--I^- at 0 rpm and 900 rpm. Interestingly, PEG/PPG added with I^- formed stronger blocking layer than that with the single addition of PEG/PPG. It signified that I^- obviously interacted with PEG/PPG, leading to an increase in the suppression. Also, the suppression layer formed with PEG/PPG-Cl^--I^- was broken at a more negative potential compared to PEG/PPG-Cl^-. I^- has a synergistic interaction with

Cl^-, thereby enhancing the adsorption of suppressor. The synergetic effect of I^- was observed with the synthesized levelers containing I^- (listed in Table 2.1).

The convection-dependent-adsorption characteristic of I^- was also observed in Fig. 3.25. The onset potentials of the combinations of PEG/PPG-Cl^- and PEG/PPG-Cl^--I^- showed potential difference below 100 mV under 0 rpm while over 200 mV under 900 rpm. This difference originated from the aforementioned change in the surface coverage of I^- according to the rotating speed. In addition, the desorption characteristics of PEG/PPG were changed by I^-. Regardless of rotating speed, PEG/PPG-Cl^- was gradually desorbed, i.e. a gradual increase in the reduction current while the steep increment of reduction current was observed with PEG/PPG-Cl^--I^- right after the onset potential.

The synergetic interaction between PEG/PPG and NaI is discussed in more detail by changing the concentrations of PEG/PPG or NaI as shown in Fig. 3.26. The concentration of I^- did not clearly affect the inhibition power, especially under 900 rpm. Under strong convection, 50 μM of I^- was enough to maximize the suppression effect of PEG/PPG. In the case of change in PEG/PPG concentrations, the suppression was almost saturated with 100 μM regardless of the rotating speed. From the voltammetric responses, it was concluded that I^- assisted and enhanced the suppression with

PEG/PPG.

As discussed previously, the displacement adsorption of SPS plays an important role in Cu electrodeposition and TSV filling. The influence I^- on SPS adsorption should be clarified. LSV was performed by adding various concentrations of NaI with the fixed concentration of 10 μM SPS as shown in Fig. 3.27. The adsorption and suppression of I^- were not observed under the stagnant condition (Fig. 3.27a); while the suppression was observed under 900 rpm (Fig. 3.27b), similar to the results in Fig. 3.24. The adsorption very slightly increased with a higher concentration of I^- only under 900 rpm. Interestingly, small reduction peaks were observed at potentials between 50 and -50 mV in the presence of I^- (as shown in the magnified images of Fig. 3.27c), which did not exist in the sole addition of NaI (Fig. 3.24b). The reduction peak was enlarged as the concentration of I^- increased. It may be related to the formation of a complex with regard to SPS and I^-, and Cu ions may also be involved in the formation of this complex.

CV was further performed to investigate the detailed effects of I^- on SPS adsorption as shown in Fig. 3.28. Twisted potential-current profiles were observed regardless of the concentration of I^-. At the initial stage (i), the aforementioned complex, which may consist of SPS, I^-, and Cu ions, was reduced. The suppressing I^- was desorbed at (ii)

because of a relatively negative electrode potential. During the backward sweep, (iii), the reduction current was higher than that in the forward scan, due to the considerable desorption of I^- and the following adsorption of SPS which slightly interrupted the reformation of suppressing layer. Finally, the suppressing layer was recovered at a positive potential, (iv). From CVs, the disturbance of suppressing layer reformation by SPS and the recovery rate for the suppressing layer could be conjectured from the hysteresis area (measured from cross point to switching potential, indicated as “Area” in Fig. 3.28a) and the cross point in twisted potential-current curves (marked as stars), respectively. The hysteresis area was normalized using the area obtained with 50 μM I^- (Fig. 3.28a), and the normalized values were 1, 0.46, and -0.05 for 50, 100, and 200 μM of I^-. The corresponding cross points were -14.6, -42.5, and -65.2 mV. These results implied that the use of more I^- reduced the effect of SPS and recovered the suppressing layer rapidly.

The effect of SPS concentration was also examined by CV with the addition of 50 μM of I^-, as exhibited in Fig. 3.29. An identical CV shape was observed, and the hysteresis area and cross point were measured based on the SPS concentration. The normalized hysteresis area was 1, 1.05, and 1.14, and the cross potential was -14.6, -10.2, and -3.12 mV for 10, 50, and 100 μM of SPS. More amount of SPS naturally occupied the

adsorption site on the Cu surface after the desorption of I^- at the negative potential and interrupted the formation of the suppressing layer.

Finally, the characteristics of full combination, i.e. PEG/PPG-SPS-I^-, were investigated using CV in the same manner as in Figs. 3.28 and 3.29. Fig. 3.30 shows the CV results according to the rotating speed and the concentration of I^- in the presence of 10 μM SPS and 50 μM PEG/PPG. Identical to the previous results, a strong suppression and twisted curves were observed with the addition of I^-. The shape of the curve during the forward scan with 200 μM I^- at 0 rpm was distorted, and it seemed that there was an additional reduction peak at around -180 mV. The color of the electrolyte was also slightly changed from blue to green with 200 μM I^-, therefore, a large amount of the complex may have been formed in the electrolyte due to the large amount of I^-.

The normalized hysteresis area and the cross potential in the three-additive system are plotted according to the concentration of I^- as shown in Fig. 3.31. As stated above, the higher normalized area suggested a larger disruption of the reformation of suppressing layer by SPS, and a more negative potential for the cross point meant fast recovery of the suppressing layer. That is, in the presence of PEG/PPG and SPS, I^- reduced the adsorption of SPS and assisted the reconstruction of the suppressing layer. These

phenomena were more remarkable with 900 rpm of rotating speed because the adsorption of I^- was increased through the enhanced mass transport of I^- under the strong convection.

The results of electrochemical analyses implies that I^- itself possibly works as the leveler. The adsorption of I^- depends on the convection strength, exhibiting stronger inhibition under forced convection. Furthermore, the suppressing power of PEG/PPG is enhanced with the addition of I^- through the synergetic interaction. Trench filling was performed by adding 10 μM SPS, 50 μM PEG/PPG, and 100 μM NaI instead of the synthesized levelers. The negligible Cu deposition on the top surface, as shown in Fig. 3.32, ensures the defect-free filling. The potential for the inorganic iodide to replace the conventionally used organic levelers is verified from the filling results.

The experiments conducted by adding other iodide compounds support the dominant effect of I^- as the leveler. LSV were performed by solely adding NaI, KI, NH_4I, or CH_3I under 0 and 900 rpm as shown in Figs 3.33a and 3.33b. No clear difference was observed under 0 rpm irrespective of the kind of iodide. The ionic compound of NaI, KI, and NH_4I inhibited Cu deposition under 900 rpm, while negligible effect of the covalent compound, CH_3I, was observed. The iodide compound except CH_3I enabled the void-free filling of TSV-scaled trenches in the presence of SPS and PEG/PPG by

applying the applied current density of 15 mA/cm^2. It is reasonable to consider that I^- ionized from the iodide compound dominantly determines the function as the leveler. CH_3I, which forms a covalent bond and does not provide I^- to the electrolyte, exhibits electrochemically negligible effect on Cu electrodeposition.

In summary, NaI exhibited the characteristics of the leveler which were observed with the synthesized levelers. Convection-dependent adsorption of I^- was observed by electrochemical analysis. I^- assisted the adsorption of suppressor, leading to the enhancement of suppression against Cu electrodeposition. Also, I^- reduced the effect of accelerator and the displacement behavior between pre-adsorbed suppressor and the accelerator. These influences of I^- was much significant under the strong convection of electrolyte. Based on the behavior of I^-, TSV-scaled trenches were completely filled with the combination of SPS, PEG/PPG, and NaI. Furthermore, other ionic compound containing iodide (i.e. KI and NH_4I) had similar electrochemical behavior to that of NaI, enabling the void-free filling. It is reasonable to consider that I^- dominantly determines the characteristic as the leveler, which is consistent with the minor effect of various iodide-based levelers (Figs. 3.17-3.19) on Cu electrodeposition although the molecular structures are changed.

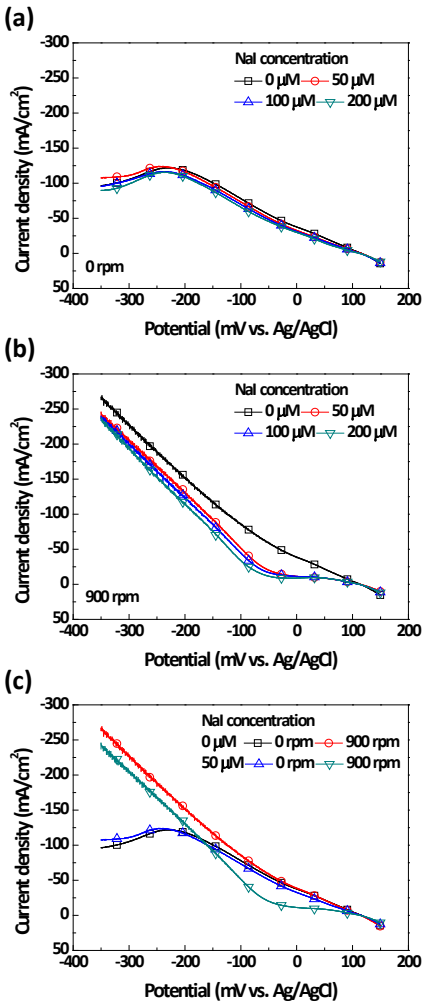

Fig. 3.24. Voltammograms obtained with the addition of 0 to 200 μM NaI under the rotating speed of (a) 0 rpm and (b) 900 rpm. (c) The replotted voltammogramss with 0 and 50 μM of NaI under 0 and 900 rpm to examine the convection-dependent adsorption of I^-.

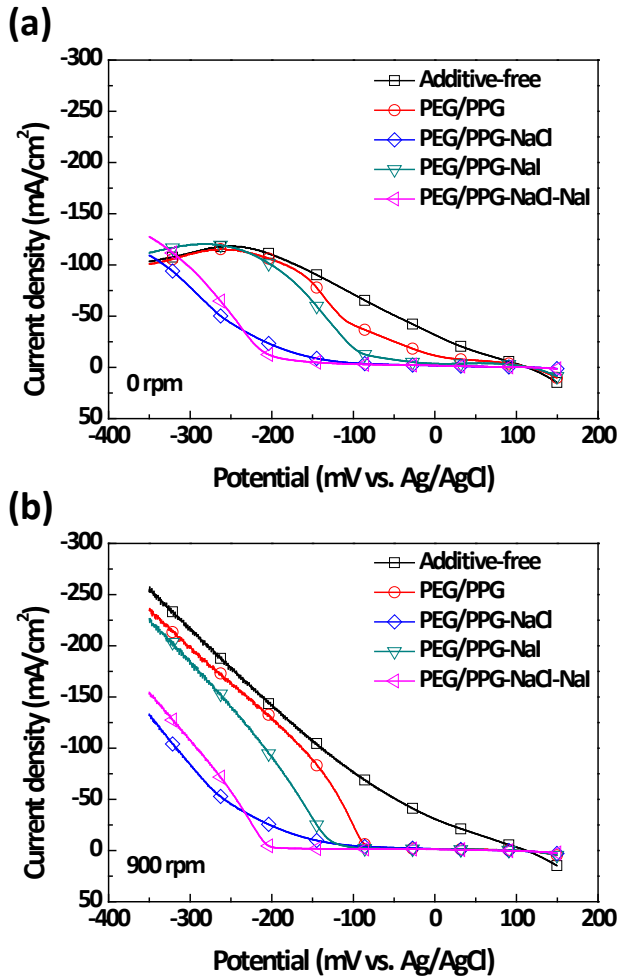

Fig. 3.25. Voltammograms obtained with various combinations of PEG/PPG, Cl^-, and I^- under (a) 0 rpm and (b) 900 rpm. The concentrations of PEG/PPG, Cl^-, and I^- were 50 μM, 1.4 mM and 50 μM, respectively.

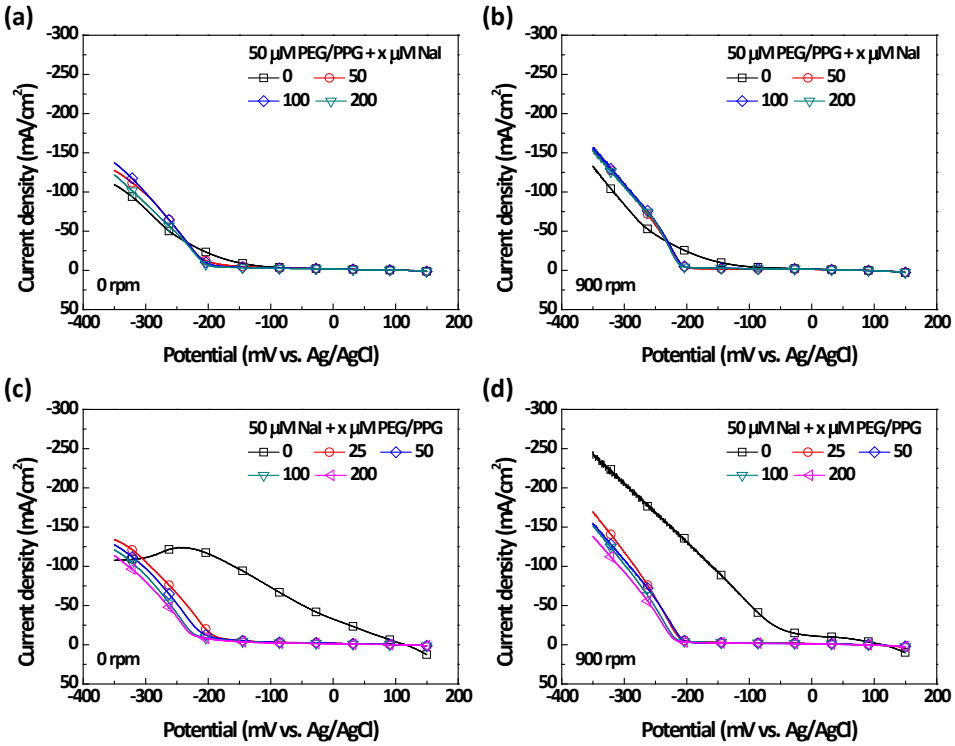

Fig. 3.26. Voltammograms obtained with the addition of 50 µM PEG/PPG and 0 to 200 µM NaI under (a) 0 rpm and (b) 900 rpm, as well as voltammograms obtained with the addition of 50 µM NaI and 0 to 200 µM PEG/PPG under (c) 0 rpm and (d) 900 rpm.

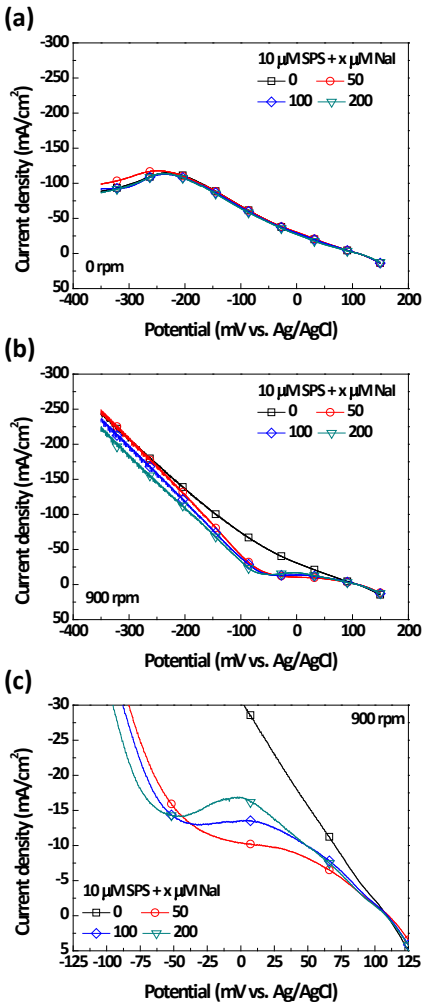

Fig. 3.27. Voltammograms obtained with the addition of 10 μM SPS and 0 to 200 μM NaI under (a) 0 rpm and (b) 900 rpm, and (c) the magnified voltammograms in (b).

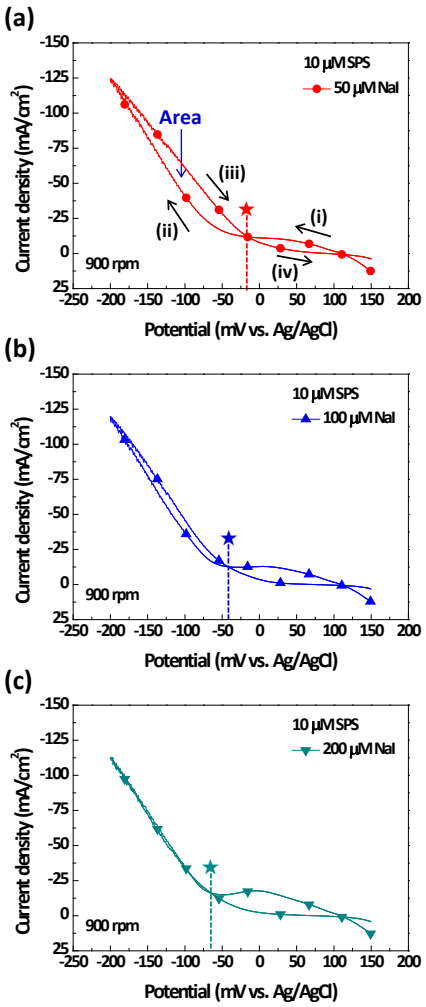

Fig. 3.28. Cyclic voltammograms obtained with the addition of (a) 50 μM, (b) 100 μM , and (c) 200 μM of NaI in the presence of 10 μM SPS under the rotating speed of 900 rpm.

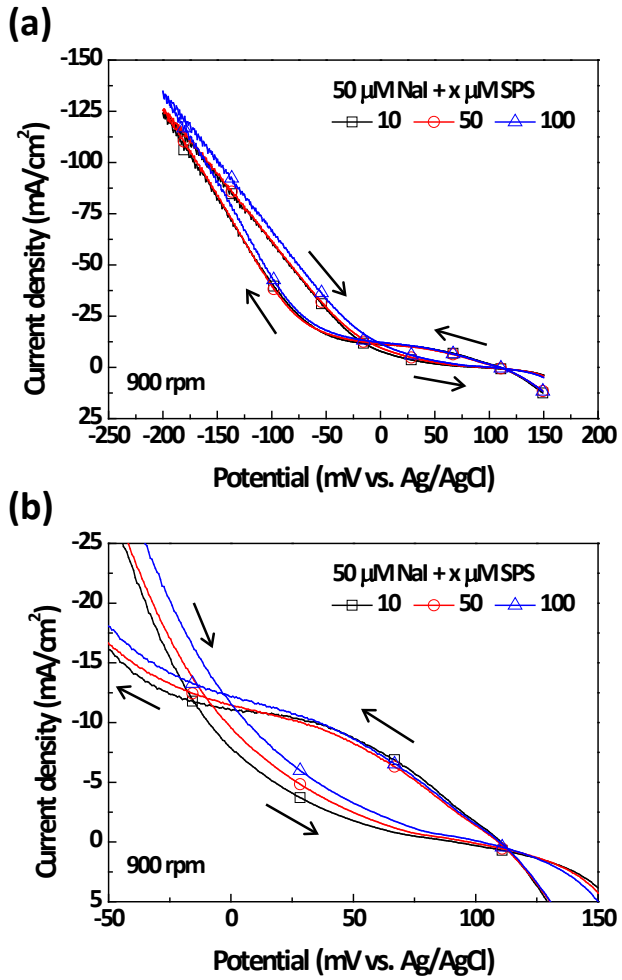

Fig. 3.29. (a) Cyclic voltammograms obtained with the addition of 10 μM to 100 μM of SPS in the presence of 50 μM NaI under the rotating speed of 900 rpm, and (b) the magnified voltammograms in (a).

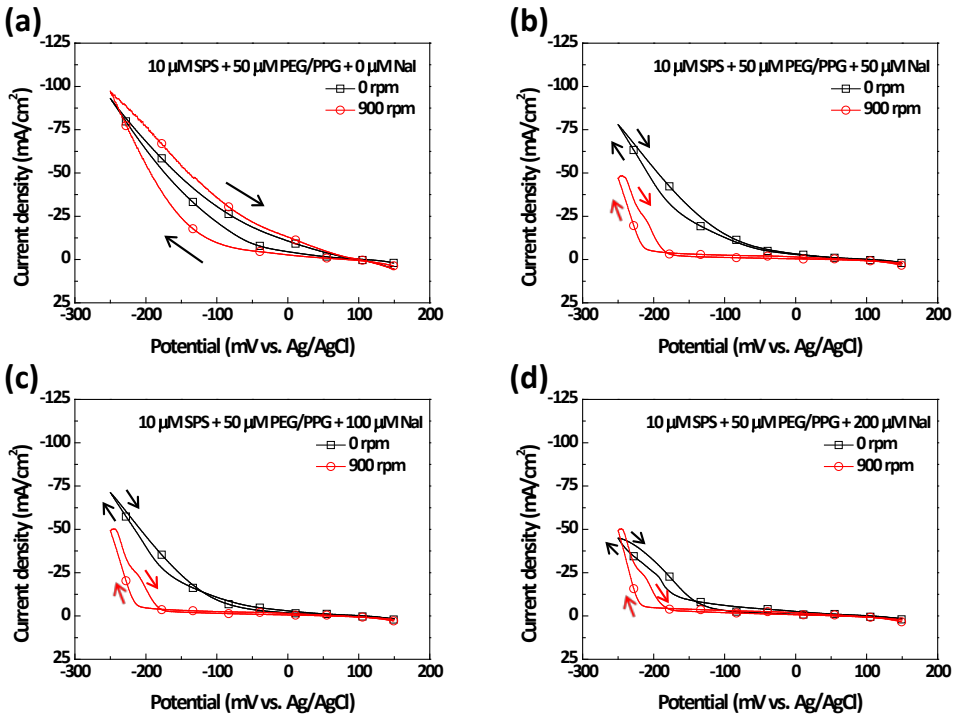

Fig. 3.30. (a) Cyclic voltammograms obtained with the addition of (a) 0 μM, (b) 50 μM, (c) 100 μM, and (d) 200 μM of NaI in the presence of 10 μM SPS and 50 μM PEG/PPG under the rotating speeds of 0 rpm and 900 rpm.

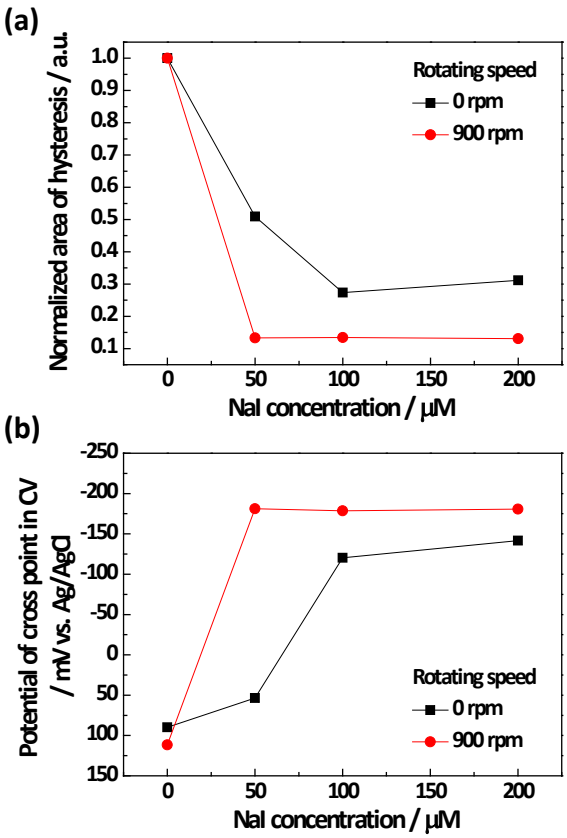

Fig. 3.31. (a) The normalized area for hysteresis and (b) the potential at the cross point according to the concentrations of NaI and the rotating speeds measured from cyclic voltammograms in Fig. 3.30.

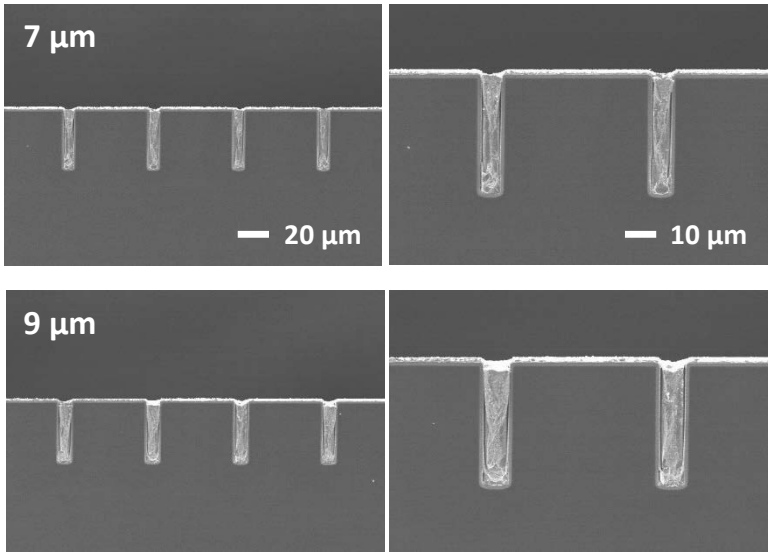

Fig. 3.32. Cross-section images of trenches filled with the addition of 10 μM SPS, 50 μM PEG/PPG, and 100 μM NaI at the current density of 15 mA/cm^2 applied for 600 s. Trenches of 7 μM and 9 μM in width were filled without voids.

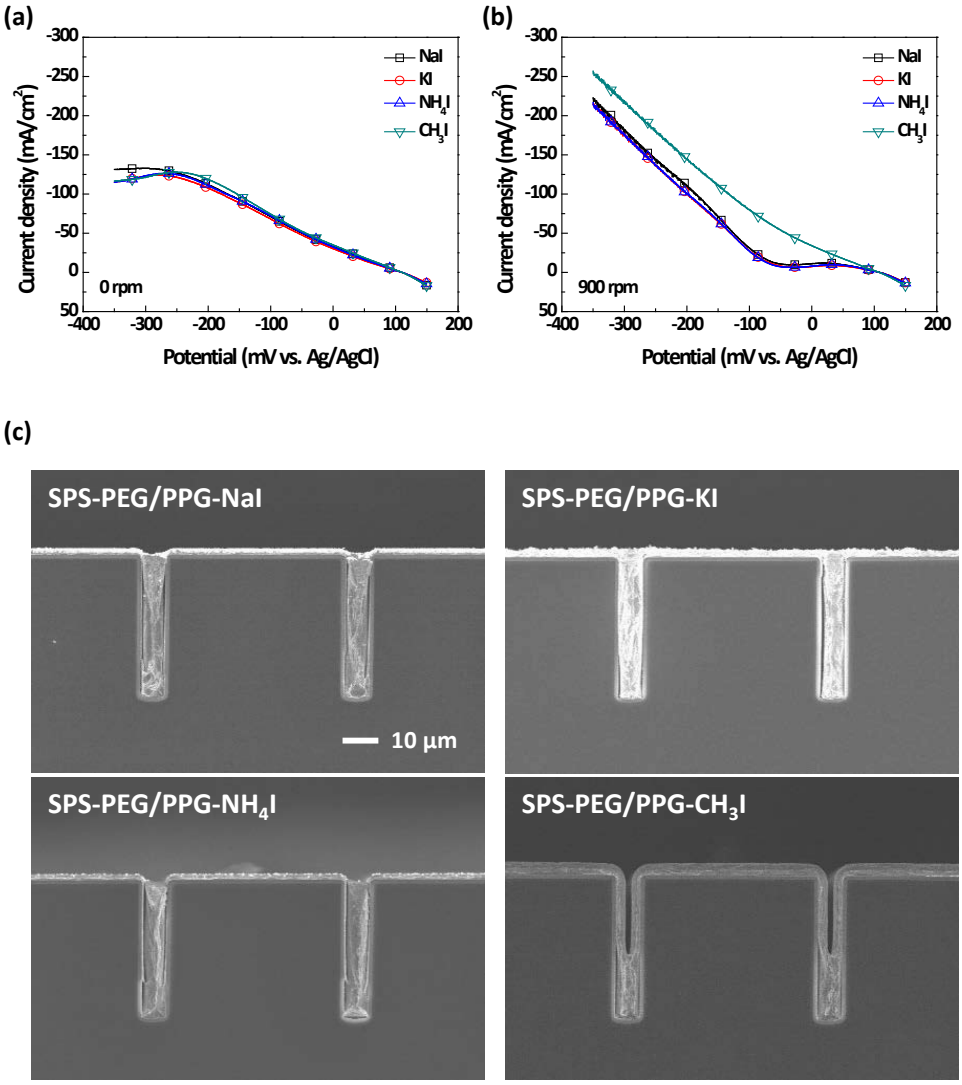

Fig. 3.33. Voltammograms obtained by adding 100 μM of NaI, KI, NH_4I, or CH_3I under (a) 0 rpm and (b) 900 rpm, and (c) cross-section images of trenches filled with the addition of 10 μM SPS, 50 μM PEG/PPG, and 100 μM of NaI, KI, NH_4I, and CH_3I at the current density of 15 mA/cm^2 applied for 600 s.

3.2. TSV filling in the four-additive composition

3.2.1. Electrochemical effect of TU

The reliable filling of TSV without voids must accompany a short filling time since the dimension of tens-of-micrometer in depth requires long filling time of the TSV as discussed in Chapter 3.1.2. Although increase in the applied current simply reduces the filling time, the high applied current kinetically promotes Cu deposition on the side walls of TSV and induces void-formation. In this Chapter, instead of TSV-scaled trenches used in Chapter 3.1, TSV of 5 μm in diameter and 60 μm in depth was filled galvanostatically at 1 or 2 mA/cm^2 of applied current density with the addition of SPS, PEG/PPG, and I^-, as shown in Fig. 3.34. The supply of Cu^{2+} inside the TSV is slower than that in the trenches due to the structural difference (TSV: hole vs. Trench: line). Compared to the current density of 15 mA/cm^2 for the TSV-scaled trench filling (Chapter 3.1), low current density of 1 mA/cm^2 is appropriate for the void-free filing of TSV (Chapter 3.2). At the applied current density of 1 mA/cm^2, void-free deposition of Cu occurred within 2200 s with the strongly blocked top surface through the adsorbed I^- and PEG/PPG. However, Cu was deposited on the side walls at the applied current

density of 2 mA/cm^2, before the bottom-up growth of the growing interface, resulting in the filling failure. The high applied current initiates Cu deposition on the side walls adjacent to the bottom where the surface coverage of suppressor and leveler are low. In this Chapter, a new combination of additives that enables the decrease in the galvanostatic filling time by enhancing the inhibition strength on the side walls is introduced.

TU is known to form a complex with ethylene oxide by the hydrogen bond between -NH_2 of the TU and -OH of the ethylene oxide.[100-102] LSV was performed with the addition of TU and PEG/PPG to examine the effect of TU on the suppression. As shown in Fig. 3.35, potential was swept under 0 and 900 rpm with the addition of 50 μM of PEG/PPG and various concentrations of TU. TU of low concentrations (10 to 50 μM) slightly increases the inhibition at 0 rpm, while 100 μM of TU rather weakens the inhibition. The bifunctional effect of TU according to the concentrations is more clearly observed at 900 rpm. In contrast to the strengthened inhibition with 10 and 25 μM of TU, the voltammetric current increases with TU of concentrations higher than 50 μM under 900 rpm. A significant depolarization occurs by adding extremely high concentrations of 500 μM TU with PEG/PPG, as shown in Fig. 3.35c, It results in the similar voltammogram to that of solely added 500 μM TU. Two adsorption pathways

of TU are considered; (1) TU with low surface coverage (with low concentrations and no convection) forms the complex with PEG/PPG, thereby stabilizing the adsorption of PEG/PPG. It is consistent with the enhanced inhibition demonstrated in the voltammetric responses with low concentrations of TU under the stationary condition. (2) TU with high surface coverage (with high concentrations and strong convection) gradually displaces the adsorbed PEG/PPG, occupying the adsorption sites of the Cu surface instead of increasing the adsorption strength of PEG/PPG. The weakened inhibition with high concentrations of TU is attributed to the dominant adsorption of TU which disrupts the suppressing layer.

Cyclic voltammogram shown in Fig. 3.36 more clearly demonstrates the bifunctional effect of TU according to the concentrations. CV was conducted at the rotating speed of 0 rpm with the same concentrations of additives used in Fig. 3.35. As shown in Fig. 3.36, the current densities in the return sweep decreased with the addition of 10 and 25 μM of TU at 0 rpm, due to the adsorbed TU which enhanced the adsorption strength of PEG/PPG. However, the current in the return sweep increased with the addition of 50 and 100 μM of TU within the potential range of about -150 mV ~ -50 mV. High concentrations of TU are gradually adsorbed on the Cu surface by displacing the pre-adsorbed PEG/PPG. The displacement adsorption of TU resulted in the formation of

hysteresis in the voltammograms. The hysteresis area increased from 51.5 to 147.6 mC/cm^2 as the concentration of TU increased from 50 to 100 μM, which implied that higher concentrations of TU promoted the displacement rate. It is noteworthy that only TU added in appropriately low concentrations improves the inhibition strength with PEG/PPG.

It has been commonly discussed that the surface coverage of the polymeric suppressor gradually decreased from top to bottom of the TSV due to the order of magnitude lower diffusion coefficient compared to that of Cu^{2+} or accelerators. The effect of TU according to the concentrations of PEG/PPG was investigated by CV as shown in Fig. 3.37. The concentrations of PEG/PPG decreased as 50, 35, to 20 μM to replicate the decreasing surface coverage of PEG/PPG in the direction from top to bottom of TSV. The current densities in the return sweep decreased, without any hysteresis, with the addition of 10 μM TU. On the contrary, a clear hysteresis was observed by adding 100 μM TU irrespective of the concentrations of PEG/PPG. Low concentration of TU improves the adsorption of PEG/PPG, thereby increasing the suppressing power. As the concentrations of TU increased up to 100 μM, displacement of PEG/PPG by TU occurred as shown in the hysteresis in Fig. 3.37. The hysteresis area increased with the decrease in the concentrations of PEG/PPG: 147.6 mC/cm^2, 179.0 mC/cm^2, and 183.1

mC/cm^2 with 50 μM, 35 μM, and 20 μM of PEG/PPG, respectively. With the low concentrations of PEG/PPG, that is, on the side walls near the bottom of TSV, the adsorbed PEG/PPG was more obviously displaced by 100 μM of TU. It is reasonable to consider that the concentrations of TU should be added with low concentrations to improve the inhibition, since high concentrations of TU possibly deactivates the adsorbed PEG/PPG on the side walls, especially on the side walls adjacent to the bottom.

One fatal problem of TU is expected: the adsorbed PEG/PPG can be displaced by TU on the top surface where forced convection exists, which deteriorates the filling performance through the weakened inhibition near the top. To simulate the effect of TU on the top surface, LSV was performed by adding various concentrations of TU with 50 μM PEG/PPG, 400 μM NaI, and with or without 10 μM SPS at 900 rpm. As shown in Fig. 3.38a, the blocking power of suppressing layer was enhanced by adding high concentrations of TU with PEG/PPG and I^-. As discussed in Fig. 3.25, I^- interacted with PEG/PPG, leading to an increase in the suppression. The improved adsorption of PEG/PPG with I^- can resist to the displacement by TU at 900 rpm. Furthermore, the chronoamperometry results performed by adding two additives of NaI and TU (Fig. 3.39) shows that high concentrations of TU proportionally increase the inhibition

strength of I^-. The enhanced inhibition is more noticeably observed at 900 rpm due to the sufficiently supplied I^- and TU to the electrode. It is concluded that TU synergistically interacts with I^-. In the three-additive system of Fig. 3.38a, even high concentrations of TU cannot displace the PEG/PPG that is strongly adsorbed on the Cu surface in the presence of I^-. The complementary interaction of TU and I^- reduces the displacement effect, as well. Consequently, as shown in Fig. 3.38b of 4-additive system (SPS, PEG/PPG, I^-, and TU), the onset potential was shifted to negative direction with the concentrations of TU. It clearly demonstrates that, in the presence of I^-, displacement of PEG/PPG by TU does not occur on the top of the TSV (at 900 rpm and with the four additives, that is, Fig. 3.38b), with the well-maintained inhibition strength.

The interaction of TU and SPS-PEG/PPG was further investigated to predict the aspect of Cu deposition on the TSV side walls. The displacement of PEG/PPG by SPS at the bottom of TSV allows the formation of growing surface. However, if the displacement reaction also occurs on the side walls during the long filling, not only on the bottom surface, then it initiates Cu deposition on the side walls as well and deteriorates the filling performance by forming voids. Therefore, the displacement adsorption of SPS should selectively occur on or just near the bottom. CV was performed with the addition of 10 μM SPS, 50 μM PEG/PPG, and 10 to 100 μM TU to

investigate the effect of TU on the displacement adsorption of SPS (Fig. 3.40). The addition of PEG/PPG and SPS results in a conventional hysteresis as shown in Fig. 3.40a. The pre-adsorbed PEG/PPG is displaced by SPS during the sweep, showing higher current in the return sweep due to the promoted Cu deposition by SPS. The hysteresis area significantly decreases with the addition of 10 μM TU. The current in the return sweep becomes even lower than that in the negative-going sweep with the addition of 25 μM TU. Higher concentration of 100 μM TU induces a twisted voltammetric response. The hysteresis area, calculated by the charge differences between the return sweep and the forward sweep (Q_{return} - $Q_{forward}$), are measured as about 162 mC/cm^2 and 15 mC/cm^2 for the concentrations of TU as 0 μM and 100 μM, respectively. The low concentrations of TU as 10 μM and 25 μM reinforce the adsorption of PEG/PPG and significantly retards the displacement of PEG/PPG by SPS, consistent with the disappearing hysteresis in CV (Figs. 3.40b and c). With 100 μM of TU, current density increases in the return sweep just after the vertex potential of -250 mV, followed by making a cross point at about -150 mV. 100 μM of TU disrupts the adsorption of PEG/PPG, congruent with the results of Fig. 3.36, inducing increase in the current at the return sweep. Re-adsorption of PEG/PPG occurs in the positive return potential at which the adsorption strength of TU is low, making the cross point.

It is noteworthy that the low concentrations of TU as 10 or 25 μM enhances the adsorption of PEG/PPG, accompanying the suppressed displacement of PEG/PPG by SPS on the side walls. Along with the enhanced inhibition on the side walls, the improvement of inhibition by TU decreases on the bottom surface of TSV with the reduced surface coverage of PEG/PPG as discussed in Fig. 3.37. It is expected that the accumulation of SPS selectively occurs on the bottom surface while it is suppressed on the side walls, thereby enabling the bottom-up growth.

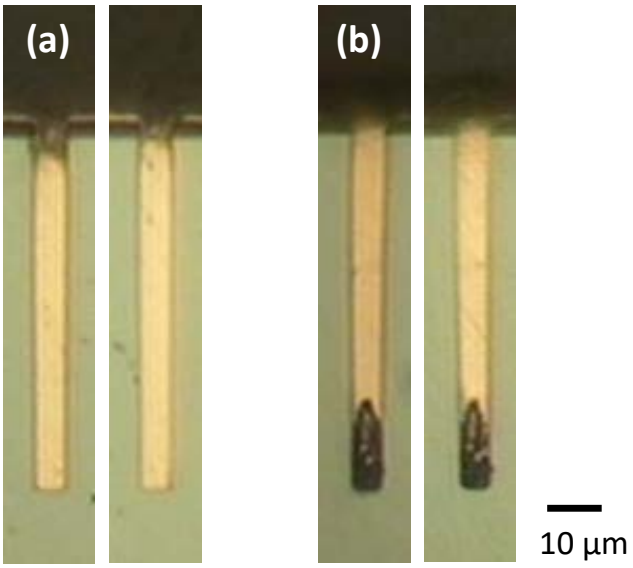

Fig. 3.34. Cross-section images of TSV filled by Cu with the addition of 10 μM SPS, 50 μM PEG/PPG, and 400 μM NaI at the current density of (a) 1 mA/cm^2 and (b) 2 mA/cm^2 applied for 2200 s and 1100 s, respectively. The filling was performed under the rotation of 900 rpm.

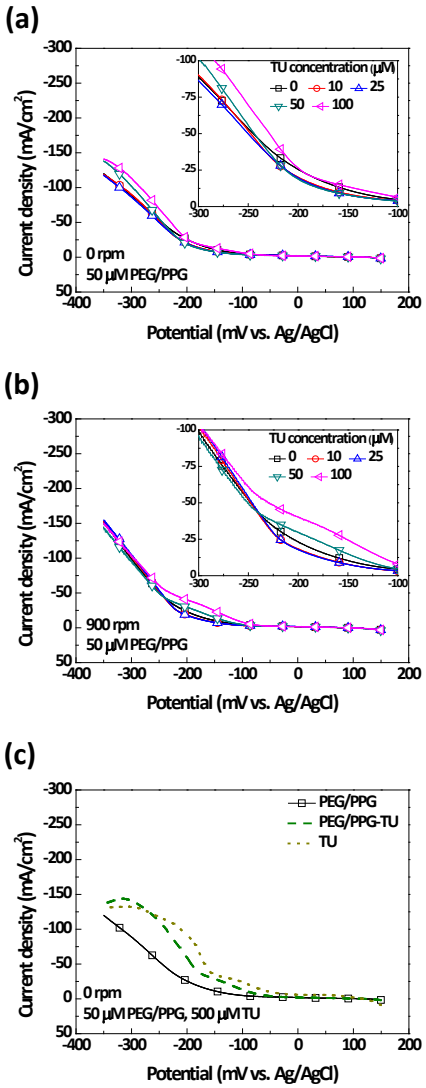

Fig. 3.35. Voltammograms obtained with the addition of 50 μM PEG/PPG and 0 to 100 μM TU under the rotation of (a) 0 rpm and (b) 900 rpm. (c) Voltammograms obtained by combining 50 μM PEG/PPG and 500 μM TU at 0 rpm.

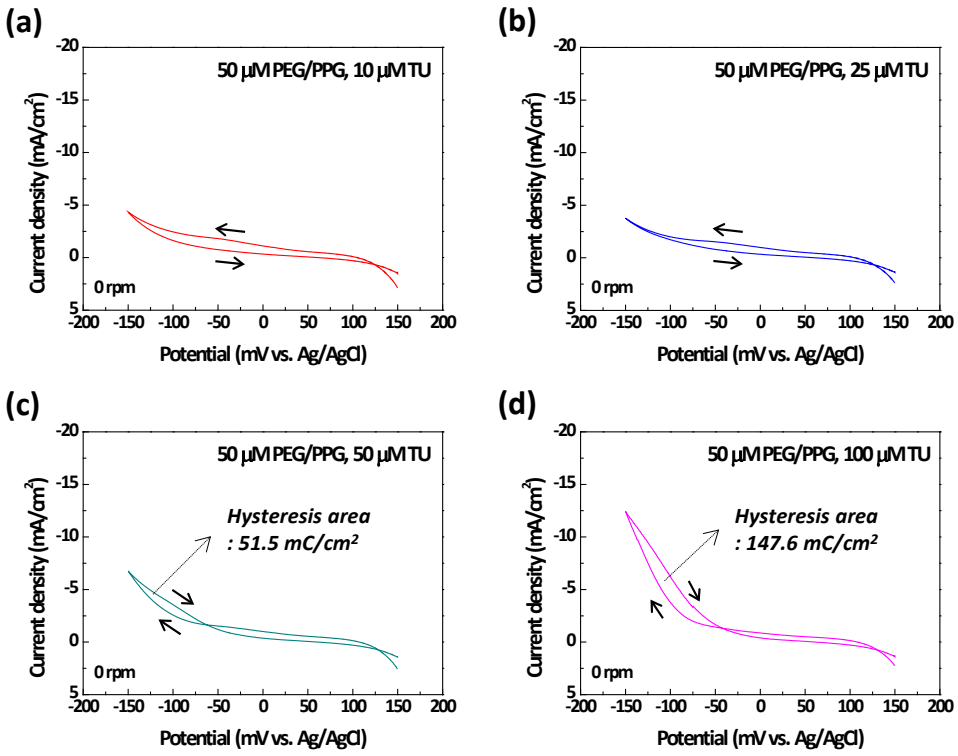

Fig. 3.36. Cyclic voltammograms obtained with the addition of 50 μM PEG/PPG and TU of (a) 10 μM, (b) 25 μM, (c) 50 μM and (d) 100 μM under the rotation of 0 rpm.

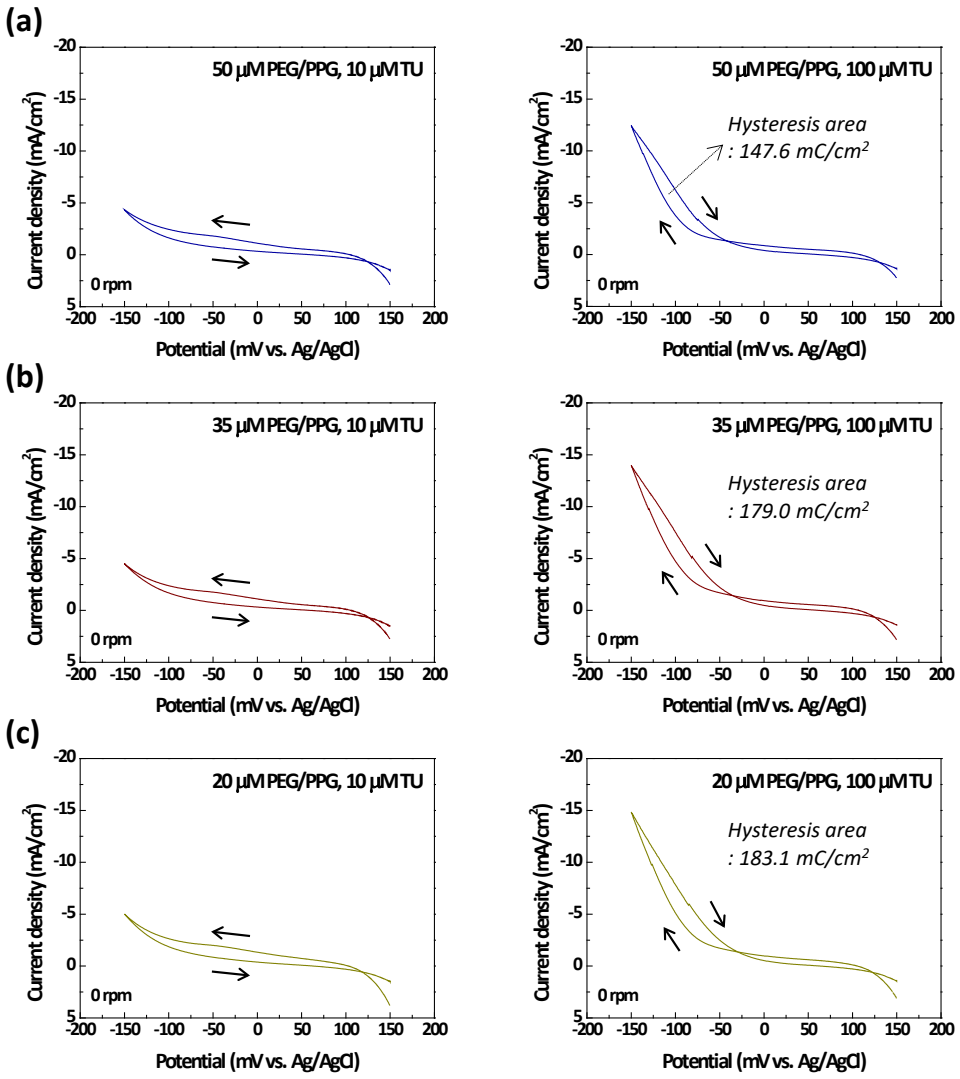

Fig. 3.37. Cyclic voltammograms obtained with the addition of 10 μM or 100 μM TU and PEG/PPG of (a) 50 μM, (b) 35 μM, and (c) 20 μM under the rotation of 0 rpm. The left and right figures were obtained with the addition of 10 μM TU and 100 μM TU, respectively.

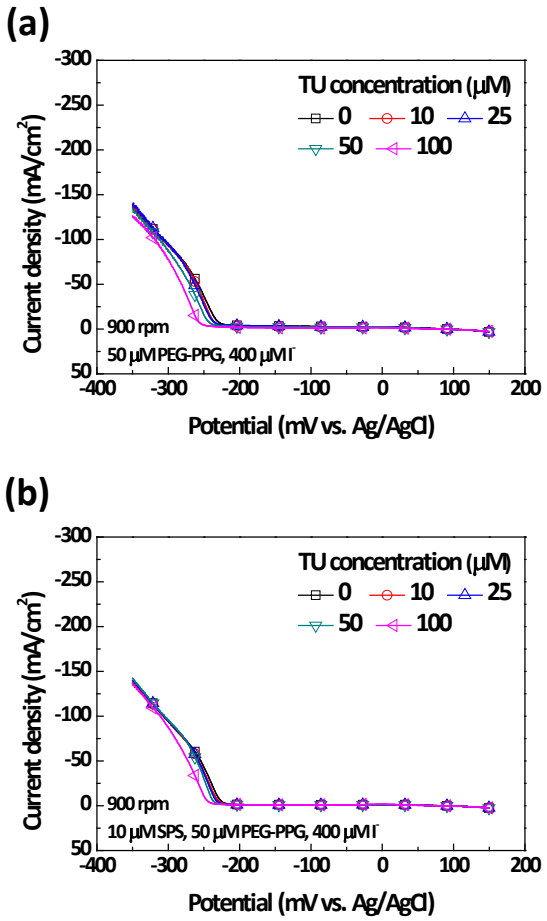

Fig. 3.38. Voltammograms obtained with the addition of 50 μM PEG/PPG, 400 μM NaI, and 0 to 100 μM TU (a) without SPS and (b) with 10 μM SPS under the rotation of 900 rpm.

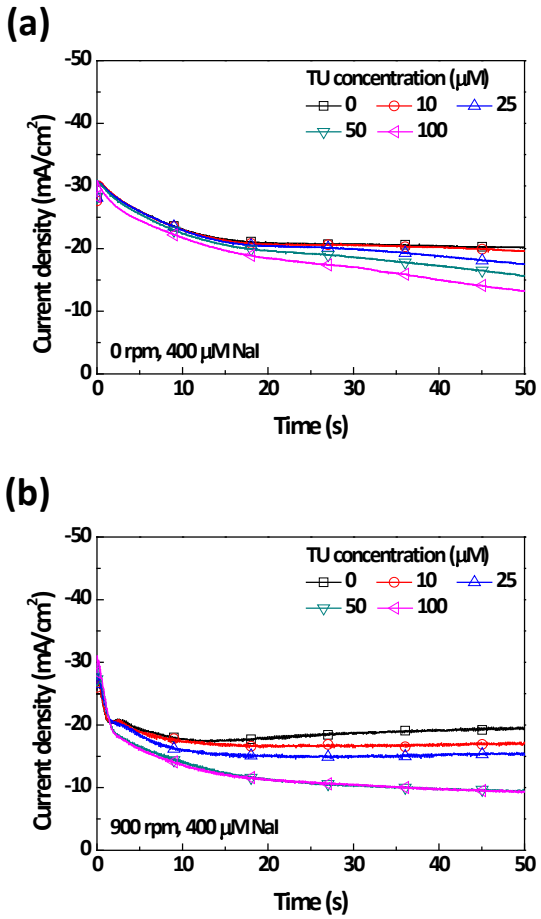

Fig. 3.39. Current profiles measured by applying -200 mV (vs. Ag/AgCl) for 50 s with the addition of 400 μM NaI and 0 to 100 μM TU under the rotation of (a) 0 rpm and (b) 900 rpm.

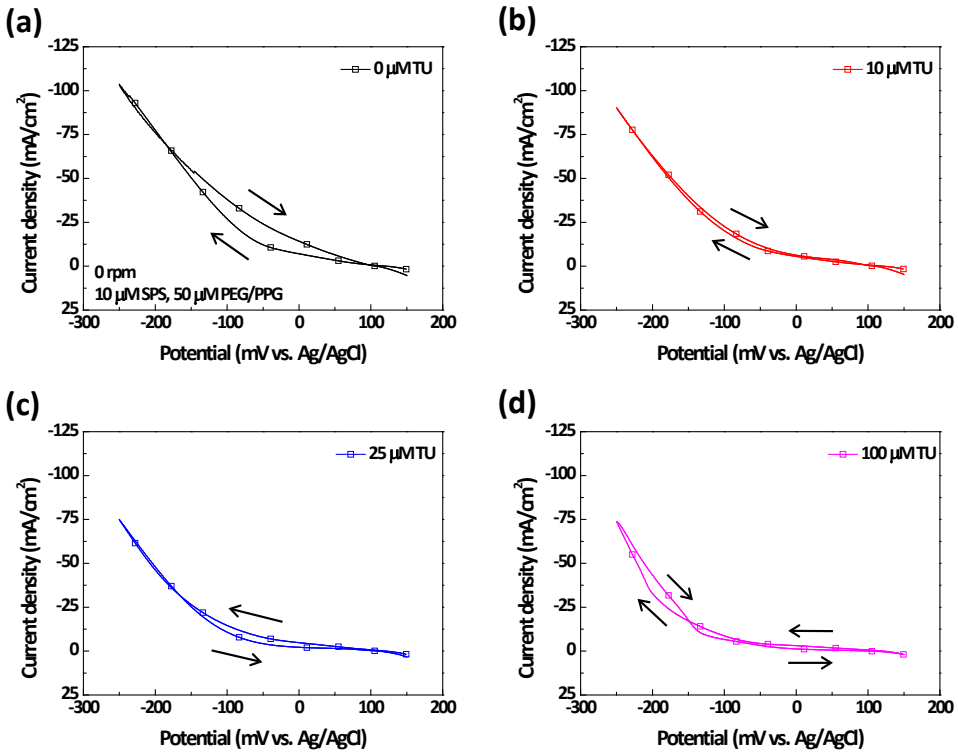

Fig. 3.40. Cyclic voltammograms obtained with the addition of 10 μM SPS, 50 μM PEG/PPG, and (a) 0 μM, (b) 10 μM, (c) 25 μM, and (d) 100 μM of TU under the rotating speeds of 0 rpm.

3.2.2. TSV filling with the addition of TU

TSV filling was performed by applying 2 mA/cm^2 of current density in the four-additive composition of SPS, PEG/PPG, I^-, and TU as shown in Fig. 3.41. On the contrary to the filling failure at 2 mA/cm^2 without TU (Fig. 3.34), the small addition of TU with 10 and 25 μM enables void-free filling at 2 mA/cm^2. Increasing the concentrations of TU to 50 and 100 μM deteriorates the filling performance. Low concentrations of TU stabilize the adsorption of PEG/PPG, enhancing the blocking power of the suppressor and also retarding the displacement of PEG/PPG by SPS on the side walls. It is considered that TU interrupts the displacement reaction only on the side walls, while SPS can be accumulated on the bottom of the TSV where the PEG/PPG is adsorbed with low surface coverage.[103,104] As a result, the filling time is reduced in half than that without TU, from 2200 s at 1 mA/cm^2 to 1100 s at 2 mA/cm^2. TU with the high concentration is dominantly adsorbed on the Cu surface and in doing so disrupts the PEG/PPG blocking layer. The weakened suppression causes the Cu deposition on the side walls and void formation as shown in Figs. 3.41c and 3.41d.

In summary, the effect of TU on the Cu electrodeposition was investigated in this Chapter. Bifunctional behavior of TU was observed: (1) low adsorption density of TU

enhanced the suppression of PEG/PPG, while (2) TU added with high concentration under forced convection disrupted the adsorption of PEG/PPG. The bifunctional effect of TU disappeared in the combination of TU and I^-. TU and I^- synergistically increased the inhibition as the concentrations of TU increased, especially at 900 rpm. Finally, low concentrations of TU impeded the displacement of PEG/PPG by SPS through the enhanced blocking layer of the suppressor in the presence of TU. Based on the electrochemical analysis, the filling performance was improved by adding 10 or 25 μM of TU to the three-additive system. In the three-additive composition without TU, Cu deposition was not blocked on the side walls at the applied current density of 2 mA/cm^2 due to the weak inhibition. However, in the four-additive composition containing TU, the blocking power of PEG/PPG was enhanced and displacement adsorption of SPS on the side walls was also retarded by TU. Cu deposition was efficiently inhibited on the side walls even at 2 mA/cm^2, which allowed the bottom-up growth. The filling time in the four-additive chemistry was reduced in half by adding TU compared to that of three-additive composition without TU.

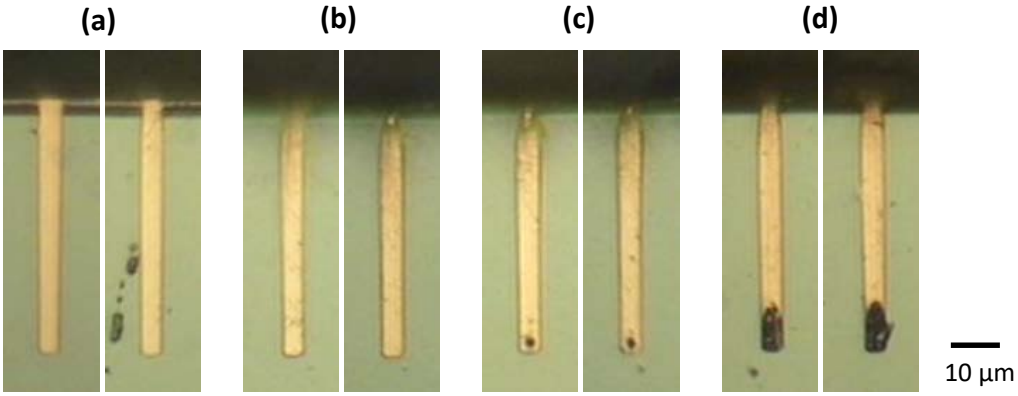

Fig. 3.41. Cross-section images of TSV filled by Cu with the addition of 10 μM SPS, 50 μM PEG/PPG, 400 μM NaI, and (a) 10 μM, (b) 25 μM, (c) 50 μM, and (d) 100 μM of TU at the current density of 2 mA/cm^2 applied for 1100 s.

CHAPTER IV

Conclusion

In this study, iodide-based levelers that enabled the void-free filling of TSV in the three- or four-additive composition were introduced with the filling mechanism examined based on the electrochemical analyses.

An organic leveler containing two quaternary ammonium ions and two iodide ions at the both ends of the structure was synthesized. The leveler exhibited convection-dependent adsorption characteristic and increased the suppressing power of PEG/PPG synergistically. TSV-scaled trench was filled, in the three-additive system containing the leveler, without any voids at an applied current density of 15 mA/cm^2. The synergetic inhibition of the leveler and PEG/PPG on the convective top surface efficiently inhibited Cu deposition near the top. Simultaneously, SPS was accumulated on the bottom and developed a growing interface, thereby allowing the bottom-up filling.

In the systemized three-additive composition, filling time was reduced by applying step current. 15 mA/cm^2 of the first step current density was applied for the bottom-up growth, followed by higher current applied to reduce the filling time. PEG/PPG and

leveler were strongly adsorbed near the top surface under the forced convection, which were not desorbed even at the high second step current. Therefore, bottom-up growth continued without Cu deposition on the side walls by applying the step current. The filling time was reduced by about 47% at the optimized deposition condition.

Other types of levelers were additionally suggested to compare the effect on Cu electrodeposition and to improve the filling performance through the modification of the molecular structures. However, the change in the molecular structure (methyl to allyl, hydroxyl to ester, or elongated carbon chain) did not affect Cu electrodeposition. All the levelers contained two quaternary ammonium cations with two iodide anions in common, which implied that the ionic part may dominantly determine the effect of the levelers. Experiments conducted with levelers containing Cl^-, Br^-, or I^- demonstrated that the characteristic as the lever was more obviously observed in the order of Lev(2)-Cl < Lev(2)-Br < Lev(2)-I. This suggested that the halide ions affected the adsorption behavior of the levelers.

To investigate the effect of iodide ion in detail, inorganic NaI was used instead of the synthesized levelers. NaI itself exhibited the characteristic of leveler: convection-dependent adsorption and synergetic inhibition with PEG/PPG. The addition of NaI with SPS and PEG/PPG allowed void-free filling of trenches. Since other ionic

compounds as KI and NH_4I also showed the similar electrochemical behavior and filling results, it was concluded that iodide ion determined the characteristic of the iodide-based levelers.

Finally, TU was added to the three-additive system of SPS, PEG/PPG, and I^- to improve the filling performance. Low concentrations of TU enhanced the adsorption of PEG/PPG, while high concentrations of TU disrupted PEG/PPG suppressing layer. The increased suppression with TU and PEG/PPG also retarded the displacement adsorption of SPS on the side walls of TSV. TSV was filled at 2 mA/cm^2 without voids in the four-additive system containing TU, although filling failed at the same current density in the three-additive system without TU. The filling time was reduced in half in the four-additive composition.

References

[1] P. C. Andricacos, C. Uzoh, J. O. Dukovic, J. Horkans, and H. Deligianni, *IBM J. Res. Dev.*, **42**, 567 (1998).

[2] J. G. Ryan, R. M. Geffken, N. R. Poulin, and J. R. Paraszczak, *IBM J. Res. Dev.*, **39**, 371 (1995).

[3] M. J. Kim, K. J. Park, T. Lim, O. J. Kwon, and J. J. Kim, *J. Electrochem. Soc.*, **160**, D3126 (2013).

[4] M. J. Kim, H. J. Lee, S. H. Yong, O. J. Kwon, S.-K. Kim, and J. J. Kim, *J. Electrochem. Soc.*, **159**, D253 (2012).

[5] G. Schneider, D. Hambach, B. Niemann, B. Kaulich, J. Susini, N. Hoffmann, and W. Hasse, *Appl. Phys. Lett.*, **78**, 1936 (2001).

[6] Chipworks.com. (2016). *Intel's 14-nm Parts are Finally Here!* | *Chipworks*. [online] Available at: https://www.chipworks.com/about-chipworks/overview/blog/intel%E2%80%99s-14-nm-parts-are-finally-here [Accessed 14 Nov. 2016].

[7] ITRS, *International Technology Roadmap for Semiconductors*, 2007, Interconnect.

[8] M. J. Kim, T. Lim, K. J. Park, O. J. Kwon, S.-K. Kim, and J. J. Kim, *J. Electrochem. Soc.*, **159**, D544 (2012).

[9] M. J. Kim, T. Lim, K. J. Park, S. K. Cho, S.-K. Kim, and J. J. Kim, *J. Electrochem. Soc.*, **159**, D538 (2012).

[10] M. J. Kim, T. Lim, K. J. Park, S.-K. Kim, and J. J. Kim, *J. Electrochem. Soc.*, **160**, D3081 (2013).

[11] M. J. Kim, T. Lim, K. J. Park, S.-K. Kim, and J. J. Kim, *J. Electrochem. Soc.*, **160**, D3088 (2013).

[12] J. U. Knickerbocker, P. S. Andry, B. Dang, R. R. Horton, M. J. Interrante, C. S. Patel, R. J. Polastre, K. Sakuma, R. Sirdeshmukh, and E. J. Sprogis, *IBM J. Res. Dev.*, **52**, 553 (2008).

[13] P. S. Andry, C. K. Tsang, B. C. Webb, E. J. Sprogis, S. L. Wright, B. Dang, and D. G. Manzer, *IBM J. Res. Dev.*, **52**, 571 (2008).

[14] C.-T. Ko and K.-N. Chen, *Microelectron. Reliab.*, **50**, 481 (2010).

[15] Yole.fr. (2016). *Yole Développement Press - Advanced Packaging.* [online] Available at: http://www.yole.fr/2014-galery-3D.aspx#I0002f5d1 [Accessed 14 Nov. 2016].

[16] T. Yoshinaga and M. Nomura, *Sci. Technol. Trends*, **37**, 26 (2010).

[17] C. H. Lee, S. Hwang, S.-C. Kim, and J. J. Kim, *Electrochem. Solid-State Lett.*, **9**, C157 (2006).

[18] C. H. Lee and J. J. Kim, *J. Vac. Sci. Technol. B,* **23**, 475 (2005).

[19] C. H. Lee, S. H. Cha, A. R. Kim, J.-H. Hong, and J. J. Kim, *J. Electrochem. Soc.*, **154**, D182 (2007).

[20] T. Lim, H.-C. Koo, K. J. Park, M. J. Kim, S.-K. Kim, and J. J. Kim, *J. Electrochem. Soc.*, **159**, D142 (2012).

[21] T. Lim, K. J. Park, M. J. Kim, H.-C. Koo, K. H. Kim, S. Choe, and J. J. Kim, *J. Electrochem. Soc.*, **161**, D135 (2014).

[22] T. Lim, H.-C. Koo, K. H. Kim, K. J. Park, M. J. Kim, O. J. Kwon, and J. J. Kim, *Electrochem. Solid-State Lett.,* **14**, D95 (2011).

[23] K. H. Kim, T. Lim, M. J. Kim, S. Choe, K. J. Park, S. H. Ahn, O. J. Kwon, and J. J. Kim, *J. Electrochem. Soc.*, **161**, D756 (2014).

[24] F. Inoue, T. Shimizu, T. Yokoyama, H. Miyake, K. Kondo, T. Saito, T. Hayashi, S. Tanaka, T. Terui, and S. Shingubara, *Electrochim. Acta,* **56**, 6245 (2011).

[25] K. J. Park, M. J. Kim, T. Lim, H.-C. Koo, and J. J. Kim, *Electrochem. Solid-State Lett.*, **15**, D26 (2012).

[26] U. Bertocci, *Electrochim. Acta,* **11**, 1261 (1966).

[27] A. Molodov, G. Markosyan, and V. Losev, *Electrochim. Acta,* **17**, 701 (1972).

[28] S. Krzewska, *Electrochim. Acta,* **42**, 3531 (1997).

[29] S. K. Cho, M. J. Kim, and J. J. Kim, *Electrochem. Solid-State Lett.*, **14**, D52 (2011).

[30] Y. Zhu, S. Ma, X. Sun, J. Chen, M. Miao, and Y. Jin, *Microelectron. Eng.*, **117**, 8 (2014).

[31] L. Kong, J. Lloyd, K. Yeap, E. Zschech, A. Rudack, M. Liehr, and A. Diebold, *J. Appl. Phys.*, **110**, 053502 (2011).

[32] A. Nguyen, K. Fealey, P. Reilly, G. Pattanaik, A. Gracias, F. Wafula, M. Flynn, and J. Enloe, *J. Microelectron. Electron. Pack.*, **12**, 43 (2015).

[33] M. J. Kim, S. Choe, H. C. Kim, S. K. Cho, S.-K. Kim, and J. J. Kim, *J. Electrochem. Soc.*, **162**, D354 (2015).

[34] S.-K. Kim, S. Hwang, S. K. Cho, and J. J. Kim, *Electrochem. Solid-State Lett.*, **9**, C25 (2006).

[35] S. K. Cho and J. J. Kim, *J. Electrochem. Soc.*, **153**, C822 (2006).

[36] S. Choe, M. J. Kim, H. C. Kim, T. Lim, K. J. Park, S. K. Cho, S.-K. Kim, and J. J. Kim, *J. Electrochem. Soc.*, **160**, D202 (2013).

[37] S.-K. Kim, S. K. Cho, J. J. Kim, and Y.-S. Lee, *Electrochem. Solid-State Lett.*, **8**, C19 (2005).

[38] S. Choe, M. J. Kim, H. C. Kim, S. K. Cho, S. H. Ahn, S.-K. Kim, and J. J. Kim, *J.*

Electrochem. Soc., **160**, D3179 (2013).

[39] S. K. Cho, S.-K. Kim, and J. J. Kim, *J. Electrochem. Soc.*, **152**, C330 (2005).

[40] S.-K. Kim and J. J. Kim, *Electrochem. Solid-State Lett.,* **7**, C98 (2004).

[41] J. J. Kim, S.-K. Kim, and Y. S. Kim, *J. Electroanal. Chem.,* **542**, 61 (2003).

[42] S. K. Cho, H. C. Kim, M. J. Kim, and J. J. Kim, *J. Electrochem. Soc.,* **163**, D428 (2016).

[43] J. W. Gallaway, M. J. Willey, and A. C. West, *J. Electrochem. Soc.,* **156**, D146 (2009).

[44] J. W. Gallaway, M. J. Willey, and A. C. West, *J. Electrochem. Soc.,* **156**, D287 (2009).

[45] J. W. Gallaway and A. C. West, *J. Electrochem. Soc.*, **155**, D632 (2008).

[46] T. Moffat, D. Wheeler, S.-K. Kim, and D. Josell, *J. Electrochem. Soc.*, **153**, C127 (2006).

[47] S.-K. Cho, M.-J. Kim, H.-C. Koo, S.-K. Kim, and J.-J. Kim, *Bull. Korean Chem. Soc.,* **33**, 1603 (2012).

[48] T. P. Moffat and D. Josell, *Isr. J. Chem.,* **50**, 312 (2010).

[49] T. P. Moffat, D. Wheeler, M. D. Edelstein, and D. Josell, *IBM J. Res. Dev.,* **49**, 19 (2005).

[50] T. Moffat, J. Bonevich, W. Huber, A. Stanishevsky, D. Kelly, G. Stafford, and D. Josell, *J. Electrochem. Soc.*, **147**, 4524 (2000).

[51] Y. Zhang, G. Ding, H. Wang, and P. Cheng, *J. Electrochem. Soc.*, **162**, D427 (2015).

[52] T. Hayashi, K. Kondo, T. Saito, N. Okamoto, M. Yokoi, M. Takeuchi, M. Bunya, M. Marunaka, and T. Tsuchiya, *J. Electrochem. Soc.*, **160**, D256 (2013).

[53] K. Kondo, Y. Suzuki, T. Saito, N. Okamoto, and M. Takauchi, *Electrochem. Solid-State Lett.*, **13**, D26 (2010).

[54] T. Hayashi, K. Kondo, T. Saito, M. Takeuchi, and N. Okamoto, *J. Electrochem. Soc.*, **158**, D715 (2011).

[55] O. Lühn, C. Van Hoof, W. Ruythooren, and J.-P. Celis, *Electrochim. Acta*, **54**, 2504 (2009).

[56] J.-J. Sun, K. Kondo, T. Okamura, S. Oh, M. Tomisaka, H. Yonemura, M. Hoshino, and K. Takahashi, *J. Electrochem. Soc.*, **150**, G355 (2003).

[57] T. Moffat and D. Josell, *J. Electrochem. Soc.*, **159**, D208 (2012).

[58] J. Casas, F. Alvarez, and L. Cifuentes, *Chem. Eng. Sci.*, **55**, 6223 (2000).

[59] D. Josell, D. Wheeler, and T. Moffat, *J. Electrochem. Soc.*, **159**, D570 (2012).

[60] D. Wheeler, T. Moffat, and D. Josell, *J. Electrochem. Soc.*, **160**, D3260 (2013).

[61] L. Yang, A. Radisic, J. Deconinck, and P. M. Vereecken, *J. Electrochem. Soc.*, **161**, D269 (2014).

[62] D. Josell and T. Moffat, *J. Electrochem. Soc.*, **162**, D129 (2015).

[63] D. Josell and T. Moffat, *J. Electrochem. Soc.*, **160**, D3035 (2013).

[64] D. Josell and T. Moffat, *J. Electrochem. Soc.*, **163**, D322 (2016).

[65] O. Lühn, A. Radisic, P. Vereecken, C. Van Hoof, W. Ruythooren, and J.-P. Celis, *Electrochem. Solid-State Lett.*, **12**, D39 (2009).

[66] O. Lühn, A. Radisic, C. Van Hoof, W. Ruythooren, and J.-P. Celis, *J. Electrochem. Soc.*, **157**, D242 (2010).

[67] M. Hayase and K. Otsubo, *J. Electrochem. Soc.*, **157**, D628 (2010).

[68] M. Hayase and M. Nagao, *J. Electrochem. Soc.*, **160**, D3216 (2013).

[69] T. Matsuoka, K. Otsubo, Y. Onishi, K. Amaya, and M. Hayase, *Electrochim. Acta*, **82**, 356 (2012).

[70] C. Madore, M. Matlosz, and D. Landolt, *J. Electrochem. Soc.*, **143**, 3927 (1996).

[71] L. Oniciu and L. Mureşan, *J. Appl. Electrochem.*, **21**, 565 (1991).

[72] C. Madore and D. Landolt, *J. Electrochem. Soc.*, **143**, 3936 (1996).

[73] D. Roha and U. Landau, *J. Electrochem. Soc.*, **137**, 824 (1990).

[74] J. J. Kelly, C. Tian, and A. C. West, *J. Electrochem. Soc.*, **146**, 2540 (1999).

[75] B. Ke, J. J. Hoekstra, B. C. Sison, and D. Trivich, *J. Electrochem. Soc.*, **106**, 382 (1959).

[76] T. C. Franklin, *Surf. Coat. Technol.*, **30**, 415 (1987).

[77] T. C. Franklin, J. Darlington, and R. Fierro, *J. Electrochem. Soc.*, **133**, 893 (1986).

[78] M. S. Kang, S.-K. Kim, and J. J. Kim, *Jpn. J. Appl. Phys.*, **44**, 8107 (2005).

[79] M. Miao, Y. Zhu, M. Ji, S. Ma, X. Sun, and Y. Jin, " Bottom-up Filling of Through Silicon Via (TSV) with Parylene as Sidewall Protection Layer", *11th Electronics Packaging Technology Conference*, pp. 442-446 (2009).

[80] W.-P. Dow, C.-C. Li, Y.-C. Su, S.-P. Shen, C.-C. Huang, C. Lee, B. Hsu, and S. Hsu, *Electrochim. Acta*, **54**, 5894 (2009).

[81] S.-M. Huang, C.-W. Liu, and W.-P. Dow, *J. Electrochem. Soc.*, **159**, D135 (2012).

[82] T. Lu, F. Wang, and Y. He, *J. Electrochem. Soc.*, **163**, D663 (2016).

[83] Z. Lei, L. Chen, W. Wang, Z. Wang, and C. Zhao, *Electrochim. Acta*, **178**, 546 (2015).

[84] A. J. Bard and L. R. Faulkner, *Electrochemical methods, Fundamentals and Application*, 2nd ed., John Wiley & Sons (2001).

[85] D. Josell, D. Wheeler, W. Huber, J. Bonevich, and T. Moffat, *J. Electrochem. Soc.*, **148**, C767 (2001).

[86] D. Josell, D. Wheeler, W. Huber, and T. P. Moffat, *Phys. Rev. Lett.*, **87**, 016102 (2001).

[87] K. Kondo, C. Funahashi, Y. Miyake, Y. Takeno, T. Hayashi, M. Yokoi, N. Okamoto, and T. Saito, *J. Electrochem. Soc.*, **161**, D791 (2014).

[88] D. Suarez and F. Olson, *J. Appl. Electrochem.*, **22**, 1002 (1992).

[89] Z. Wang, H. Wang, P. Cheng, G. Ding, and X. Zhao, *J. Micromech. Microeng.*, **24**, 085013 (2014).

[90] J. J. Kim, S.-K. Kim, and J.-U. Bae, *Thin Solid Films*, **415**, 101 (2002).

[91] H. Marom, M. Ritterband, and M. Eizenberg, *Thin Solid Films*, **510**, 62 (2006).

[92] S. Arai, T. Saito, and M. Endo, *J. Electrochem. Soc.*, **157**, D147 (2010).

[93] A. Mayadas and M. Shatzkes, *Phys. Rev. B*, **1**, 1382 (1970).

[94] K. Kondo, Y. Yamada, and M. Yokoi, *J. Electrochem. Soc.*, **162**, D397 (2015).

[95] S.-K. Kim, D. Josell, and T. Moffat, *J. Electrochem. Soc.*, **153**, C616 (2006).

[96] T. M. Huynh, F. Weiss, N. T. Hai, W. Reckien, T. Bredow, A. Fluegel, M. Arnold, D. Mayer, H. Keller, and P. Broekmann, *Electrochim. Acta*, **89**, 537 (2013).

[97] S. Huemann, N. T. Minh Hai, P. Broekmann, K. Wandelt, H. Zajonz, H. Dosch, and F. Renner, *J. Phys. Chem. B*, **110**, 24955 (2006).

[98] W. Wang and Y.-B. Li, *J. Electrochem. Soc.*, **155**, D263 (2008).

[99] J. G. Long, P. C. Searson, and P. M. Vereecken, *J. Electrochem. Soc.,* **153**, C258 (2006).

[100] S. Choe, M. J. Kim, K. H. Kim, H. C. Kim, J. C. Song, S.-K. Kim, and J. J. Kim, *J. Electrochem. Soc.,* **162**, H294 (2015).

[101] A. Campo, J. Fretti, and N. Vasanthan, *Polymer,* **49**, 374 (2008).

[102] Y. Liu, H. l. n. Antaya, and C. Pellerin, *J. Phys. Chem. B,* **114**, 2373 (2010).

[103] M. J. Willey and A. C. West, *J. Electrochem. Soc.*, **153**, C728 (2006).

[104] Y. Cao, P. Taephaisitphongse, R. Chalupa, and A. C. West, *J. Electrochem. Soc.*, **148**, C466 (2001).

국문 초록

소작의 직접도 증가를 위한 반도체 배선의 미세화 공정은 점차 물리적, 기술적인 한계에 도달하고 있다. 배선 미세화에 의한 한계를 극복하기 위해 실리콘 관통 비아를 사용한 소자의 3차원 적층에 대한 연구가 진행되고 있다. 본 연구에서는, 구리 전해 도금을 통한 실리콘 관통 비아의 무결함 채움을 위해 요오드화물 기반의 평탄제를 제안하고, 실리콘 관통 비아의 채움 메커니즘과 채움 효율 개선을 위한 방법을 소개한다.

기존에 보고된 평탄제의 구조식을 바탕으로, 양이온의 사차 암모늄과 음이온의 요오드화 이온을 포함하는 새로운 평탄제를 제안하였다. 제안한 평탄제는 흡착 세기가 교반 세기에 의존하는 특징을 보이며, 강한 교반 조건에서 구리 전착을 효과적으로 억제하였다. 전기화학 분석을 통해 평탄제를 억제제와 함께 첨가할 경우 억제 세기가 증가하고, 교반이 없는 조건에서는 가속제가 치환 흡착하여 구리 환원이 촉진되는 것을 확인하였다. 가속제, 억제제, 평탄제를 첨가하여 실리콘 관통 비아와 크기가 유사한 트렌치의 채움을 진행하였고, 전기화학 분석 결과와 채움 결과를 바탕으로 트렌치 입구에서는 평탄제와 억제제가 구리 전착을 강하게 억제하며, 트렌치 바닥에서는 가속제가 축적되어 성장 계면을 형성하는 채움

메커니즘을 제안하였다.

3-첨가제 시스템에서의 연구를 바탕으로, 채움 시간을 단축하기 위해 스텝 전류를 인가하였다. 스텝 전류는 바닥 차오름을 진행하기 위한 낮은 전류와, 이후 채움 시간을 단축하기 위해 인가하는 높은 전류로 구성된다. 첫 번째의 낮은 전류를 인가하는 동안 트렌치 바닥에서 가속제의 축적으로 인해 성장 계면이 형성되어 바닥 차오름이 진행된다. 트렌치 입구에 근처에서는 평탄제와 억제제가 강한 교반 조건 하에 구리 전착을 강하게 억제하므로, 높은 전류를 인가하여도 트렌치 벽면에서의 구리 전착이 진행되지 않는다. 따라서 구리 전착은 성장 계면에만 집중되어 계속적인 바닥 차오름을 통해 무결함 채움을 구현할 수 있다. 조건 최적화를 통하여 정전류 채움 방법에 비해 47% 정도 채움 시간을 단축하였다.

첨가제의 구조식 개선을 통한 채움 성능의 향상을 위해, 다양한 구조식의 평탄제를 합성하여 그 영향을 확인하였다. 메틸기를 알릴기로, 수산기를 에스터기로, 그리고 탄소수의 길이를 증가하는 방향으로 평탄제 구조식의 변화를 주었지만 평탄제 종류에 관계없이 유사한 전기화학 분석 결과와 박막 특성 결과가 확인되었다. 각 첨가제는 사차 암모늄 이온과 요오드화 이온을 공통적으로 포함하므로, 해당 작용기가 평탄제의 전반적인 거동을 결정함은 자명하다. 다양한 할로겐화 이온을 포함하는 평탄제를 합성하여

전기화학 분석을 진행한 결과 염화 < 브롬화 < 요오드화 이온의 순서로 평탄제로서의 특성이 명확해졌다.

요오드화 이온의 영향을 추가로 규명하기 위해, 요오드화나트륨을 평탄제로서 첨가하여 분석을 진행하였다. 요오드화 이온은 기존의 유기 평탄제와 동일하게 교반 의존적인 흡착 특성을 보이고, 억제제와 함께 첨가할 경우 억제 세기를 향상시켰다. 또한 순환 전압 전류법을 통해 요오드화 이온이 가속제의 치환 흡착을 억제함을 확인하였다. 요오드화나트륨을 유기 평탄제 대신 첨가하여 트렌치의 무결함 채움을 진행할 수 있었다. 요오드화칼륨, 요오드화암모늄 역시 용액 내에서 이온화되어 요오드 이온을 만들어 무결함 채움을 가능하게 하였고, 요오드화 이온이 평탄제로서의 성능을 결정한다는 것을 뒷받침하였다.

요오드화 이온을 포함하는 3-첨가제 시스템에서 실리콘 관통 비아의 채움을 진행하는 경우, 1 mA/cm^2의 인가 전류 밀도에서는 무결함 채움이 가능한 반면, 2 mA/cm^2에서는 보이드가 형성되었다. 2 mA/cm^2에서의 채움 효율을 개선하기 위해 싸이오요소를 3-첨가제 시스템에 추가하였다. 싸이오요소를 억제제와 함께 첨가할 경우, 낮은 농도의 싸이오요소는 억제제의 흡착 세기를 증진하는 반면, 높은 농도의 싸이오요소는 억제제의 흡착을 방해하였다. 낮은 농도의 싸이오요소는 실리콘 관통 비아의

벽면에서 억제제의 흡착 세기를 개선하는 동시에 가속제의 치환 흡착을 방해하여, 높은 인가 전류에서도 벽면에서의 구리 전착을 억제하고 무결함 바닥 차오름을 가능하게 하였다. 농도 최적화를 통해, 4-첨가제 시스템에서 실리콘 관통 비아의 채움 시간을 3-첨가제 시스템에 비해 2배 이상 단축하였다.

주요어: 실리콘 관통 비아, 구리, 평탄제, 요오드화물, 전해 도금, 정전류 도금, 스텝 전류, 수퍼필링

학 번: 2011-21032

Appendix I

TSV filling with the modified organic additives

I. Introduction

In Chapter 3.1.4, it was examined that I^- contained in the organic additives dominantly determined the function of the additives as the leveler.[1-3] Further researches were conducted to investigate the effect of functional groups (especially the functional groups of suppressors) on the properties of Cu deposit in this Chapter. Previously, an extreme bottom-up filling of the trenches with similar dimensions to those of the TSVs was reported.[4] The trenches were perfectly filled by the galvanostatic electrodeposition with three components of additives: SPS, chemically synthesized suppressor and leveler. Both the suppressor and the leveler contained amine functional groups. With the given combinations of additives, trenches of 40 μm depth and 6 or 8 μm width were filled within 15 min. However, the coarse-grained morphology evolved near the top could potentially contain micro defects, which were required to be modified by

changing the functional groups of the additives to solve this problem.

In this study, the molecular structures of organic additives were modified by changing the functional groups from amines to hydroxyl groups, which is specifically described in the experimental section, to improve the microstructure of the deposited Cu inside the trenches.

II. Experimental

Cu electrodeposition was performed using a standard electrolyte composed of 1.0 M $CuSO_4$, 0.5 M H_2SO_4, and 1.37 mM of Cl^-. Three additives were added in the electrolytes: 5 μM of SPS as an accelerator, 50 μM of S2 (suppressor, product of Samsung Fine Chemicals Co. Ltd.), and 20 μM of L2 (leveler, product of Samsung Fine Chemicals Co. Ltd.). Previously S1, a type of polyoxy polymer with amine terminal groups at both sides and with an average molecular weight between 3,000 and 4,000, was used as the suppressor.[4] Moreover, L1, consisting of pyridine with amine functional group, was synthesized as the leveler.[4] In this study, the molecular structures of the additives were modified; S1 was composed of polyoxy polymer having hydroxyl groups at both sides, with an average molecular weight between 2,000 ~ 3,000. L2, a kind of pyridine derivative, contained hydroxyl groups instead of amine group. Both L1 and L2 contained iodide ion as the counter ion of quaternary ammonium cation, which implied that L1 and L2 would show similar effect on Cu deposition.

The electrodeposition and electroanalytical measurements were performed using a three-electrode system including a working electrode, and electronic grade Cu rod and Ag/AgCl electrode (KCl saturated) as the counter and reference electrodes,

respectively. The temperature of the electrolytes was maintained at 25 °C by using a thermostat. All the experimental conditions for the filling were the same as described in Chapter 2.1.3, except the applied current density. 10 mA/cm^2 was applied for the filling of 9 μm-width TSV-scaled trenches at 900 rpm. Cu was deposited on the blanket wafer composed of Cu seed layer (50 nm, PVD)/Ta (35 nm, PVD)/SiO_2 to clarify the effect of additives on the microstructure of the deposited Cu. Before the electrodeposition of Cu, the native oxide of the blanket wafer was removed by chemical wet etching by immersing it in an aqueous solution of 0.03 M citric acid and 0.034 M potassium hydroxide for 2 min.[5] Cu was electrochemically deposited onto the oxide-etched coupon wafer at a current density of 10 mA/cm^2 with a deposition charge of 2800 mC/cm^2.

III. Results and discussion

The gap-filling images were previously obtained by adding SPS and chemically synthesized suppressor, S1 (polyoxy polymer with amine terminal groups, Mw = 3000 ~ 4000), and leveler, L1 (pyridine derivative with an additional amine group), as shown in Fig. 1.[4] All the trenches were uniformly filled with overburdens at a current density of 6.5 mA/cm^2 for 30 min. The suggested filling mechanism was supported by the results of LSV, CV, and potential-time curve.[4] The accumulation of SPS at the bottom established the growing surface, which promoted the bottom-up filling. The co-adsorption of S1 and L1 severely inhibited the Cu deposition at the lateral wall and top of the trenches, enabling the void-free filling. Note that the filling mechanism is just the same as that discussed in Chapter 3.1.1. Although the additive chemistry of SPS-Cl^--S1-L1 facilitated the extreme bottom-up filling under the galvanostatic condition, the coarse-grained morphology near the top of the trenches were expected to contain defects as shown in Fig. 1.

S2 (polyoxy polymer with hydroxyl terminal groups, Mw = 2000 ~ 3000) and L2 (pyridine derivative with an additional hydroxyl group) were synthesized as a suppressor and leveler, respectively, to improve the microstructure near the top of the

trenches. Prior to the trench filling, the effect of the additives on the Cu deposition was electrochemically investigated. The electrochemical effects of S2 and L2, or their combinations with SPS, showed analogous tendency to those of S1 and L1, which implied that S2 and L2 might also induce the same filling mechanism.

The most important demerit of the gap-filling with S1-L1-SPS was the formation of coarse grains near the opening of the trenches as shown in Fig. 1. Therefore, the effects of the additives (S2 and L2) on the microstructure were examined by depositing Cu on the blanket surface. The surface morphology and cross-sectional images of the Cu deposits by adding S1-L1-SPS or S2-L2-SPS at rotating speeds of 0 and 900 rpm are shown in Fig. 2. As shown in Figs. 2a and 2c, uniform and relatively smooth Cu films were deposited at 0 rpm (0 rpm of rotating speed replicates the convection condition at the bottom of trenches), irrespective of the additives used. The brightening effect of SPS,[6] efficiently displacing S1 or S2 only at the stationary condition, resulted in the deposition of flat films at 0 rpm. Note that S1-L1-SPS resulted in the non-uniform deposition of Cu (not shown here) at 900 rpm (900 rpm replicates the conditions near the top of the trenches), and the image in Fig. 2b was from the area where Cu deposition took place. Even the deposited Cu had a rough surface, which was closely related to the coarse-grained microstructure evolved near the top during the trench

filling. It was considered that either S1 or L1 predominantly determined the uneven deposition of Cu, because SPS did not efficiently function under the strong convection at 900 rpm. In contrast, by adding S2-L2-SPS, the surface morphology was improved than that with S1-L1-SPS based on the modified functional groups. In conclusion, the combination of S2-L2-SPS was expected to have an advantage in regard to the microstructure of the deposited Cu, provided that S2-L2-SPS induced the successful bottom-up filling.

To investigate the major factors affecting the microstructure or deposit morphology, Cu was deposited on the blanket wafer with the sole addition of S1 or S2 into the standard electrolyte. In contrast to L1 or L2, inducing the uniform deposition of Cu films (not shown here), the suppressors significantly affected the morphology and uniformity of Cu deposit. As shown in Figs. 3a and 3b, Cu was locally deposited under both the stationary and convective conditions by adding S1. The surface morphologies were divided into two areas, A and B; Cu was selectively deposited in area A, whereas negligible deposition occurred in area B. In the area B, hemispherical nodules with about 1 ~ 2 μm in diameter were sparsely observed. In contrast, relatively uniform Cu films were deposited by adding S2 irrespective of the rotating speed, as shown in Figs. 3c and 3d. The surface morphology of the deposited Cu was also slightly affected by

the rotating speed which determined the surface concentration of Cu^{2+}. Actually, the deposited Cu by adding S1 or S2 showed different morphology according to the rotating speed, although S1 or S2 exhibited electrochemically similar inhibition strength regardless of the convective conditions.

Generally, the uniformity of the additives' distribution strongly affects the deposition morphology. The adsorption uniformity of additive is determined by the simultaneous adsorption and desorption on the surface during Cu electrodeposition. Therefore, based on the results in Figs. 2 and 3, we surmised that S1 had poor uniformity in coverage because Cu was selectively deposited on the surface, resulting in a severe lump deposition. In contrast, S2, containing hydroxyl functional groups with improved adsorption uniformity than that of S1, enabled the even deposition and growth of Cu. While S1 induced abnormal deposition of Cu near the top, thereby resulting in the coarse-grained microstructure, the addition of S2 improved Cu microstructure by its uniform surface coverage. Furthermore, the uniform adsorption of S2 also induced the uniform coverage of L2 which co-adsorbed with S2, thereby improving the microstructure from coarse to smooth one. In conclusion, S2 was considered to improve the grain structure near the top of the trenches, because S2 improved the microstructure of the deposited Cu when added with SPS and L2.

The additive chemistry composed of SPS, S2, and L2 enabled the uniform trench filling with overburdens as shown in Fig. 4. In contrast with the coarse deposit near the top in Fig. 1, smooth deposit was maintained until the end of the filling with S2-L2-SPS. As the filling propagated toward the trench opening, S1-L1 or S2-L2 mainly affected the properties of Cu deposit owing to the gradually increased convection. In contrast with S1-L1-SPS, the uniform and bright Cu film was deposited with S2-L2-SPS even at 900 rpm, as shown in Fig. 2, inducing the deposition of smooth-grained Cu near the top. The modification of the functional groups effectively improved the microstructure near the top without severe deterioration in the filling performance.

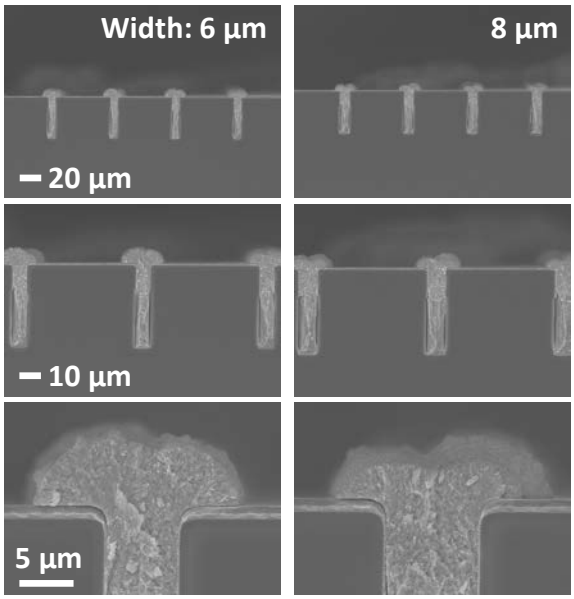

Fig. 1. The previous results of the gap-filling profiles by adding SPS, S1, and L1. Trenches with 40 μm depth were filled at a current density of 6.5 mA/cm^2 for 30 min; the images from Ref. 1.

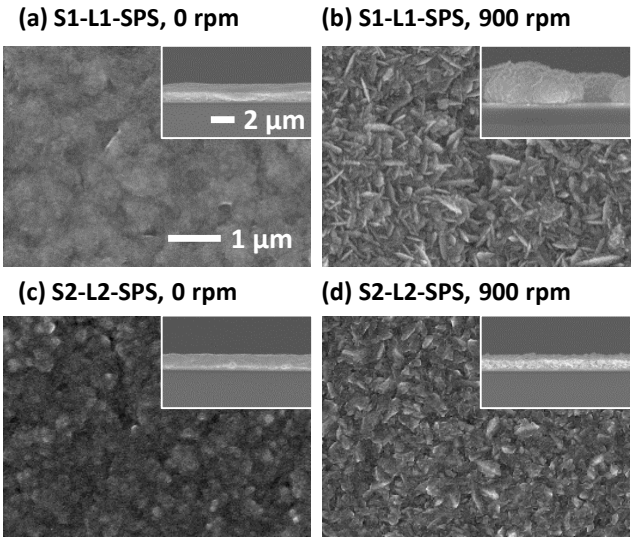

Fig. 2. The deposit structure of Cu on the blanket wafer by adding S1-L1-SPS (a) at 0 rpm and (b) at 900 rpm or S2-L2-SPS (c) at 0 rpm and (d) at 900 rpm.

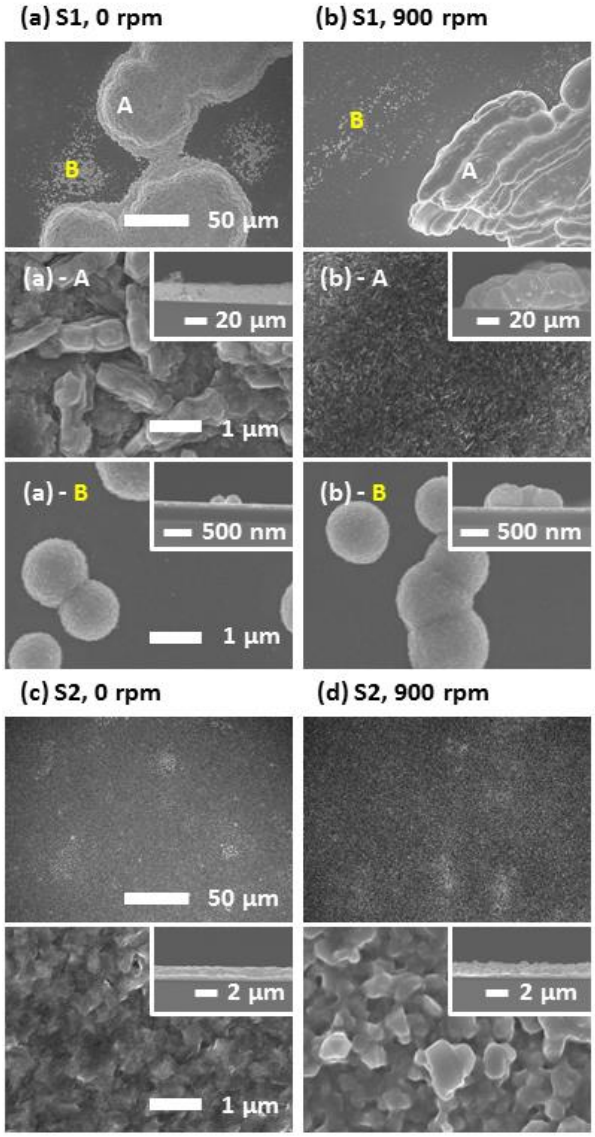

Fig. 3. The deposit structure of Cu on the blanket wafer by adding S1 at (a) 0 rpm, (b) 900 rpm, and S2 at (c) 0 rpm, (d) 900 rpm. In Figs. 3a and 3b, the surface was divided into two regions, A and B; A where Cu was locally deposited and B where Cu was negligibly deposited with the hemispherical nodules.

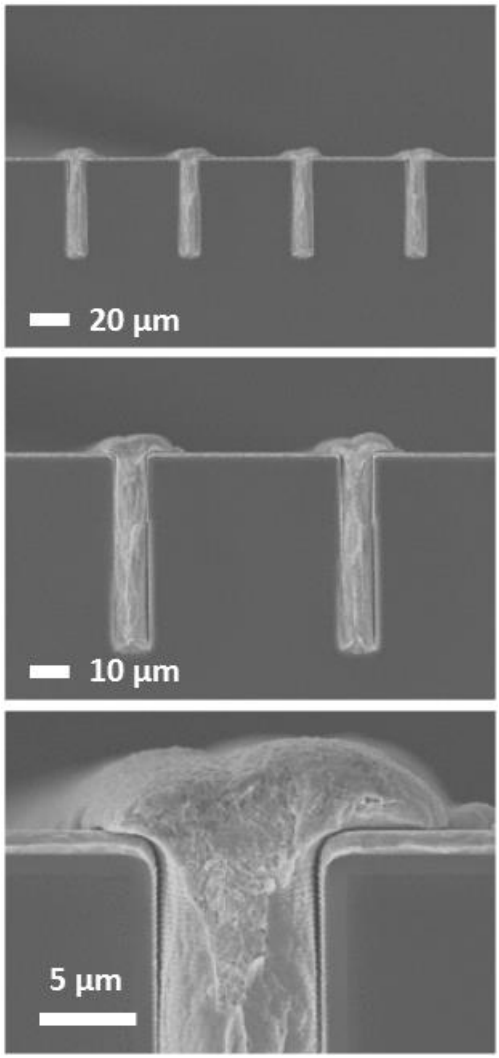

Fig. 4. The cross-section images of Cu filled trenches with S2-L2-SPS at a current density of 10 mA/cm^2 for 25 min.

IV. Conclusion

The proper modification of the functional groups, i.e., from amine to hydroxyl terminal groups, or the increase in the adsorption uniformity of the suppressor improved the microstructure of the deposited Cu, which was a main drawback of the previously used S1 and L1. Uniform Cu film that was not obtained with the addition of S1-L1-SPS at 900 rpm was deposited by adding the modified additives (S2 and L2 with SPS). It was concluded that S2 dominantly induced the deposition of uniform Cu surface through the uniform adsorption density. The improved uniformity of Cu deposit corresponded to the smooth-grained microstructure near the top of Cu-filled TSV.

V. References

[1] M. J. Kim, Y. Seo, H. C. Kim, Y. Lee, S. Choe, Y. G. Kim, S. K. Cho, and J. J. Kim, *Electrochim. Acta*, **163**, 174 (2015).

[2] M. J. Kim, Y. Seo, J. H. Oh, Y. Lee, H. C. Kim, Y. G. Kim, and J. J. Kim, *J. Electrochem. Soc.*, **163**, D185 (2016).

[3] M. J. Kim, H. C. Kim, and J. J. Kim, *J. Electrochem. Soc.*, **163**, D434 (2016).

[4] M. J. Kim, H. C. Kim, S. Choe, J. Y. Cho, D. Lee, I. Jung, W.-S. Cho, and J. J. Kim, *J. Electrohem. Soc.*, **160**, D3221 (2013).

[5] M. J. Kim, S. K. Cho, H.-C. Koo, T. Lim, K. J. Park, and J. J. Kim, *J. Electrochem. Soc.*, **157**, D564 (2010).

[6] J. J. Kim, S.-K. Kim, and Y. S. Kim, *J. Electroanal. Chem.*, **542**, 61 (2003).

Appendix II

Effect of Benzotriazole (BTA) and TU on the Cu film properties

I. Introduction

As aforementioned, the properties of Cu deposit can be improved by adding additives. As the additives affect the Cu deposition depending on the functional groups containing S, N, or O, the behavior of additives has been actively investigated.[1-3] Therefore, the basic research on examining the effect of functional groups on the properties of Cu deposit is required to set direction for the development of new additives. In this Chapter, the effect of additives on the film properties is investigated by adding benzotriazole (BTA), BTA derivatives, and TU.

BTA, which is a well-known corrosion inhibitor as well as leveler, provides effective grain refining.[4] It was reported that the nitrogen atoms in BTA supply their electrons to the cuprous ion to form a Cu-BTA complex, which becomes a stable adsorbent on Cu surface.[5] Several models have been presented to explain the interaction between BTA

and the Cu ion or the Cu surface; a model of adsorption by the BTA-Cu-BTA bidentate polymer or a model of bonding between the unshared electrons in BTA and Cu surface.[6,7]

TU also acts as an effective brightening agent through strong adsorption on metal substrates, which affects the various properties of the metal films.[8] Particularly, TU can reduce the grain size of metal films by adsorbing onto the nucleation sites of substrates.[9] The adsorption mechanism of TU has been investigated using either infrared (IR) or surface enhanced raman spectroscopy (SERS). The spectra of adsorbed TU indicated that the TU adsorbed onto the Cu surface through the sulfur atom.[10,11] Furthermore, the adsorption mechanism of TU and the TU/formamidine disulfide ($S_2C_2(NH)_2(NH_2)_2$, FDS) redox pair have been electrochemically investigated.[12] As shown in the equation [1] below, two molecules of TU could be oxidized into one molecule of FDS, which is a side reaction during the Cu reduction/dissolution process.

$$2TU \rightleftarrows FDS + 2H^+ + 2e^- \qquad [1]$$

TU is also oxidized to FDS, thereby simultaneously reducing Cu^{2+} to Cu^+, as shown in the equation [2].[13]

$$2TU + 2Cu^{2+} \rightleftarrows FDS + 2Cu^+ + 2H^+ \qquad [2]$$

As TU either forms a redox pair with FDS [1], or simultaneously reduces Cu^{2+} [2], the

effect of these reactions on the Cu electrodeposition as well as stable adsorption of TU complex needs to be examined.

By considering the above research, the effect of two additives, BTA and TU, on Cu deposition is investigated in this work. At first, electroanalytical results and Cu film characteristics resulting from the additions of BTA and its derivatives are presented in relation to the number of nitrogen atoms. Research on the distribution of the nitrogen atoms in BTA derivatives is focused because the unshared electron pair of nitrogen atoms determines Cu film properties. Secondly, the effect of TU on Cu electrodeposition through derivatization has been discussed in depth. Derivatization, a method of coating additives on the electrode by dipping into an additive-containing electrolyte, is introduced to properly control the properties of the electrodeposited Cu. The derivatization method can be applied either to verify the adsorption mechanism of TU or to improve the resistivity problem, accompanying an enhancement in the hardness and reduction in the magnitude of high resistivity.

II. Experimental

2.1. Electrochemical analysis and Cu film deposition

The electrochemical experiments were performed in a three-electrode system involving Cu rotating disk electrode (RDE), electronic grade Cu rod, and Ag/AgCl (KCl saturated) as working, counter, and reference electrodes, respectively. The electrolyte used for Cu electrodeposition was composed of 0.25 M $CuSO_4 \cdot 5H_2O$ and 1.0 M H_2SO_4, and the temperature of the electrolyte was maintained at 30°C. BTA, benzimidazole, 1H-benzotriazole-1-methanol (BTA-MeOH), indazole, and indole, whose molecular structures are shown in Fig. 1, were used to compare the electrochemical effect of BTA and its derivatives. The main structural differences among these additives were the number and distribution of the nitrogen atoms, the structural similarity among them was that they all included the benzene ring. Since additives containing more than 4 nitrogen atoms have different molecular structures, BTA and its derivatives having fewer than 3 nitrogen atoms were selected, to exclude any structural effects on Cu film deposition. Each of the additives was added in amounts 0.42 mM, 0.7 mM, 1 mM, and 1.4 mM.

In the case of TU experiment, 1.4 mM of TU or 0.7 mM of formamidine disulfide (FDS), known as being produced by the oxidation of TU, was added to the Cu electrolyte. The derivatization was conducted by dipping the Cu RDE into the Cu electrolyte containing 1.4 mM of TU for several seconds. Then the derivatized-RDE was rinsed by dipping it into the stagnant deionized water, followed by gently blowing the electrode surface with N_2 gas. The mild rinsing and blowing processes had a negligible influence on the surface coverage of pre-adsorbed TU, since TU chemically adsorbed on the Cu electrode. Then, electrochemical analysis was done in the additive-free standard electrolyte. In the three-electrode system, LSV was conducted from 0 mV (vs. open circuit potential (OCP), which corresponded to +50 mV vs. Ag/AgCl) to -600 mV (vs. Ag/AgCl) at a scan rate of 10 mV/s.

The Cu films were electrochemically deposited using a Cu blanket wafer composed of Cu seed layer (40 nm, PVD)/Ta (7 nm, PVD)/SiO_2/Si as the working electrode. The counter and reference electrodes used for the film deposition were same as those used in the electrochemical analysis. Prior to the Cu electrodeposition, the surface oxide of Cu wafer was efficiently removed by immersing the wafer into a solution composed of 0.03 M citric acid and 0.034 M potassium hydroxide for 2 min. After the pretreatment, Cu films were deposited galvanostatically by applying 15 mA/cm^2 or by applying a

constant potential of -200 mV (vs. Ag/AgCl) with the total deposition charge of 1400 mC with the PAR 273A potentiostat (EG&G Princeton Applied Research Corporation). The thicknesses of the Cu films were controlled to 550 nm (± 50 nm). The deposited films were rinsed with deionized water, and then, the samples were blow-dried with N_2 gas.

2.2. Analysis of deposition characteristics

Film properties were analyzed 5 days after the deposition. X-ray diffractometer (XRD, D8 Advance, Bruker) having Cu Kα 1 (0.154 nm) was used to study the crystallographic orientations and full width at half maximum (FWHM) of the Cu films. FWHM induced by the diffractometer was calculated to be 0.0513° using standard reference material 660a, LaB_6, provided from National Institute of Standards and Technology (NIST). The measured FWHM values were corrected considering this instrumental FWHM to exclude the peak broadening effect induced by the diffractometer. Sheet resistance and film thickness were measured with a 4-point probe (CMT-SR1000N, Chang Min Tech Co.) and by field emission scanning electron microscopy (FESEM, S-4800, Hitachi), respectively, to calculate resistivity. Surface

morphology images were presented by both FESEM and atomic force microscopy (AFM, XE-150, Park Systems). A nanoindenter (MTS XP, MTS Systems Co.) was used to measure film hardness. A Berkovich tip (three-sided pyramid shape) made of diamond was employed as the indenter, and hardness was measured as the indenter penetrated the sample from the surface. From the load and indented area according to the depth of penetration, hardness could be calculated. To remove the unreliable data on the hardness near the surface and the substrate effect, the average hardness for displacement range of 150 nm to 250 nm from the surface was calculated.

The mass changes in the Cu electrode based on the dipping time into various electrolytes, which were either devoid of or containing TU were measured on QCA 917 (EG&G Princeton Applied Research Corporation). A commercially available 300 nm thick sputter deposited Cu electrode was used for the quartz crystal microbalance (QCM), and 0.196 cm^2 of the QCM electrode was exposed for the analysis. Prior to each measurement, the surface oxide of the Cu electrode was removed using cathodic polarization, which was conducted by applying 5 mA for 300 s in 0.1 M sulfuric acid. Then, the frequency of the QCM electrode was measured without any externally applied potential based on the dipping time in the electrolyte either containing or devoid of TU.

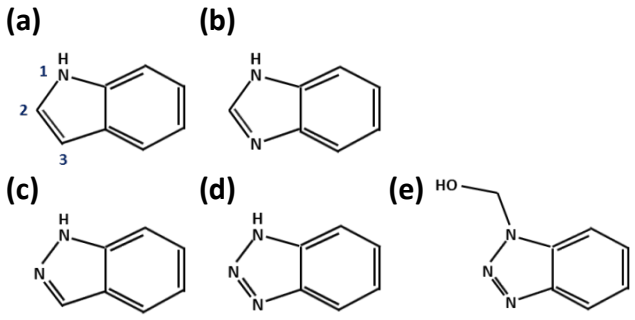

Fig. 1. Molecular structures of (a) indole, (b) benzimidazole, (c) indazole, (d) BTA, and (e) BTA-MeOH. Note that the additives can be grouped according to their number of N atoms in the azole group.

III. Results and discussion

3.1. Effect of BTA and its derivatives on Cu electrodeposition

The molecular structure of each additive is shown in Fig. 1. Indole (a) has one nitrogen atom at site #1, whereas benzimidazole (b) and indazole (c) have two nitrogen atoms at sites #1 and #3, and at sites #1 and #2, respectively. Both BTA (d) and BTA-MeOH (e) have three nitrogen atoms, while nitrogen #1 of BTA-MeOH is covalently bonded to a methanol group.

As described in Fig. 2, LSV was conducted according to the amount of additive to verify the behavior of each additive in Cu electrodeposition. Indole of 0.42 mM did not have any inhibition effect, but indole of more than 0.70 mM had a slight inhibition effect up to about 0 mV to -30 mV and then provided I-V characteristics similar to those of additive-free case. In Fig. 2b and 2c, benzimidazole does not present a clear electrochemical activity, while indazole inhibited Cu deposition. Indazole showed a slight inhibition effect up to 50 mV ~ 0 mV according to its concentration, and then yielded current profiles similar to those given by indole at low concentrations (0.42 mM and 0.70 mM). Indazole of 1.0 mM gave slightly low currents from about -200 mV,

and that of 1.4 mM inhibited Cu deposition in almost all potential ranges. In Fig. 2d and e, BTA and BTA-MeOH having 3 nitrogen atoms progressively suppress the deposition rate until -200 mV ~ -250 mV according to their concentrations. The overlapped LSV with 1.4 mM of each additive is described in Fig. 2f. The inhibition strengths of the additives were in the order of BTA ≈ BTA-MeOH > indazole ≈ indole > benzimidazole for the concentrations examined. Comparing the current profiles of indazole and benzimidazole, which contained 2 nitrogen atoms, we can speculate that the locations of nitrogen atoms also affect the inhibition ability of an additive, and that the Cu reduction is strongly inhibited when the nitrogen atoms are adjacent (at site #1 and #2). In brief, molecules having 3 nitrogen atoms, i.e. BTA and BTA-MeOH, are needed to greatly inhibit Cu electrodeposition.

BTA is known to produce Cu-BTA complex film, especially in the structure of a bidentate polymer.[6,7] Although the formation of a BTA polymeric film may be deteriorated in acidic conditions, an adhesion layer of tens of angstrom may be constructed.[5,14] Furthermore, BTA can be adsorbed on the Cu surface directly through the bonding between its nitrogen and the copper atoms, as well. Indole, benzimidazole, and indazole, which contain 1 or 2 nitrogen atoms, can also function as corrosion inhibitors producing their own complexes,[15] but these additives have lower complex-

formation ability and corrosion inhibiting efficiency than BTA.[6] Actually the additives containing 1 or 2 nitrogen atoms provided electrochemically weak inhibition, as shown in Fig. 2, which means that the adsorption strength or stability of complex produced with these additives may be lower than that of a complex produced with BTA. Based on this result, compared to the other additives having a fewer number (1 or 2) of nitrogen atoms, BTA was revealed to have effective complex-formation ability with Cu^{+}; high adsorption ability on the Cu surface due to its sufficient number (3) of nitrogen atoms; and efficient inhibition effect on Cu deposition.

Accordingly, adsorption strength may be closely related to the number of nitrogen atoms; this relation can be supported by the strong inhibition effects of BTA and BTA-MeOH, as revealed by the electroanalytical results. Although a methanol functional group may sterically hinder one of the nitrogen atoms in BTA-MeOH, BTA-MeOH shows similar behavior to BTA through the conversion of BTA-MeOH into BTA in acidified electrolyte. BTA-MeOH can also produce a stable complex through a hydrogen bond between hydroxyl group and nitrogen atom,[16] which can strongly inhibit Cu reduction.

The XRD patterns and (111) peak intensities of the Cu films are demonstrated in Fig. 3a and Fig. 3b, respectively. In Fig. 3a, only the peak related to Cu (111) was clearly

observed in the deposited Cu films within the scan range of 30° - 60°. The crystal plane of (222), which naturally accompanies the development of (111), was detected at 95° (not shown here). Other crystal planes, except (111) or (222), were not observed even at the slower scan rate of 1.5°/min. Since (111) crystallographic orientation is preferentially grown in thin Cu films to minimize the surface energy,[17] only (111) peak was analyzed in Fig. 3a. Though the crystal plane developed in the seed layer can contribute to the measured peak intensities of Cu films, the change of the (111) intensity according to the additive can reasonably be discussed without considering the seed effects since Cu seed layer has almost the same influence on all samples. Indole and indazole of both 1.4 mM reduced the peak intensity of Cu (111) by 40% from that of additive-free electrodeposition, while benzimidazole did not decrease the peak intensity clearly. BTA and BTA-MeOH induced a notable decrease of Cu (111) peak intensity of about 96% at maximum. FWHM according to the concentration of each additive was plotted in Fig. 3c. Benzimidazole showed no apparent change in FWHM regardless of its concentrations, similar to the results in Fig. 3b. Additions of 1.4 mM of indole and indazole increased FWHM by about 18% from that of additive-free electrodeposition. Additions of 1.4 mM of BTA and BTA-MeOH showed 1.5-time (compared to indole and indazole) and 1.7-time (compared to benzimidazole) higher

FWHMs, respectively, which indicates a much smaller grain size. Since the adsorption of grain refiners retards the surface mobility of Cu adatoms, the adsorption strength of the additives is strongly related to grain size. Relatively lower (111) peak intensities and higher FWHMs with additions of BTA and BTA-MeOH owing to their strong adsorption correspond to the result of Fig. 2.

The surface morphologies of Cu films deposited with 1.4 mM of indole, indazole, and BTA were investigated by AFM and SEM in Fig. 4. Crystallite size presented in Fig. 4a was calculated from Scherrer's equation with the result of FWHM in Fig. 3c. In terms of calculating crystallite size from FWHM, peak broadening according to the microstrain in the films was not excluded, which means the actual grain size can be larger than the noted crystallite size. However, the change of the exact grain size from back scattered electron (BSE) images exhibits the same tendency as the change of $FWHM^{-1}$, so the influence of each additive on grain size can be verified reasonably without additional consideration of the microstrain effect. Moreover, in Fig. 4, the aggregate size shown in the AFM or SEM images changed dramatically according to the additives, compared to crystallite size, which was calculated from diffractometer measurements. However, one protrusion from AFM or SEM images can contain several grains, which can definitely be verified using BSE image, so the crystallite

sizes from XRD were compared quantitatively in this research. Actually, some aggregates in the SEM images were divided into several smaller grains in the BSE images. BSE images of Cu deposits with 1.4 mM of indole, indazole, and BTA are presented in Fig. 5, and the size distribution of surface grains measured from the BSE images is shown as Fig. 5e. Though similar surface morphologies were verified between the BSE and SEM images, a more exact and clear distribution of the surface grains was identified, as shown in Fig. 5. Average sizes of the surface grains of the additive-free Cu films, and Cu films with additives inole, indazole, and BTA were 74.6, 58.3, 60.5, and 38.4 nm, respectively, which were slightly higher than those from XRD. However the variation of grain size for each additive was in excellent agreement with those calculated from Scherrer's equation (noted in Fig. 4). This implies that the change of crystallite sizes calculated from Scherrer's equation could reasonably be used even though the influence of the Cu seed layer or the microstrain on FWHM may affect the exact calculation.

Without any additives, the crystallite size of the Cu film was calculated as 70 nm. The Cu films deposited with indole and indazole showed smaller mean crystallite sizes of 57 nm and 60 nm, respectively, than that of films deposited with no additive. The addition of BTA resulted in crystallite size of 37 nm, which was 35% smaller than the

crystallite sizes of the film deposited with either indole or indazole. AFM results indicated increased surface roughness in the order of indole, indazole, and BTA, which can also be verified in the SEM images of Fig. 4e-h. It is important to note that BTA and BTA-MeOH improved surface roughness through their efficient grain refining, as described in Fig. 3.

Resistivity results with additive concentrations are shown in Fig. 6. Resistivity was maintained or increased slightly with the addition of indole, indazole, or benzimidazole. On the other hand, the film deposited with either 1.4 mM BTA or 1.4 mM BTA-MeOH showed 8 or 9-time higher resistivity than the Cu film deposited in an additive-free bath. To ascertain the reason for this high resistivity, several factors, such as phonon scattering, grain boundary scattering, surface scattering, and scattering at an impurity (or point defect) can be considered. Since all the samples were analyzed at the same temperature, phonon scattering probably had a negligible effect on their resistivities. Sufficient thickness of greater than 500 nm can minimize the influence of surface scattering on resistivity. Therefore, it can be concluded that resistivity is dominantly governed by grain boundary scattering. BTA and BTA-MeOH function as effective grain refiners, which produce high density grain boundaries, which in turn increase resistivity. Incorporation of BTA on Cu films, as previously suggested by other papers,

can also contribute to the increase of resistivity.[18]

The hardness variation for 1.4 mM of each additive is shown in Fig. 7. The Cu film deposited with indole (including 1 nitrogen atom) shows 2.3 GPa, which is similar to the hardness value of the Cu film deposited in an additive-free bath. Benzimidazole and indazole (both containing 2 nitrogen atoms) slightly increased the hardness to 2.4 GPa. BTA and BTA-MeOH with 3 nitrogen atoms increased the hardness up to 3.9 and 3.2 GPa, which are 1.7-time and 1.4-time higher value than the hardness of the Cu film deposited without an additive, respectively. In agreement with the result of LSV and grain size, the effective construction of a Cu-BTA complex can promote the stable adsorption of additives on the Cu surface. Consequently, the reduced grain size due to the addition of BTA or BTA-MeOH can intensively retard dislocation movements, thereby improving film hardness. Also impurities due to the incorporation of additives can enhance hardness, as well, by impeding the propagation of dislocation. The strong adsorption of BTA or BTA-MeOH makes them more favorable additives for incorporation into Cu films, and enlarged amounts of impurities imposes lattice strain to restrict the dislocation movement.

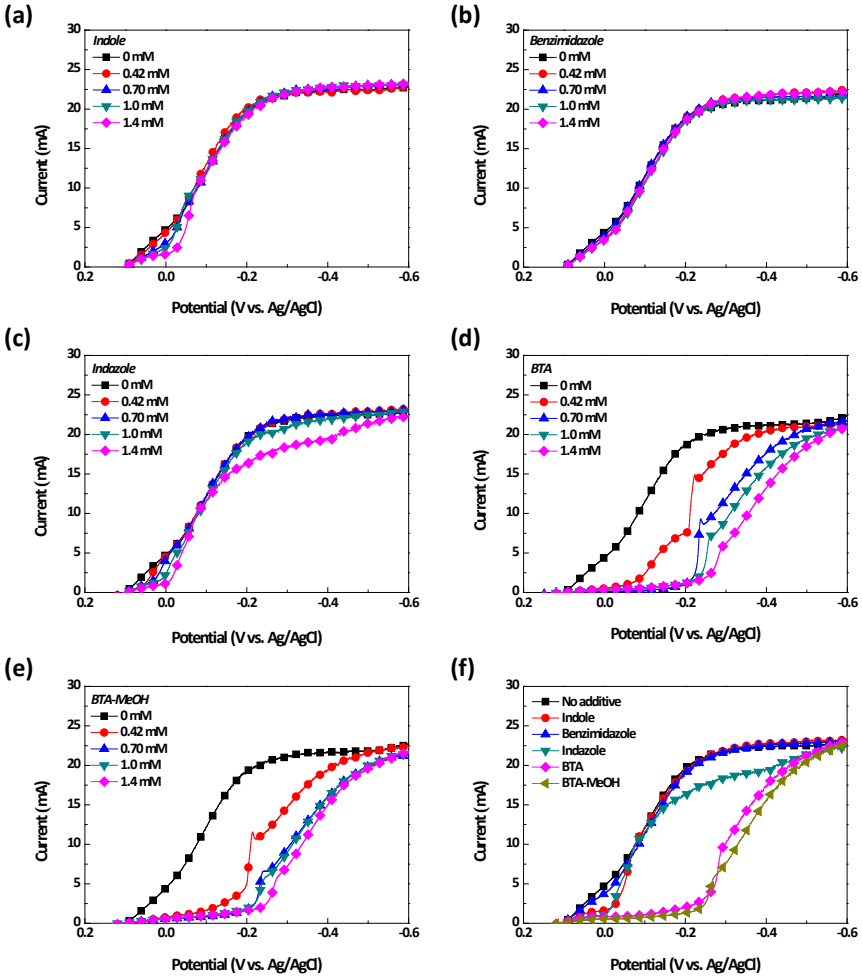

Fig. 2. LSV results of (a) indole, (b) benzimidazole, (c) indazole, (d) BTA, (e) BTA-MeOH, and (f) overlapped result with 1.4 mM of each additive. All the experiments were performed with the potential sweep rate of 10 mV/s.

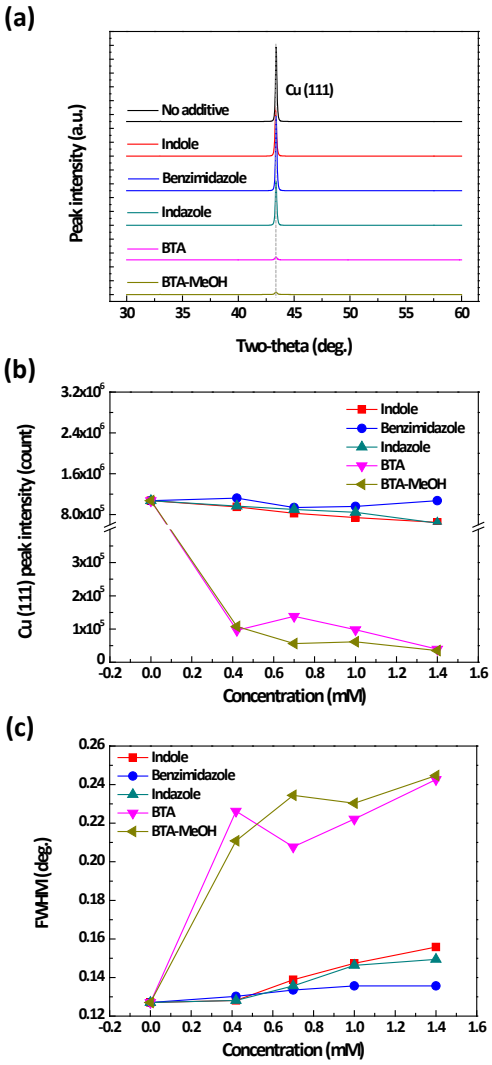

Fig. 3. (a) XRD pattern of 1.4 mM of each additive, (b) Cu (111) peak intensity, and (c) FWHM for various concentrations of BTA and its derivatives.

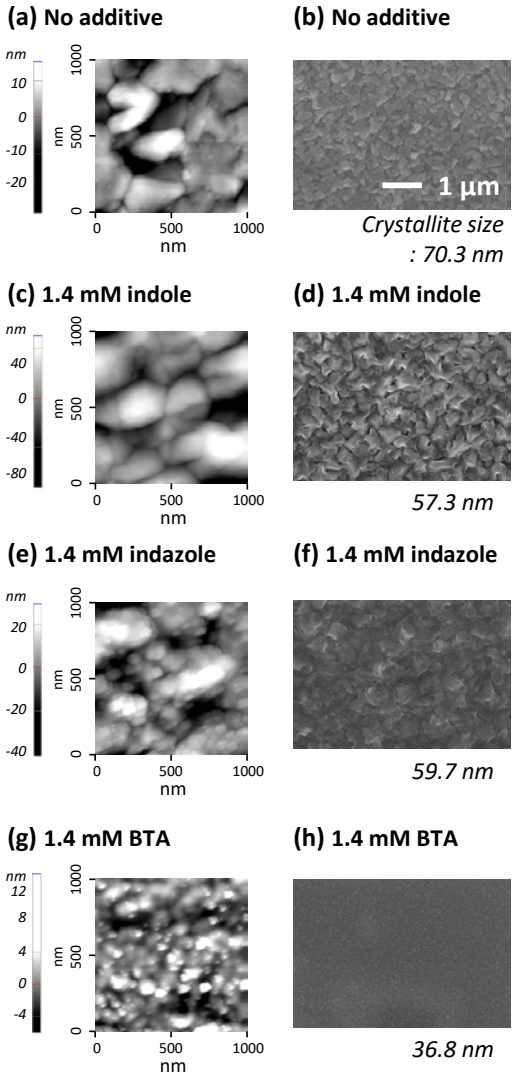

Fig. 4. Surface morphology from AFM and SEM images with (a), (b) no additive; and with 1.4 mM of (c), (d) indole; (e), (f) indazole; and (g), (h) BTA, respectively, and the crystallite sizes below AFM images were calculated using Scherrer's equation from Fig. 3c.

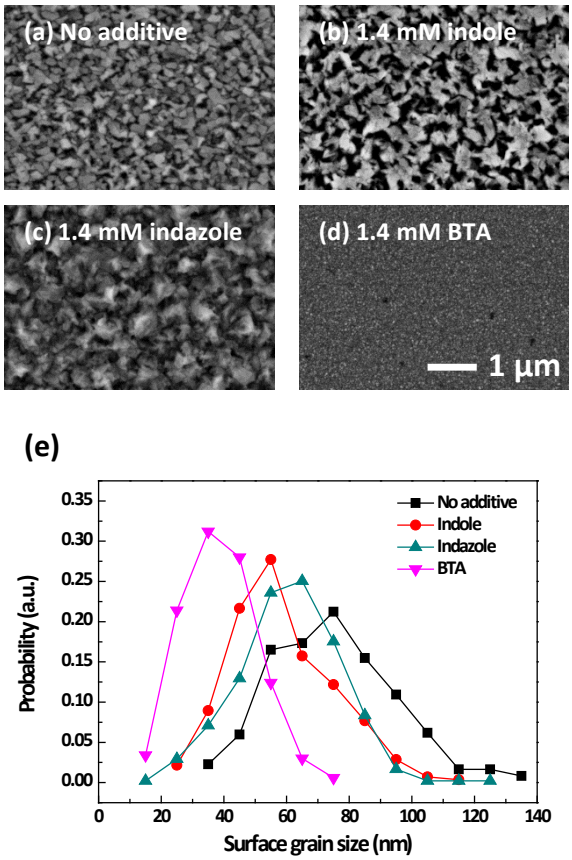

Fig. 5. BSE images of Cu films deposited (a) without additive and with 1.4 mM of (b) indole, (c) indazole, and (d) BTA, respectively, and (e) the size distribution of surface grains for each additive.

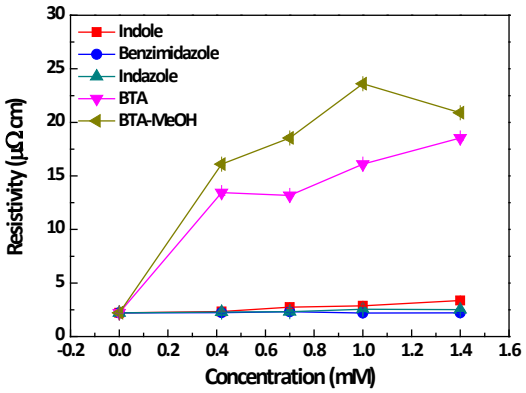

Fig. 6. Resistivity for various concentrations of BTA and its derivatives.

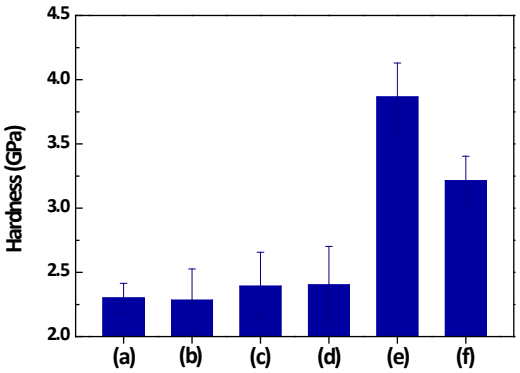

Fig. 7. Hardness measured without (a) additive, and with 1.4 mM of (b) indole, (c) benzimidazole, (d) indazole, (e) BTA, and (f) BTA-MeOH.

3.2. Electrodeposition of Cu films using the derivatization method of TU

Based on the voltammetry studies conducted in the electrolyte containing 1.4 mM of TU, Fig. 8a, TU significantly inhibited the Cu reduction until about -240 mV. In Fig. 8b, the LSV results based on the TU derivatization time of 5, 30, 60, 120, and 180 s are presented. For the durations of 5 s and 30 s, the additional cathodic current, i.e., an acceleration effect from OCP to -100 mV was observed. The derivatization duration of 60 s generally inhibited the Cu reduction with a slight acceleration near 0 mV, whereas the Cu deposition was effectively inhibited up to -230 mV after the derivatization over 180 s, analogous to the voltammetry of bulk addition (Fig. 8a).

The strong adsorption of TU on the Cu surface efficiently inhibited the Cu reduction as shown in Fig. 8a. Several investigations on the adsorption mechanism of TU have been performed using IR, SERS, and electrochemical methods. Papapanayiotou et al. reported that the TU adsorbed onto the Cu surface through the sulfur atom by verifying the change in the C-N and C-S bond orders using in-situ IR.[19] Fabricius et al. used a rotating ring disk electrode in solutions of sulfuric acid to electrochemically verify the formation of the TU-Cu^{+} complex.[20] TU coordinated to Cu^{+} through the sulfur atom, and it was considered that the complexed Cu^{+} was possibly coordinated by the Cu

surface to exert a strong adsorption and suppression of the Cu deposition.

In contrast with the general behavior of TU as an inhibitor, the adsorbed TU within 30 s of derivatization (Fig. 8b) showed an acceleration effect. Cu is reduced via a two-step reaction as shown below.

$Cu^{2+} + e^- \rightleftarrows Cu^+$ [3]

$Cu^+ + e^- \rightleftarrows Cu$ [4]

Reaction [3] is the rate determining step, and the Cu reduction is promoted by increasing the reaction rate of [3].

As shown in reaction [2], TU can spontaneously reduce Cu^{2+} to Cu^+. Since the reaction [2] is kinetically favorable to occur even in the acidified solution of 2.0 M H_2SO_4,[21] it can also proceed in the given acidic condition of 1.0 M H_2SO_4. The TU adsorbed onto the electrode with relatively low surface coverage during TU derivatization of < 30 s, and the adsorbed TU of low coverage effectively reduced Cu^{2+} to Cu^+ at the electrode surface during the electrodeposition step, thereby accelerating the Cu reduction. The derivatization duration of longer than 60 s induced high coverage of TU-Cu^+, which inhibited the Cu reduction. As the derivatization time increased, Cu^+ was continuously generated at the electrode surface by the reaction [2] or the dissolution of Cu electrode. The generated Cu^+ continued to form TU-Cu^+

complex with the TU during the derivatization step, and the adsorbed complex inhibited Cu reduction in the electrodeposition step. Since P. Cofré et al. reported that the reaction did not occur in the ratio higher than $[Cu^{2+}]$:[TU]=100:1,[22] the reaction [2] was assumed to hardly proceed homogeneously in the given electrolytic condition of $[Cu^{2+}]$:[TU]=250:1.4. Accordingly, it could be concluded that the highly accumulated coverage of TU during the derivatization made the forward direction of reaction [2] kinetically favorable on the electrode surface, even though the information on the activities or concentrations of species in reaction [2] are limited.

To sum up, the surface coverage of the TU based on the derivatization time has a direct relationship to either the adsorption state or complex-formation-ability of TU. In other words, the low surface coverage of TU caused the acceleration while the high density of adsorbed TU inhibited the deposition. In the case of the electrolyte containing TU (Fig. 8a), the TU-Cu^{+} complex was sufficiently formed with the continuous supply of TU from the bulk electrolyte, and the Cu reduction was dominantly suppressed.

The LSV was conducted in the sulfuric acid electrolyte devoid of the copper ion to additionally elucidate the action of TU. The voltammetry performed in 1.0 M sulfuric acid with 1.4 mM of TU is shown in Fig. 9a. Only slight inhibition up to -150 mV was

observed with the TU. The results of LSV after the derivatization of up to 180 s, (Fig. 9b), indicated a considerable increase in the current based on the derivatization time. As shown in Fig. 9a, the dissolution of Cu RDE in an acidic electrolyte generates only small amounts of Cu^{+}, which can further form complexes with TU, exhibiting extremely weak inhibition. However, the overall voltammetric response with the addition of TU approximated that without TU especially after -150 mV. This suggested that the supply of Cu^{2+} was required to implement a clear inhibition (Fig. 8b), by continuously generating Cu^{+} which formed the inhibiting complex with TU. The pre-adsorbed TU during the derivatization (Fig. 9b) spontaneously reduced Cu^{2+} dissolved from Cu RDE in the acidic LSV bath. In addition, it increased the reduction current based on the derivatization time. In contrast with the LSV results (Fig. 8b) showing a decrease in the current with longer derivatization times (> 60 s), currents increased in all the given derivatization times (Fig. 9) owing to an absence of Cu^{2+} in the bulk electrolyte. Cu^{2+} was not continuously supplied from the bulk electrolyte, and TU, which did not form an inhibiting complex efficiently with Cu^{+}, was just used to reduce Cu^{2+} to Cu^{+}, thereby increasing the current in voltammetry even with the derivatization time of 180 s. It was also noteworthy that the current scale in Fig. 9 was much smaller than that shown in Fig. 8 owing to the absence of Cu^{2+} in the bulk electrolyte.

The LSV and AFM measurements after the derivatization in either sulfuric acid or base Cu electrolyte, devoid of TU, were performed to verify the effect of roughness generated during the derivatization (Fig. 10). The LSV was conducted in the sulfuric acid electrolyte after the derivatization in either sulfuric acid (Fig. 10a) or Cu electrolyte (Fig. 10b) free from TU for 0-180 s. In Fig. 10a, the current did not change until -150 mV regardless of the derivatization time, followed by a slight increase in the current after -150 mV with derivatization. On the other hand, the current increased (Fig. 10b) with a peak at -60 mV after the derivatization was performed in the Cu electrolyte free from TU, while the significant peak current at 0 mV seen in Fig. 9b was not observed. To investigate the effect of roughness on voltammetry, the surface roughness of the wafer immersed in the given electrolytes was measured using AFM, as shown in Fig. 10c. The Cu blanket wafer was dipped into sulfuric acid, Cu electrolyte, and Cu electrolyte containing TU for 30 s prior to measuring the surface roughness. In Fig. 10c, surface roughness increased by a meager 20% after the immersion in sulfuric acid. However, the roughness increased more than 2.4 -times after dipping in Cu electrolyte either with or without TU. A higher dissolution rate of Cu in the electrolyte containing Cu^{2+} owing to the comproportionation-disproportionation,[23] which will be discussed later in Fig. 12, increased the surface roughness compared to that observed in the

sulfuric acid devoid of Cu^{2+}. A change in the roughness based on the electrolyte corresponded to the voltammetry results; a slight increase in the current and roughness with the derivatization in the sulfuric acid (Fig. 10a), and a relatively striking change in the current and roughness with the derivatization in the Cu electrolyte either without (Fig. 10b) or with TU (Fig. 9b). The increased surface roughness can induce a larger surface area of electrode, thereby establishing higher current in voltammetry. The reduction of Cu^{2+} based on the oxidation of adsorbed TU, furthermore, increased the current. This was because the peak current at 0 mV was only observed after the derivatization in the standard Cu electrolyte containing TU (Fig. 9b), which was not observed with the derivatization in the Cu electrolyte devoid of TU (Fig. 10b). Based on the voltammetry results obtained in sulfuric acid, the surface roughness contributed to an increase in the current, while the reduction of Cu^{2+} based on the adsorbed TU during the derivatization affected the voltammetry especially around 0 mV.

The generated FDS on the electrode surface by the oxidation of TU possibly affected Cu reduction, and the effect of FDS was electrochemically examined (Fig. 11). 0.7 mM of FDS was added, because two molecules of TU chemically reacted to form one molecule of FDS from the reaction [2]. The FDS weakly inhibited the Cu reduction by forming the FDS-Cu^{+} complex,[24] as shown from the voltammetry studies (Fig. 11a)

conducted in the Cu electrolyte containing FDS. TU or FDS coordinated to Cu^{+} through the interaction between electron-rich sulfur and electron-deficient Cu^{+}. Since FDS, an oxidized state of TU, contained less electrons available for the coordination in the sulfur atom than TU, FDS exhibited weaker coordination ability and inhibition strength. As shown in Fig. 11b, the LSV was carried out using the same derivatization method as referenced in Fig. 8b. The FDS slightly accelerated the Cu reduction with the derivatization of < 30 s (current increase of 2 mA at 0 mV), and exhibited inhibition, which was weaker than that of TU with a longer derivatization time. As shown in Fig. 11b, the FDS adsorbed during the short derivatization was seemed to be reduced to TU electrochemically during the potential sweep, as the reverse reaction of [1], and the generated TU at the Cu electrode promoted Cu reduction. To sum up, the adsorbed FDS with short derivatization could work as a catalyst, that is, stabilize the transition state of reaction [3], which was derived by summing up the backward reaction of [1] and forward reaction of [2]. However, this multi-step reaction including the electro-reduction of FDS increased the current by only 2 mA at 0 mV, while the current increased to about 5.5 mA after the derivatization in the Cu electrolyte containing TU (Fig. 8b). This behavior rationalized the acceleration effect of TU. The electrochemical reduction of FDS to TU during the voltammetry did not increase the

reduction current (Fig. 11b) because the current related to the FDS reduction was not observed when the LSV was conducted in sulfuric acid free from Cu^{+} with 0.7 mM of FDS.

The adsorption state of additives during the derivatization was also investigated using QCM. The change of electrode mass during the immersion in sulfuric acid containing 1.4 mM TU is depicted in Fig. 12a, and that in Cu electrolyte containing 1.4 mM TU and 0.7 mM FDS is shown in Figs. 12b-c. In QCM, the measured frequency according to the analysis time can be converted to the change rate of mass, w (g/s).

In Fig. 12a, the mass of the Cu electrode decreased with the dipping time owing to the dissolution of Cu under acidic conditions. The reduction ratio of the electrode mass decreased by about 42% with the addition of TU into the sulfuric acid owing to the formation of the TU-Cu^{+} complex that inhibited the Cu dissolution, wherein Cu^{+} was formed from the dissolution of the Cu electrode. As shown in Fig. 12b, the dissolution rate in the Cu electrolyte increased by about 62% than that in sulfuric acid because Cu metal and adjacent Cu^{2+} reacted to form Cu^{+}, while the comproportionation-disproportionation promoted the dissolution rate of Cu in the Cu electrolyte. This might probably be the reason for the enhanced surface roughness when the Cu electrode was dipped into the solution containing both sulfuric acid and copper sulfate

as shown in Fig. 10c. When the TU was added to the Cu electrolyte, the mass increased until 150 s, followed by a decrease after 230 s. With the addition of FDS into the Cu electrolyte (Fig. 12c), the dissolution was suppressed by about 57%, without any increase of mass in the initial stage.

Either the TU or FDS formed a complex with the dissolved Cu^{+}, and the adsorbed complex inhibited the dissolution of Cu as shown in Fig. 12a or 12c. However, the mass of the Cu electrode rather increased in the Cu electrolyte containing TU (Fig. 12b). The surface images of the Cu wafer after dipping in various electrolytes were analyzed with SEM (Fig. 13), to investigate the change in the surface. The Cu wafer was immersed into the Cu electrolyte either with or without TU, and sulfuric acid containing TU for 120 s, and dendrites developed on the Cu surface only in the Cu electrolyte containing TU. The Cu^{+} near the Cu surface was reduced to Cu again by the oxidation of TU, which contributed to the formation of dendrites. Expectedly, instead of being reduced, the resulting Cu^{+} formed a TU-Cu^{+} complex that showed a high resistance to being reduced, as previously discussed. However, Suarez et al. reported that the complex state of Cu^{+} could be changed based on either the concentrations of TU or applied current density; high formation ratio of FDS-Cu^{+} with low TU concentration or low applied current, and predominance of TU-Cu^{+} with the converse

conditions.[24] We conducted QCM or dipping experiments without any externally applied current, and the two products of the reaction [2], Cu^+ and FDS, preferentially formed the FDS-Cu^+ complex rather than the TU-Cu^+ complex during the short dipping time. The Cu^+ in the FDS-Cu^+ complex was spontaneously reduced to Cu metal by the oxidation of TU, thereby either increasing the mass of the QCM electrode (Fig. 12b) or forming dendrites (Fig. 13b) because the FDS-Cu^+ exhibited higher reducibility compared to TU-Cu^+ as inferred from the weak inhibition strength of FDS (Fig. 11). The dendrites were not formed in the wafers immersed in the standard Cu electrolyte devoid of TU (Fig. 13c) and the sulfuric acid free from Cu^{2+} but containing only TU (Fig. 13d) owing to the absence of the reducing agent, TU, and the relatively negligible quantity of Cu^{2+}/Cu^+ source, respectively. Although additional analyses are required to investigate the adsorption states of TU and their effects more clearly, it is noteworthy that the possible use of TU as a reducing agent to accelerate the Cu reduction was verified from these experimental results. When the dipping time was longer than 200 s (Fig. 12b), the high adsorption density of TU dominantly coated the electrode surface with the TU-Cu^+ complex, which had high resistance to reduction. The spontaneous reduction of Cu^{2+} was suppressed with the highly covered TU-Cu^+ complex after 200 s (Fig. 12b), and the mass of QCM electrode began to decrease after 200 s owing to the

dissolution. In contrast to TU, the electrode mass did not increase (Fig. 12c), thereby, just inhibiting the Cu dissolution by the formation of the FDS complex because the FDS was not oxidized to reduce Cu^{2+}.

TU showed varying electrochemical behavior with the adsorption densities, and the film properties could be changed moderately using TU derivatization, instead of the drastic change in the film properties when deposited in the electrolyte containing TU.

To verify the effect of TU derivatization on Cu film characteristics, the Cu films of 500 nm thickness were deposited without any additive, after the TU derivatization, and in the electrolyte containing TU. As shown in Fig. 1b, the voltammetry with the sufficient derivatization time of 180 s showed analogous current profiles to that observed for the TU-added electrolyte. To clearly distinguish the effect of the deposition methods on the properties of the Cu film, a short derivatization time of 5 s was applied. The XRD patterns and Cu (111) peak intensities are shown in Figs. 14a-b, and the average sizes of (111) grain were calculated using Scherrer's equation in Fig. 14c. From Fig. 14b, the intensity of Cu (111) decreased in the following order: additive-free > TU derivatization > TU, and 2.1% and 26.2% reduced grain sizes than those of the additive-free were measured with TU derivatization and with the addition of TU, respectively. The strong adsorption of TU on the Cu surface impeded the

surface movement of Cu adatoms, and suppressed the growth of the preferred orientation, (111), and grain. After the derivatization, the development of (111) grains was inhibited at the interface of the Cu seed layer and the electrolyte owing to the adsorbed TU. However, the pre-adsorbed TU was gradually incorporated or desorbed as the Cu film was deposited, permitting the growth of (111) grains. The gradual increase of (111) orientation from near the seed layer to the surface of the Cu film, which was examined from the properties of Cu films deposited with various thickness after the derivatization, resulted in the averagely larger (111) intensity and grain size compared to those of films deposited with the addition of TU. The thickness dependency of film properties in derivatization can also explain the results of hardness and resistivity, which will be discussed later.

The hardness of the Cu films deposited under the above-mentioned conditions in Fig. 14 is presented in Fig. 15. In comparison to the hardness of the film electroplated in an additive-free bath, a 38.0% increase in the hardness was measured with the addition of TU, while the hardness increased by 9.2% with TU derivatization. The hardness of the films depended on the mobility of the dislocations, and because higher energy is required for the dislocations to pass through the grain boundary compared to that needed to move within a single grain, the hardness was enhanced by the high density

of the grain boundaries. The impurities incorporated into the film could also restrict the propagation of dislocations by imposing lattice strains around the impurities. The TU increased both grain boundary density and impurity amounts, which induced high hardness of Cu films, and the hardness was also improved by just using TU derivatization without the bulk addition of TU.

The measured resistivity under the given deposition conditions is shown in Fig. 16. The resistivities increased by 26.0% and 700.0% after the derivatization and with the addition of TU, respectively, compared to that without any additive. The resistivity is determined by the electron scattering either at the grain boundaries or microstrains induced by impurity.[25] TU increased the resistivity by rendering high density of grain boundaries and large amount of impurities. In comparison to the resistivity of a film deposited with TU, the lower resistivity was measured with TU derivatization, thereby circumventing the problems caused by a severe increase in resistivity, when TU was added.

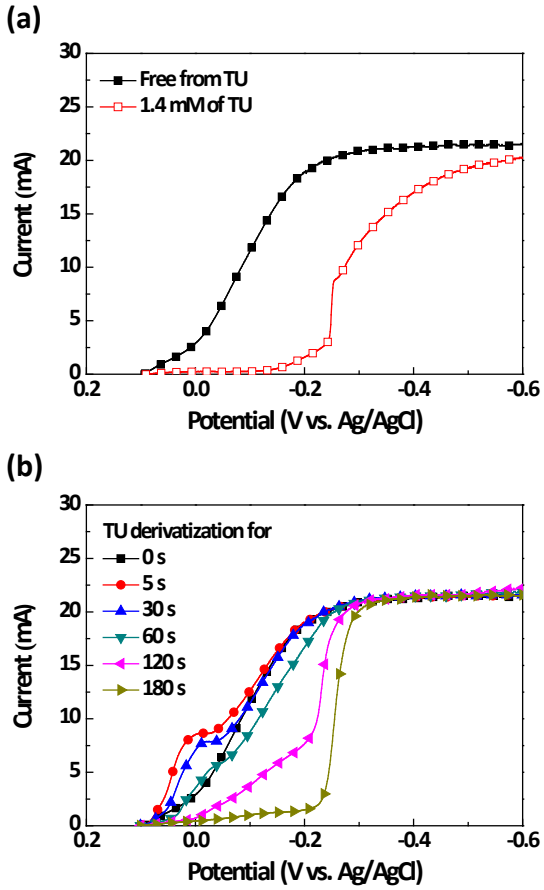

Fig. 8. (a) LSV in 0.25 M $CuSO_4$ + 1.0 M H_2SO_4 containing 1.4 mM TU, (b) derivatization of Cu electrodes in 0.25 M $CuSO_4$ + 1.0 M H_2SO_4 containing 1.4 mM TU for 0 - 180 s, followed by LSV in 0.25 M $CuSO_4$ + 1.0 M H_2SO_4 devoid of TU.

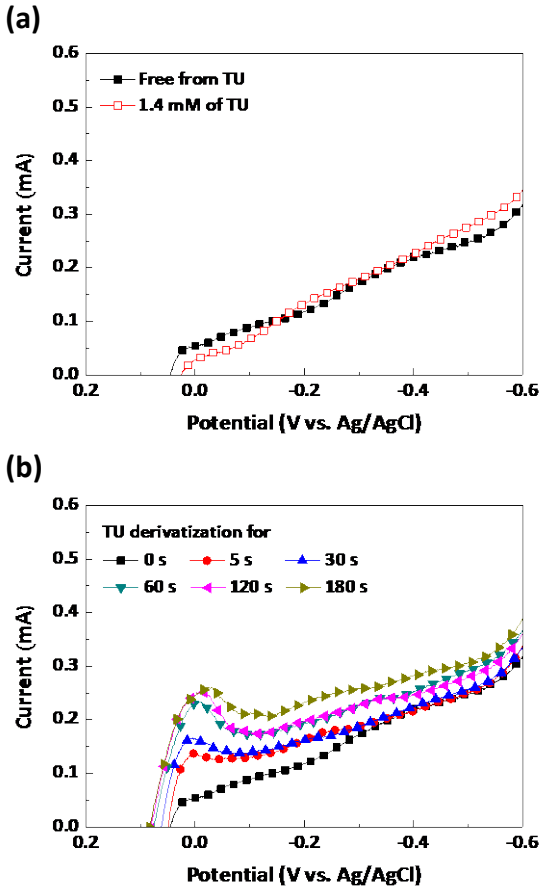

Fig. 9. (a) LSV in 1.0 M H_2SO_4 containing 1.4 mM TU, (b) derivatization of Cu electrodes in 0.25 M $CuSO_4$ + 1.0 M H_2SO_4 containing 1.4 mM TU for 0 - 180 s, followed by LSV in 1.0 M H_2SO_4 devoid of TU.

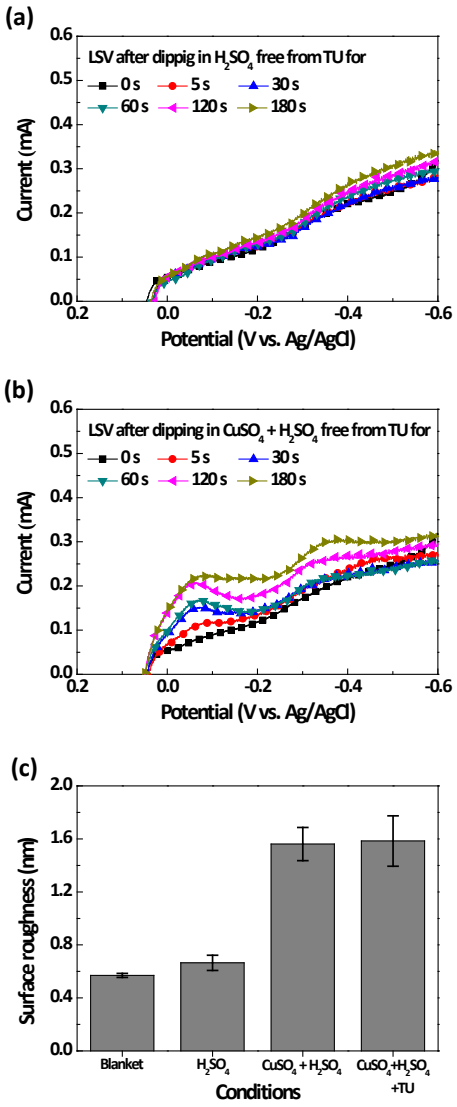

Fig. 10. LSV in 1.0 M H_2SO_4 with derivatization of Cu electrodes in (a) 1.0 M H_2SO_4, (b) 0.25 M $CuSO_4$ + 1.0 M H_2SO_4 without any additives for 0 - 180 s, (c) surface roughness after immersing electrode into electrolytes, sulfuric acid, Cu electrolyte, Cu electrolyte containing TU, for 30 s.

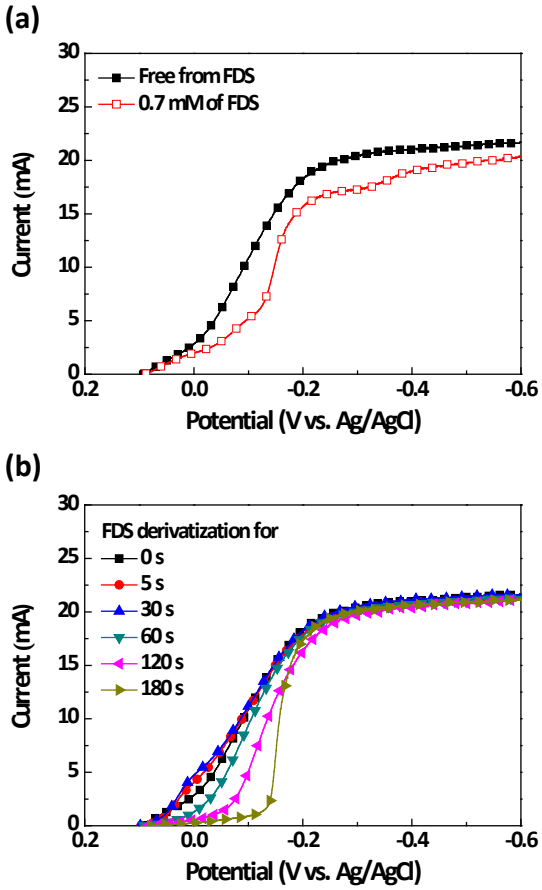

Fig. 11. (a) LSV in 0.25 M $CuSO_4$ + 1.0 M H_2SO_4 containing 0.7 mM FDS, (b) derivatization of Cu electrodes in 0.25 M $CuSO_4$ + 1.0 M H_2SO_4 containing 0.7 mM FDS for 0 - 180 s, followed by LSV in 0.25 M $CuSO_4$ + 1.0 M H_2SO_4 without any FDS.

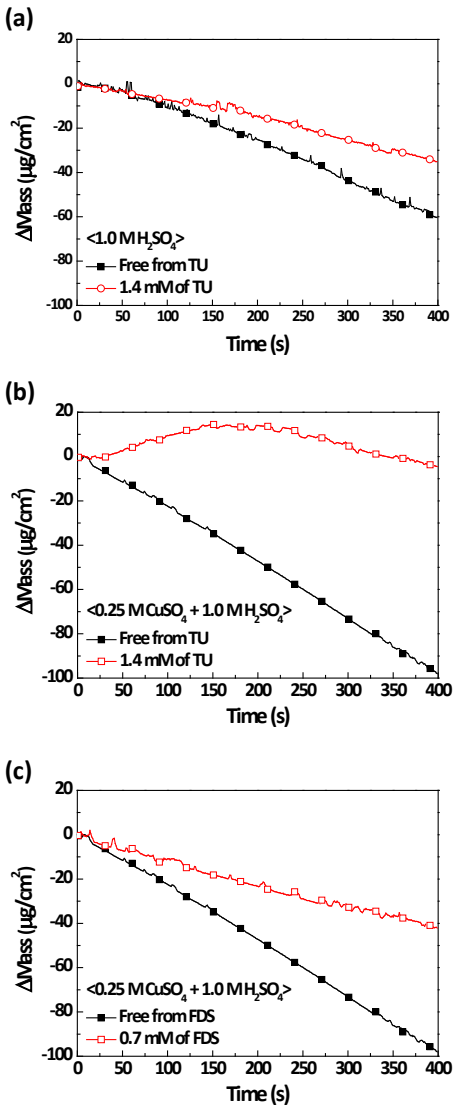

Fig. 12. QCM from (a) 1.0 M H_2SO_4 containing 1.4 mM TU, (b) 0.25 M $CuSO_4$ + 1.0 M H_2SO_4 containing 1.4 mM TU, and (c) 0.25 M $CuSO_4$ + 1.0 M H_2SO_4 containing 0.7 mM FDS, respectively.

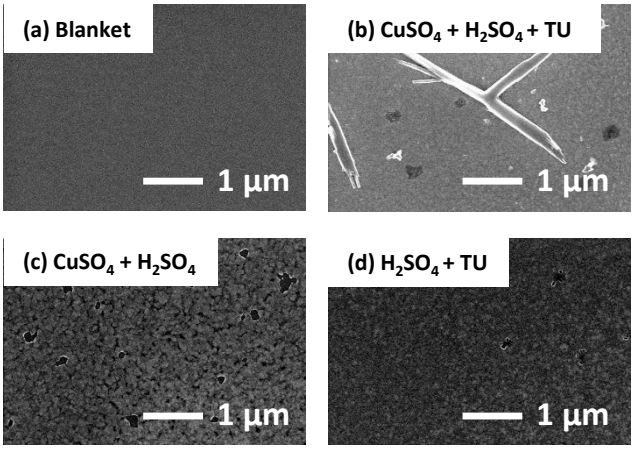

Fig. 13. Surface SEM images of (a) blanket Cu wafer, and after immersion into electrolytes (b) Cu electrolyte containing TU, (c) Cu electrolyte, and (d) sulfuric acid electrolyte containing TU for 120 s.

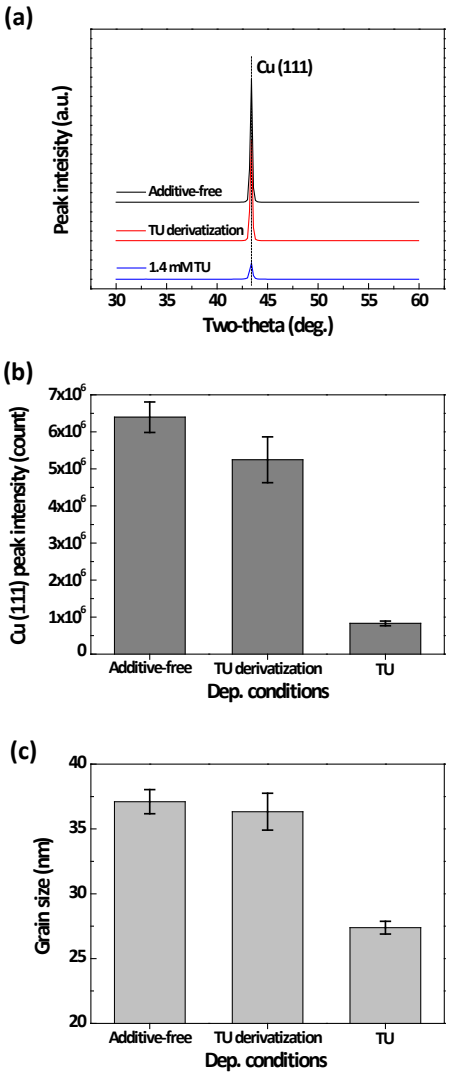

Fig. 14. (a) XRD pattern, (b) Cu (111) peak intensity, and (c) grain size of Cu films deposited under three different conditions; additive-free, derivatization with 1.4 mM TU, and electrolyte containing 1.4 mM TU. Grain size was calculated using Scherrer's equation.

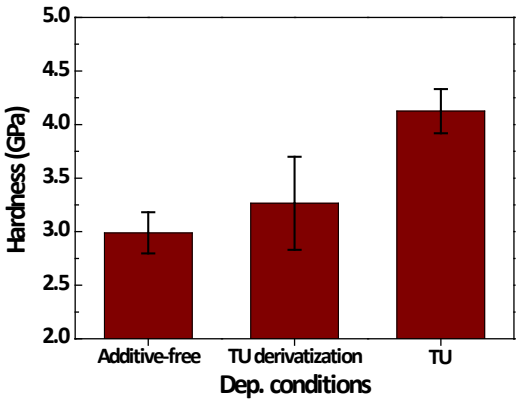

Fig. 15. Hardness of Cu films deposited in additive-free electrolyte, after derivatization with 1.4 mM TU, and in the electrolyte containing 1.4 mM TU.

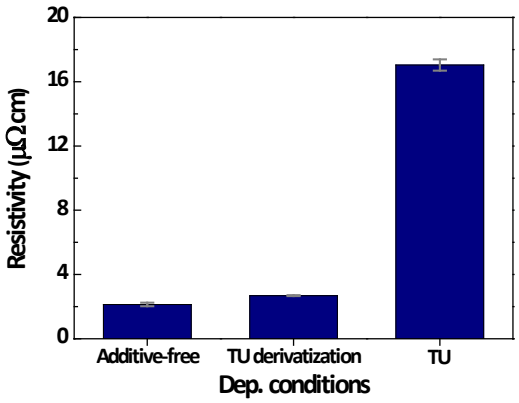

Fig. 16. Resistivity of Cu films deposited in additive-free electrolyte, after derivatization with 1.4 mM TU, and in the electrolyte containing 1.4 mM TU.

IV. Conclusion

The effect of BTA and its derivatives on Cu electrodeposition were examined. The BTA and its derivatives used in this paper were categorized according to their number of nitrogen atoms in the azole group: indole having 1 nitrogen atom, benzimidazole and indazole both having 2 nitrogen atoms, and lastly, BTA and BTA-MeOH having 3 nitrogen atoms. Additives with 3 nitrogen atoms, BTA and BTA-MeOH, strongly inhibited Cu electrodeposition, as shown by the I-V characteristics. Moreover, the Cu films deposited with additions of BTA and BTA-MeOH showed 35% smaller grain size, as well as 1.5- time increased hardness than the Cu films deposited with additions of the other additives containing fewer nitrogen atoms. BTA-family additives constructed a stable complex with the cuprous ion by donating the unshared electron pair of nitrogen atoms to the electron-deficient cuprous ion. This donation emphasizes the significance of the number of nitrogen atoms in determining the complex-formation ability and adsorption strength of an additive; this relation was validated by the remarkable grain refining behavior of BTA and BTA-MeOH. Additional investigations about the effect of additives having different nitrogen atom distributions, numbers, and diverse nitrogen-functional groups remain as future work.

Furthermore, the bifunctional effect of adsorbed TU was electrochemically verified using derivatization. TU with low surface coverage during the short derivatization time (< 60 s) was oxidized to FDS, spontaneously reducing Cu^{2+} to Cu^{+}, and promoting Cu reduction. On the other hand, the TU-Cu^{+} complex generated from the high surface coverage of TU with the long derivatization time (> 60 s) severely inhibited the Cu reduction and the bulk addition of TU alike. The possible use of TU as a reducing agent, verified from the mass increase of either the QCM electrode or dendrite formation on Cu surface after dipping the substrate into Cu electrolyte containing TU without any externally applied current, supported the spontaneous reduction of Cu^{2+} to Cu^{+} through the oxidation of TU. The Cu films having 9.2% higher hardness with only 26.0% deterioration in resistivity were deposited using TU derivatization compared to those deposited in the Cu electrolyte devoid of TU. The derivatization method is expected to assist in the investigation of the adsorption behavior of other additives, and could be potentially used in instances wherein a trade-off between the hardness and resistivity in metal deposits is required.

V. References

[1] J. J. Kim, S.-K. Kim, and J.-U. Bae, *Thin Solid Films*, **415**, 101 (2002).

[2] J. J. Kim, S.-K. Kim, and Y. S. Kim, *J. Electroanal. Chem.*, **542**, 61 (2003).

[3] S. K. Cho, S.-K. Kim, and J. J. Kim, *J. Electrochem. Soc.*, **152**, C330 (2005).

[4] R. Walker and R. C. Benn, *Electrochim. Acta*, **16**, 1081 (1971).

[5] M. R. Vogt, W. Polewska, O. M. Magnussen, and R. J. Behm, *J. Electrochem. Soc.*, **144**, L113 (1997).

[6] G. W. Poling, *Corros. Sci.*, **10**, 359 (1970).

[7] R. F. Roberts, *J. Electron Spectroscop. Relat. Phenom.*, **4**, 273 (1974).

[8] N. D. Nikolic, G. Novakovic, Z. Rakocevic, D. R. Durovic, and K. I. Popv, *Surf. Coat. Technol.*, **298**, 188 (2002).

[9] K. S. Kumar, K. Biswas, and R. Balasubramaniam, *J. Nanopart. Res.*, **13**, 6005 (2011).

[10] B. H. Loo, *Chem. Phys. Lett.*, **89**, 346 (1982).

[11] M. Fleischmann, I. R. Hill, and G. Sundholm, *J. Eletroanal. Chem.*, **157**, 359 (1983).

[12] P. W. Preisler and L. Berger, *J. Am. Chem. Soc.*, **69**, 322 (1947).

[13] Ch. Yarnitzky and R. Schreiber-Stanger, *J. Electroanal. Chem.*, **214**, 65 (1986).

[14] Y. C. Wu, P. Zhang, H. W. Pickering, and D. L. Allara, *J. Electrochem. Soc.*, **140**, 2791 (1993).

[15] H. G. Tompkins, D. L. Allara, and G. A. Pasteur, *Surf. Interface Anal.*, **5**, 101 (1983).

[16] R. Youda, H. Nishihara, and K. Aramaki, *Corros. Sci.*, **28**, 87 (1988).

[17] C. V. Thompson, *Annu. Rev. Mater. Sci.*, **30**, 159 (2000).

[18] T. P. Moffat, J. E. Bonevich, W. H. Huber, A. Stanishevsky, D. R. Kelly, G. R. Stafford, and D. Josell, *J. Electrochem. Soc.*, **147**, 4524 (2000).

[19] D. Papapanayiotou, R. N. Nuzzo, and R. C. Alkire, *J. Electrochem. Soc.*, **145**, 3366 (1998).

[20] G. Fabricius, K. Kontturi, and G. Sundholm, *J. Appl. Electrochem.*, **26**, 1179 (1996).

[21] A. Szymaszek, J. Biernat, and L. Pajdowski, *Electrochim. Acta*, **22**, 359 (1977).

[22] P. Cofré and A. Bustos, *J. Appl. Electrochem.*, **24**, 564 (1994).

[23] D. K. Y. Wong, B. A. W. Coller, and D. R. Macfarlane, *Electrochim. Acta*, **38**, 2121 (1993).

[24] D. F. Suarez and F. A. Olson, *J. Appl. Electrochem.*, **22**, 1002 (1992).

[25] A. F. Mayadas and M. Shatzkes, *Phys. Rev. B*, **1**, 1382 (1970).